University of North Dakota
UND Scholarly Commons

Theses and Dissertations | Theses, Dissertations, and Senior Projects

January 2012

Corrosion And Wear Resistance Of Titanium- And Aluminum-Based Metal Matrix Composites Fabricated By Direct Metal Laser Deposition

Ben L. Waldera

How does access to this work benefit you? Let us know!

Follow this and additional works at: https://commons.und.edu/theses

Recommended Citation

Waldera, Ben L., "Corrosion And Wear Resistance Of Titanium- And Aluminum- Based Metal Matrix Composites Fabricated By Direct Metal Laser Deposition" (2012). *Theses and Dissertations*. 1223.
https://commons.und.edu/theses/1223

This Thesis is brought to you for free and open access by the Theses, Dissertations, and Senior Projects at UND Scholarly Commons. It has been accepted for inclusion in Theses and Dissertations by an authorized administrator of UND Scholarly Commons. For more information, please contact und.commons@library.und.edu.

CORROSION AND WEAR RESISTANCE OF TITANIUM- AND ALUMINUM-BASED METAL MATRIX COMPOSITES FABRICATED BY DIRECT METAL LASER DEPOSITION

by

Benjamin L. Waldera
Bachelor of Science, University of Minnesota Duluth, 2010

A Thesis

Submitted to the Graduate Faculty

of the

University of North Dakota

In partial fulfillment of the requirements

for the degree of

Master of Science

Grand Forks, North Dakota

May

2012

Copyright 2012 Benjamin L. Waldera

This thesis, submitted by Benjamin L. Waldera, in partial fulfillment of the requirements for the Degree of Master of Science from the University of North Dakota, has been read by the Faculty Advisory Committee under whom the work has been done and is hereby approved.

_____
Dr. Matthew Cavalli

_____
Dr. Samar J. Kalita

_____
Dr. Marcellin Zahui

This thesis meets the standards for appearance, conforms to the style and format requirements of the Graduate School of the University of North Dakota, and is hereby approved.

_____
Dr. Wayne Swisher
Dean of the Graduate School

_____
Date

Title	Corrosion and Wear Resistance of Titanium- and Aluminum- Based Metal Matrix Composites Fabricated By Direct Metal Laser Deposition
Department	Mechanical Engineering
Degree	Master of Science

In presenting this thesis in partial fulfillment of the requirements for a graduate degree from the University of North Dakota, I agree that the library of this University shall make it freely available for inspection. I further agree that permission for extensive copying for scholarly purposes may be granted by the professor who supervised my thesis work or, in his absence, by the chairperson of the department or the dean of the Graduate School. It is understood that any copying or publication or other use of this thesis or part thereof for financial gain shall not be allowed without my written permission. It is also understood that due recognition shall be given to me and to the University of North Dakota in any scholarly use which may be made of any material in my thesis.

Benjamin L. Waldera
4/24/2012

TABLE OF CONTENTS

LIST OF FIGURES

LIST OF TABLES

Table Page

ACKNOWLEDGMENTS

I would like to express my sincere gratitude to Dr. Samar Kalita, Dr. Matthew Cavalli, and Dr. Marcellin Zahui for their motivation, enthusiasm, and guidance throughout my time at the University of North Dakota. I am grateful for the support of the Advanced Engineered Materials Center (AEMC) for their collaboration with Benét Laboratories under a joint program entitled 'Lightweight Reliable Materials for Military Systems' (Agreement No: W15QKN-11-2-0002). Special thanks to Benet Laboratories Cooperative Agreement Manager (CAM) Mr. Kevin Miner, Alternate Cooperative Agreement Manager (ACAM) Mr. Fang Yee and AEMC Director Dr. Michael Mann in managing the research program.

I thank all my fellow colleagues at the AEMC. Special thanks to Joshua Johnson, Douglas Larson, Juergen Fischer, Sam Cowart, Kirt Leadbetter, CJ Sitter, and Connie Larson for their continued support and collaboration. I would like to thank my parents, Denny and Connie Waldera, and my many close friends for their much appreciated love and guidance. Special thanks to my bride-to-be for her patience, understanding, and support for my academic pursuits.

To my beautiful bride-to-be

ABSTRACT

Titanium- and Aluminum-based metal matrix composites (MMC) have shown favorable properties for aerospace applications such as airframes, reinforcement materials and joining elements. In this research, such coatings were developed by direct metal laser deposition with a powder-fed fiber coupled diode laser. The MMC formulations consisted of pure titanium and aluminum matrices with reinforcing powder blends of chromium carbide and tungsten carbide nickel alloy. Two powder formulations were investigated for each matrix material (*Ti1, Ti2, Al1* and *Al2*). Titanium based composites were deposited onto a Ti6Al4V plate while aluminum composites were deposited onto AA 7075 and AA 5083 for *Al1* and *Al2*, respectively. Microstructures of the MMCs were studied by optical and scanning electron microscopy. The hardness and reduced Young's modulus (E_r) were assessed through depth-sensing instrumented nanoindentation. microhardness (Vickers) was also analyzed for each composite. The corrosion resistance of the MMCs were compared by monitoring open circuit potential (OCP), polarization resistance (R_p) and potentiodynamic polarization in 0.5 M NaCl to simulate exposure to seawater. The Ti-MMCs demonstrated improvements in hardness between 205% and 350% over Ti6Al4V. Al-MMCs showed improvements between 47% and 79% over AA 7075 and AA 5083. The MMCs showed an increase in anodic current density indicating the formation of a less protective surface oxide than the base metals.

CHAPTER I

INTRODUCTION

Research Objective

The objective of this research was to investigate the corrosion and wear resistance of metal matrix composites (MMC) fabricated by direct metal laser deposition (DMLD). Specifically, composites with aluminum and titanium matrices were developed because of the wide scope of applications in which these materials are used. The applicability of these alloys can be largely attributed to the favorable mechanical and electrochemical properties offered by these alloys such as high specific strength and corrosion resistance. However, there is significant industrial need to improve the long term survivability of materials exposed to highly corrosive and abrasive environments.

Research has shown that DMLD is a viable method for laser surface engineering and rapid manufacturing. This method is an attractive alternative to conventional MMC processing methodologies due to the favorable characteristics and economic value associated with DMLD [1-4]. DMLD allows MMCs to be fabricated with virtually endless combinations of metal and non-metal powders, many of which are selected to improve physical, mechanical, or electrochemical properties.

There are many processing techniques for the fabrication of MMCs. These techniques can be classified as liquid, powder, solid or gas phase processes [5]. However, few studies specifically analyze the effect of adding various powders by DMLD on corrosion and wear resistance. Thus, the analysis performed in this research aims to

investigate the corrosion and wear resistance of titanium- and aluminum- based MMCs fabricated by DMLD.

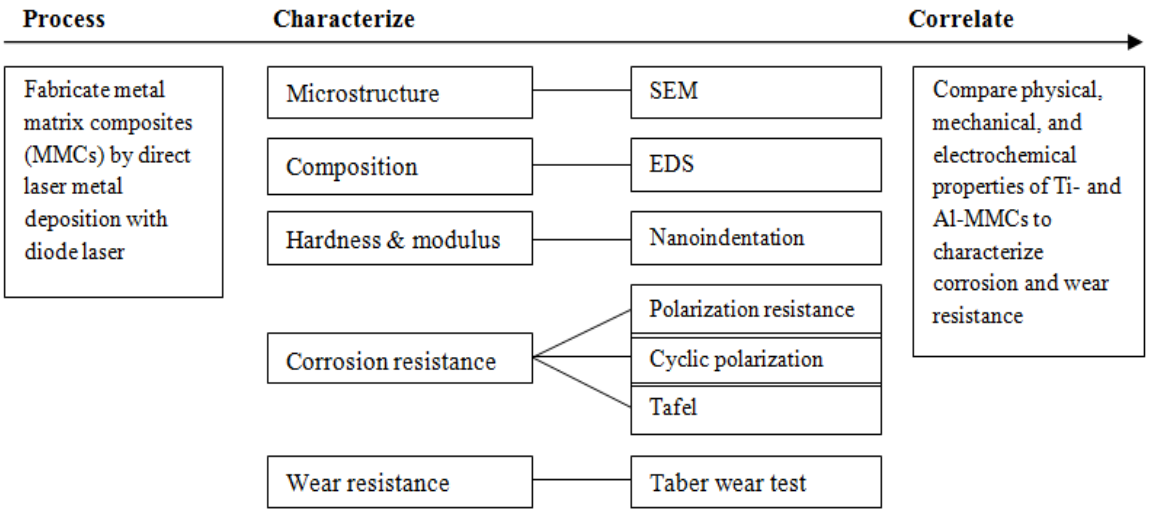

Figure 1. Experimental Methodology

Figure 1 presents a schematic for the processing and characterization methodology used in this research. DMLD was carried out using a powder-fed fiber-coupled diode laser to deposit molten material onto the substrate. After fabrication, samples were visually inspected for defects before being sectioned and mounted. Optical and scanning electron microscopy was carried out to analyze microstructure and chemical composition of the MMCs. Mechanical properties were investigated by nanohardness, microhardness, and Taber wear testing. Corrosion resistance was analyzed by monitoring Open Circuit Potential (OCP), polarization resistance (R_p), and by conducting cyclic potentiodynamic polarization in an aqueous solution of 0.5 M NaCl.

Metal Matrix Composites

A metal matrix composite (MMC) is a type of composite material that is composed of two or more distinct parts, at least one of which is a metal. The secondary constituents may consist of other metals, ceramics or even organic compounds.

Conventionally, the material that exhibits support for the structure in which reinforcing materials may be added is called the matrix. Titanium, aluminum and magnesium are the most frequently used matrix materials for MMCs [6]. Reinforcement materials may be continuous fibers oriented in a specific direction or discontinuous as is the case with powder-based processing. The reinforcement materials may serve specific purposes such as improving thermal conductivity, wear resistance or corrosion resistance. The development of new advanced composite materials requires a method of strategic processing, empirical testing, as well as qualitative and quantitative analysis.

To develop MMCs for specific industrial applications, engineers must evaluate design requirements and choose a set of material selection criteria. In composite material systems, material design criteria are focused on developing a certain set of physical and/ or chemical characteristics to improve performance, increase lifetime, or reduce manufacturing costs. Improving these characteristics is crucial to the successful implementation of MMCs. Conventionally, the advantages of MMCs are only realized in applications where there is an acceptable cost-to-performance relationship or when a certain property profile is only achievable through MMCs [7].

Strategic material selection requires a design engineer to account for a number of factors [8-11]:

1. Static characteristics
2. Fatigue characteristics
3. Fracture characteristics
4. Damping characteristics
5. Thermal properties

6. Manufacturing methods
7. Environmental characteristics

In literature, static characteristics such as longitudinal, transverse, and shear strengths have been well-established for these MMCs [9]. Furthermore, fatigue and fracture characteristics have also been studied extensively as a result of their importance in the aerospace industry. Many MMCs have been designed to offer significant hardness, strength and fracture toughness advantages over bulk alloys [12]. The ability to tailor a material's properties for use in a specific application is one of the major technical advantages of MMCs [6].

Today, MMCs have been used in the automotive industry to strengthen pistons, crankcases, and disk brakes [7]. SiC/Al and SiC/Ti MMCs have been utilized in the field of high temperature supersonic air travel. The scope of possible applications is seemingly endless and continues to grow. Industries where significant improvement is needed in corrosion and wear resistance are of particular interest to the present research. For some applications in the aerospace, automotive, shipbuilding, and biomedical industries, corrosion and wear resistance are crucial to the long term survivability of a part.

Corrosion Resistance of Metal Matrix Composites

There are many forms of corrosion; however, this study focuses on uniform surface attack, localized corrosion, and pitting corrosion because of their prevalence in commercial applications. Uniform surface attack occurs in titanium and aluminum alloys when the protective oxide present on the surface of a material is soluble in its surrounding environment. This may be especially true in sodium chloride, phosphoric

acid, or sodium hydroxide [13]. The rate of attack in this form of corrosion is dependent on the specific ions present, their concentration, and their temperature.

Localized corrosion occurs in environments where the surface oxide is insoluble, causing corrosion to occur at weak points in the oxide film. Localized corrosion is caused by a difference in the corrosion potential in a localized cell that may be formed on the metallic surface. This difference in potential is typically a result of cathodic microconstituents in the surface, such as insoluble intermetallic compounds [14]. However, there are other causes for localized corrosion. For instance, a stray electric current leaving the surface may cause localized corrosion or dry oxidation as is frequently seen in fretting corrosion [14].

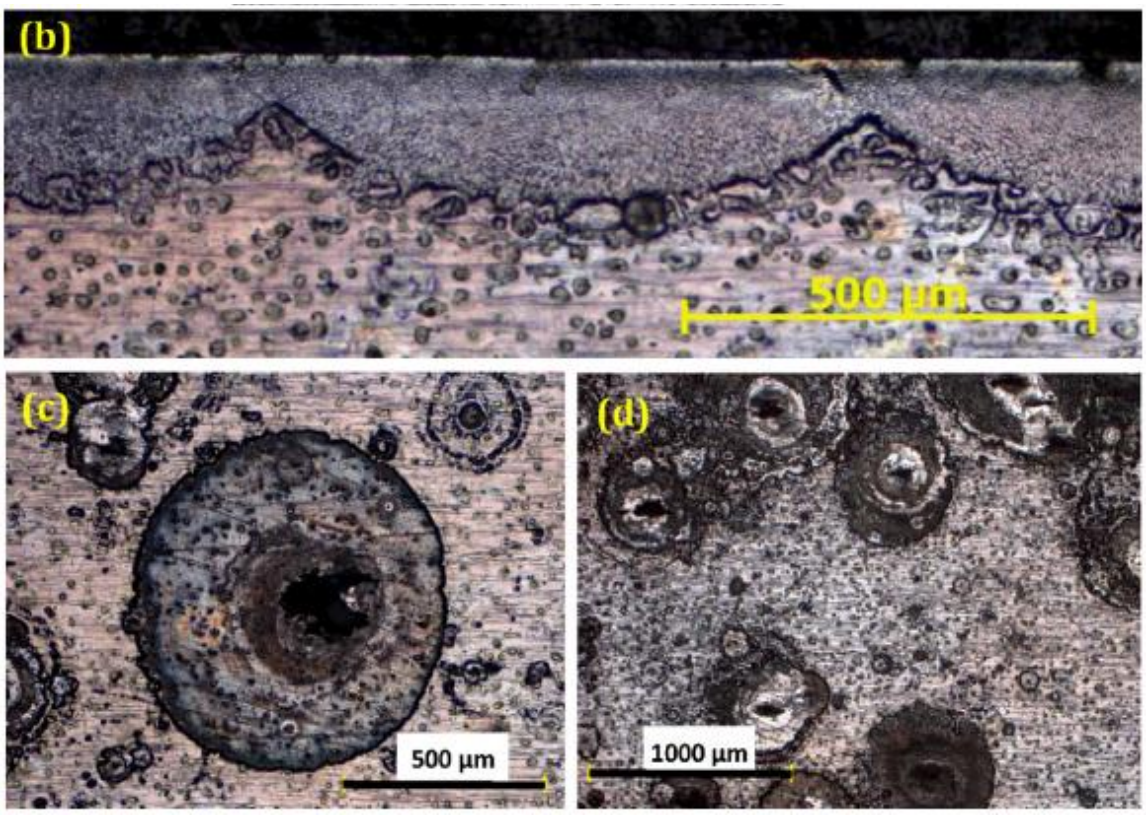

Figure 2. Optical micrograph after immersion test of AA 2024: (a) laser melt tracks along with a large and many small pits in the un-melted region, (b) consecutive melt tracks demonstrating no pitting within the melted region, (c) a large pit (un-melted region) and (d) multiple pit formation (un-melted region) Used with permission [15].

Pitting corrosion of titanium and aluminum occurs at localized sites when the surface is exposed to an electrolyte resulting in the development of cavities. The propagation of cavities occurs when imperfections in the surface oxide film cause Cl^- to displace oxygen from the surface [14, 16, 17]. The roughly circular geometry of a pit distinguishes it from intergranular corrosion where the attack is confined to grain boundaries. Pits form as a result of local electrochemical cells at the metallic surface and thus pitting corrosion is similar to localized corrosion [16, 18]. Figure 2 presents typical pit morphologies that occur in AA 2024 aluminum, when immersed in a corrosive medium [15]. These images show the formation of pits in areas of the specimen that have not been laser treated. These images indicate that pitting corrosion can be mitigated by certain laser processing techniques, like laser melting.

Galvanic corrosion occurs when there is electrical contact between a metal and a nobler metal or nonmetallic in a conductive environment. This type of corrosion most frequently occurs in application when aluminum is joined with another material such as steel or copper. In this case the aluminum corrodes more rapidly than it would if it was not in contact with the more noble material. The rate of this attack depends on 5 major factors: the difference in corrosion potentials of the two metals, the electrical resistance between the two metals, the conductivity of the electrolyte, the cathode-anode area ratio and the polarization characteristics of the two metals [13].

Intergranular corrosion often occurs in aluminum alloys when magnesium precipitates to the grain boundaries and is thus a problem in commercial applications. Intergranular corrosion occurs at the grain boundary zone, without any significant attack on the grain body of the material. Intergranular corrosion is the result of an

electrochemical cell in the grain boundaries that is formed between second-phase microconstituents and the depleted metallic solid solution [13]. In this case the constituents exhibit a different corrosion potential than the adjacent material.

In practice, MMCs tend to corrode differently than bulk alloys. The nonhomogenous nature of MMC anatomy tends to cause more areas of localized corrosion than observed in the bulk matrix. Effects of processing methodology and the presence of reinforcing elements can cause accelerated corrosion of the structure as compared to an unreinforced matrix alloy. This propensity for accelerated corrosion originates from the chemical and electrochemical interactions between the constituent materials and microstructure. MMCs exhibit unique structures as a result of particle or fiber reinforcements that cause segregation, dislocation generation, and micro-crevice formation at the reinforcement/matrix interface [19, 20].

These corrosion processes are often initiated at the interface between reinforcing elements and matrix. In addition, intermetallic particles may form at this interface. The initiation of corrosion around the fiber/matrix interface in alumina fiber reinforced Al–2% Cu–T6 alloy causes dissolution of the adjacent matrix. Figure 3 presents SEM images of this alumina fiber reinforced Al–2% Cu–T6 alloy [21]. It can be observed that corrosion is initiated around a small intermetallic particle that is located at the fiber/matrix interface. In this case, the fiber/matrix interface, containing intermetallic particles rich in Fe and Cu, served as cathodic sites for the initiation of localized corrosion.

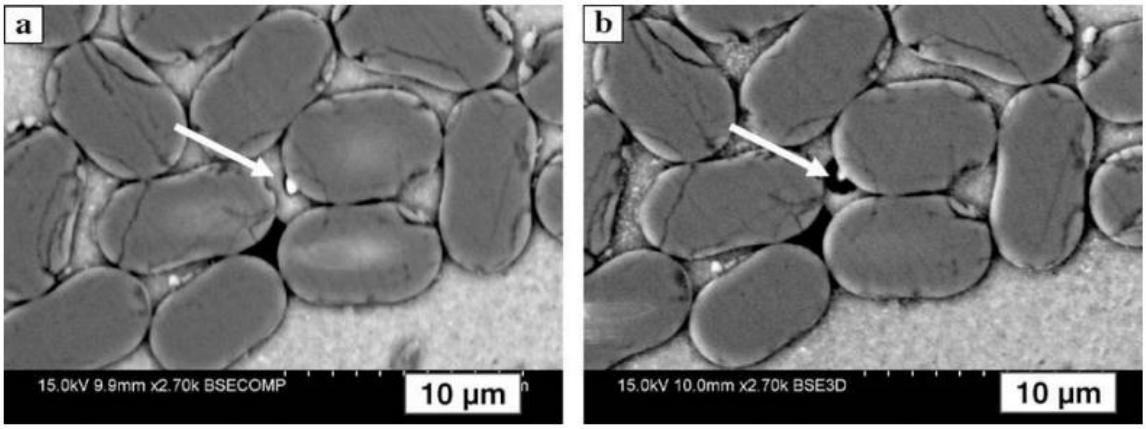

Figure 3. SEM images of Al–2%Cu/Al_2O_3/60f–T6 MMC in the as-polished virgin condition (a), and the same site, after exposure in air-exposed 3.15 wt.% NaCl at RT (b). Corrosion initiation occurred around a small intermetallic particle. Notice the matrix dissolution around the particle [21].

While localized corrosion around the fiber or reinforcement/matrix interface is a primary area for localized corrosion, other forms may exist between these materials. Chemical degradation of interphases and reinforcements may occur via chemical reactions that cannot be represented by electrochemical analysis. They must undergo chemical degradation, as is the case in the hydrolysis of the Al_4C_3 interface in aluminum carbide degradation [22].

Microstructure may also influence corrosion when reinforcements or intermetallic phases are present as a result of solute rejection during solidification [23]. These intermetallic phases occasionally have potentials and corrosion resistances not equal to that of the matrix. In this case, galvanic corrosion may again be induced. For example, this occurs in certain aluminum alloys when the Al_8Mg_5 or Mg_2Si intermetallic phases provide a corrosion path along the reinforcement/matrix interface in Al_2O_3 MMCs [22]. Furthermore, the dislocation density of the microstructure may play a role in accelerated corrosion. It has been observed that the higher the dislocation density the greater the risk of increased corrosion rates in some metals [24]. Thus, it can be generalized that the

factors affecting the degradation of MMCs by corrosion are galvanic corrosion between MMC constituents, chemical degradation due to interphases as a result of localized corrosion, and uniform corrosion [19, 20].

Corrosion Resistance of Titanium Metal Matrix Composites

Titanium is often used for its corrosion resistant properties. Titanium is known to be more corrosion resistant than steel; however, it is not considered to be corrosion proof as are gold and platinum [17]. Instead, titanium relies on the formation of a passive surface oxide to protect the bulk material from the environment. The formation of the passive surface oxide is attributed to the highly reactive nature of titanium with oxygen. This reaction forms a highly adherent and chemically inert passive oxide film on the surface [25].

In most aqueous environments, titanium forms protective surface oxides $Ti0_2$, Ti_20_3 or TiO. At high temperatures the most commonly formed oxide is $Ti0_2$. The more amorphous Ti_2O_3 is formed at lower temperatures and may occur as a mixture of Ti_2O_3 and TiO_2 [17].

Certain alloying elements can play a major role in the general corrosion behavior of many titanium alloys. For example, vanadium and molybdenum are known to improve corrosion resistance while the opposite is true for aluminum. Alloying elements that cause a positive potential shift cause a stable oxide film to form that may overcome corrosion resistance limitations of titanium alloys in aggressive reducing environments [17]. Thus, a reduction in anodic activity corresponds to an improvement in corrosion resistance. However, corrosion analysis of titanium is not always so simple.

Ti-MMCs, used in the automotive, aerospace, and biomedical industries, may corrode differently than the bulk matrix. A Ti-MMC structure may have reinforcing elements that tend to resist repassivation, leaving weak areas in the protective surface oxide [22]. Localized corrosion will often initiate at these areas where the corrosion-resistant surface oxide is weakest.

Corrosion studies of SiC/Ti-MMCs indicate that the titanium matrix passivated while the carbon-rich SiC monofilaments oxidized when exposed to a 3.5% NaCl solution [26]. Similarly, studies have been done detailing TiC/Ti-MMCs. In one study, a TiC/Ti-MMC showed a 20 times higher dissolution current when anodically polarized in a 2 wt% HCl environment. In this case, microscopy indicated that the titanium matrix was virtually uncorroded but the TiC reinforcing particles, again, showed signs of degradation [22].

Corrosion Resistance of Aluminum Metal Matrix Composites

Like titanium, aluminum alloys are known to have good corrosion resistance in many natural environments such as fresh water or seawater. Based on thermodynamics, the corrosion behavior of aluminum should be quite poor and highly reactive. However, the resistance to corrosion of aluminum in many environments is due to the presence of a highly adherent surface oxide. As fresh aluminum surfaces are exposed to air or water, the film grows rapidly on the surface up to approximately 5 nm thick [13, 18, 27, 28].

Corrosion resistance of aluminum is dependent on the preservation of this oxide on the surface. In some chemicals, the oxide may dissolve resulting in rapid uniform dissolution. Furthermore, factors that affect corrosion may include composition,

fabrication methodology, and environment. These factors determine the microstructure which may ultimately determine the rate of corrosion or method of attack.

In marine applications, the shiny appearance often becomes a non-aluminum looking gray color. Common alloys for marine applications include commercially pure aluminum, Al-Mn, Al-Mg, and Al-Mg-Si alloys because of their good corrosion resistance. Al-Cu and Al-Zi-Mg are known to have poorer corrosion resistance and often require protection with either painting or cladding [13].

The corrosion resistance of Al-MMCs reinforced with SiC, Al_2O_3, and several others have been recently investigated. In composites with SiC reinforcing whiskers and particulates, it was observed that the corrosion rate was higher than that of the monolithic matrix alloy and increased as the volume fraction of SiC constituents increased [22]. The passive current density and pitting potential of MMCs with SiC particles or whiskers does not exhibit major changes when immersed in aqueous solution. This indicates that the SiC particulates do not significantly degrade the pitting-resistant passive surface oxide that exists on the surface of aluminum in chloride solutions [29]. However, while pit nucleation is inhibited, the pits remain shallow in shape; they appear to increase in number as they form in the intermetallic particles which are smaller and more numerous in SiC-MMCs [30]. Similarly, Al_2O_3 reinforcement particles have shown to have minimal effects on pitting potential in chloride solutions [19].

Fabrication of Metal Matrix Composites

The fabrication methodologies for MMCs may be categorized by either liquid-, vapor- or solid-state processes. Liquid-state processes include but are not limited to electroplating, infiltration, or spray deposition while vapor deposition processes may

include physical or chemical vapor deposition. Solid-state processing most frequently involves powder consolidation (powder metallurgy), diffusion bonding or direct metal laser fabrication. The following sections describe the basics of conventional processing.

Liquid-State Processing

Liquid-state processing of MMCs have historically offered significant advantages over conventional solid-state processing [6]. Liquid metal was often less expensive and easier to handle than powders. Also, castings can be easily produced in near-net shapes using methods already in existence for non-reinforced materials [6]. Thus, much attention has been given to developing a better understanding of liquid-state processes over the last 20 years.

There are four major methods for combining the matrix and reinforcement particles by liquid-state processing: (a) infiltration, (b) dispersion, (c) spraying, and (d) in-situ fabrication. All four of which have been modified and combined over the years to create new processes aimed at minimizing the cost of development [31-33].

Infiltration-based processes can be thought of as methods in which a porous body of reinforcing elements is “infiltrated” with molten metal flow which fills the pores and solidifies to create the composite. In these processes the major processing parameters include material composition, volume fraction, morphology, force applied, and temperature of the infiltrating material. For example, it has been found that increased pressure applied during solidification may produce a finer grain structure than is achievable through solidification at atmospheric pressure. This refinement in grain structure is a result of greater heat transfer between the mold and the composite [34]. An advantage of infiltration processing includes the ability to fabricate parts near-net shape.

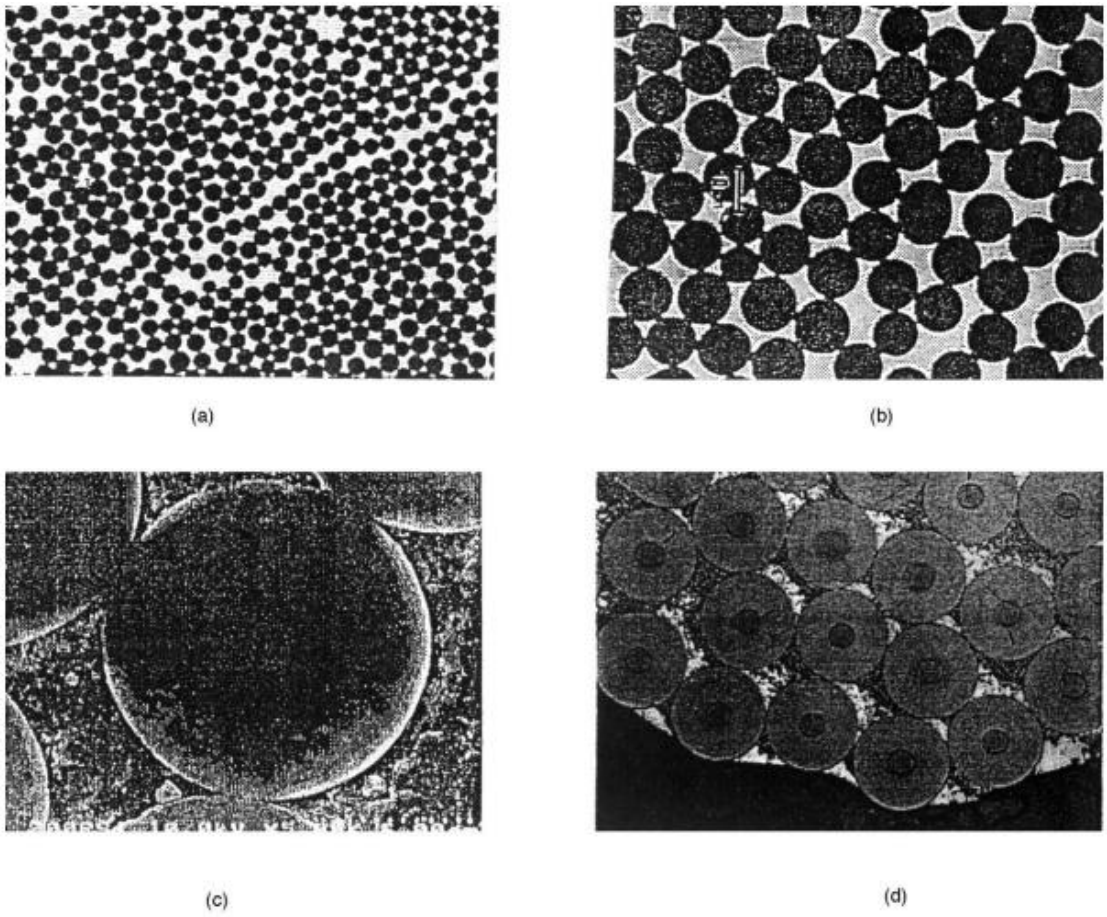

Figure 4. Cross-section pictures of continuous fiber MMCs produced by continuous pressure infiltration. (a) Pitch type carbon/Al wire 400x. (b) Nextel 610/Al wire 975x. (c) Si-Ti carbide/Al wire 8000x. (d) SiC/Al wire 110x. Used with permission [35].

Figure 4 shows pictures of several different types of MMCs fabricated by continuous pressure infiltration. Continuous pressure infiltration allows control over production parameters like production speed, fiber volume fraction, and wire diameter [35]. A major advantage of continuous pressure infiltration is that it allows multiple wires of various fiber-metal combinations to be manufactured.

Another type of liquid-state processing includes dispersion processing. Dispersion processing mixes reinforcing constituents into the liquid metal by stirring. This method is inexpensive and allows materials to be made in large quantities but requires further processing such as extrusion or casting. Various types of mixing have been developed to

minimize the amount of impurities, oxides, and gases in the MMC [6, 36]. Ultimately, the success of this process is determined by the control over undesirable features like porosity as a result of gas entrapment during mixing. Also, oxide inclusions and particle migration are of concern.

In spray processing, drops of molten metal are sprayed with the reinforcing phase through a nozzle with atomizing gas onto the surface of a substrate. This process has been used for unreinforced materials for some time due to the favorable refinement in grain structure realized by the high solidification rates during the process [37, 38]. However, residual porosity may be a concern which would require secondary processing. In addition, this methodology is typically not as economical as dispersion or infiltration processes.

In-situ composites are composites materials that are fabricated by solidification of poly-phase alloys. This methodology has been especially important for the processing of high temperature materials produced by controlled solidification. The major advantage is that the reinforcing phase is often homogeneously distributed in the material. Also, the relative dispersion size and spacing of the reinforcement phase can be controlled by the solidification or reaction time [39].

The liquid-state processing techniques, described above, are often plagued by porosity, incomplete control of the processing parameters, and the propensity for undesirable chemical reactions to occur between the molten metal and reinforcement [6]. Thus, it is important to analyze other methods of fabrication.

Solid-State Processing

Solid-state fabrication processes are generally known to obtain the best mechanical properties as a result of minimal brittle reaction product formation as compared to liquid-state processing techniques. This is especially true for discontinuous MMCs [6]. The most common methods of solid-state processing include powder consolidation, high-rate consolidation, and diffusion bonding.

In powder consolidation, metal powders are mixed with reinforcement particulates. Next, the formulation typically undergoes cold isostatic pressing to obtain a green compact which can then be outgassed and extruded or forged. Powder consolidiation can also be achieved through liquid-phase sintering because the low melting phase pulls the solid particles together as a result of the force of surface tension [40].

Another method of solid-state processing is diffusion bonding which uses foil layers and fibers to create single- or multiple-ply composites that exhibit solid-state creep deformation. This means that the matrix foils exhibit creep flow between the fibers and eventually make metal-to-metal contact. Titanium and aluminum alloys reinforced with SiC and B fibers are some of the common MMCs made by this method for use in gas turbine engines [6].

High-rate consolidation is another solid-state fabrication process by which frictional heating at the powder-particle interface causes melting and consolidation, followed by rapid solidification upon cooling [41]. This type of processing strengthens alloys by increasing the dislocation density in the material. However, these structures typically contain cracks which are a major hindrance of this methodology.

These solid-state processes often produce discontinuously reinforced MMCs with agglomerates or an uneven distribution of reinforcing particulates. This can be detrimental to the performance of the part; however, the refinement of grain structure achievable with solid-state processing is a primary reason that research has continued with similar solid-state processes.

Vapor Deposition

Vapor deposition processes, in general, describe a method of depositing a thin film by condensation of a vaporized form of a specific material onto a substrate. Common techniques include physical and chemical vapor deposition, evaporative deposition, pulsed laser deposition, and sputter deposition. This process is the most commonly used process for applying thin films on individual fiber surfaces [42].

Pulsed Laser Deposition (PLD) is a physical vapor deposition technique in which a high-powered laser strikes a target of a desired composition, like a silicon wafer, and creates a plasma plume which deposits a thin film of material on the substrate. PLD is used in the fabrication of WC-Co MMCs for the repair of cutting tool materials [43]. A schematic of a typical PLD process is provided in Figure 5 [44].

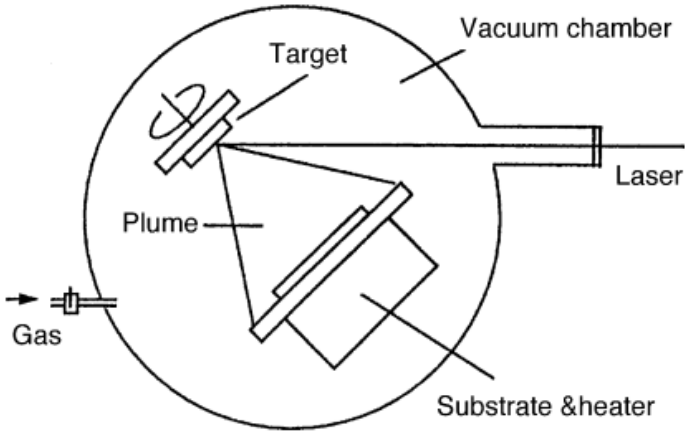

Figure 5. Schematic of the PLD process. Used with permission [44]

Direct Metal Laser Fabrication

Direct metal laser fabrication (DMLF) is a processing methodology for the fabrication of MMCs utilizing a high-powered laser and metal, ceramic, or other non-metal powder. It has been used to create novel surfaces with different physical, mechanical, and electrochemical properties than the substrate. These powder-based processes may be advantageous in the fabrication of MMCs due to the flexibility in creating composites with different chemical compositions in an economical manner. Advantages of this process include better coatings with minimal dilution, minimal distortion and better surface quality [1]. When repeated layer-by-layer, these DMLF processes allow the creation of freeform parts as is done in layer-additive manufacturing.

Layer-by-layer manufacturing processes have been under development for roughly a quarter century. Today, companies like Fiat, Toyota, and Mercedes Benz are using layer-by-layer laser technology for the production of engine valve seats. Rolls Royce utilized layer-by-layer laser technologies for turbine blade repair in modern day aircraft [1].

DMLF processes are divided into two primary groups based on the phase of the powder during the process: non-melting systems and melting systems. Sintering-based operations like direct metal laser sintering (DMLS) will often exhibit minimal melting of the powders during processing with solidification being a result of liquid phase sintering instead of complete melting of powder [45]. Melting-based operations like Selective Laser Melting (SLM) and Direct Metal Laser Deposition (DMLD) exhibit complete melting of both matrix and reinforcing powders. Thus, a solid structure is formed upon rapid quenching of the melt pool. Melting processes may be further categorized

according to the method of powder delivery. SLM uses a preplaced powder, often referred to as a powder bed, to build structures layer-by-layer. Conversely, DMLD uses powder delivered by a stream of gas aimed at the laser beam to place molten powder on the substrate. DMLD is the fabrication methodology employed in this research.

Direct Metal Laser Deposition

The process of DMLD is described by many names: Direct Metal Laser Deposition, Laser Engineered Net Shaping, Controlled Metal Buildup, and several others [1, 46, 47]. All, however, refer to the same philosophy of building up metal layer-by-layer with a high-powered laser system. DMLD utilizes a laser heat source to deposit a thin layer of molten powder onto a substrate. Material may be delivered to the heat source by wire feeding or powder injection. Powder injection, however, has been shown to be the most effective [1]. An inert shielding gas surrounds the laser/material interaction zone to prevent oxidation. Thicknesses between 0.05 and 2 mm with widths as small as 0.4 mm are conventionally observed. Figure 6 presents a schematic for a DMLD system that utilizes coaxial powder feeding with inert shielding gas as was used in the fabrication of MMCs in this research [48, 49].

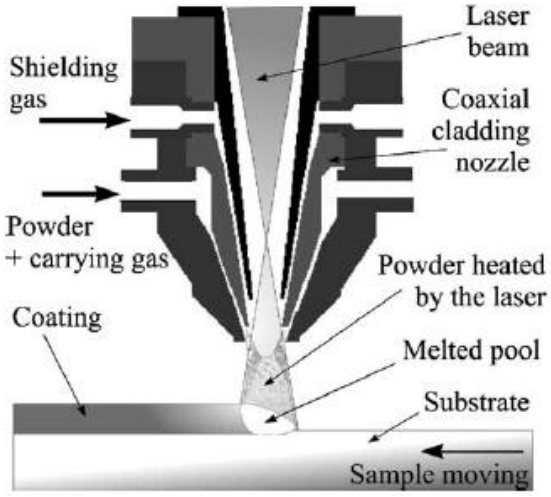

Figure 6. Schematic of DMLD with coaxial powder injection

Common materials used with this process include titanium alloys, nickel alloys, steels cobalt alloys and aluminum alloys. Titanium hip implants have been created from Ti6Al4V powder with equivalent tensile and fatigue properties to the wrought materials [45]. The Interdisciplinary Research Centre (IRC) at the University of Birmingham in partnership with Rolls-Royce has fabricated turbine blades from a burn-resistant beta titanium alloy [50]. Furthermore, The National Research Council of Canada has developed functional net shape Ti6Al4V and Inconel alloy components for a space robot manipulator [45].

DMLD is a complicated process with many parameters that can affect the final performance and properties of the part. Parameters like laser power, laser spot diameter, substrate scanning speed, laser energy density, hatch spacing and even scanning strategy can affect the finished product. Material properties like thermal conductivity of the metal powders or substrate, spectral absorptivity, and even surface tension may have an influence. Previous research has been concentrated on the influence processing parameters on the roughness, density, microstructure and mechanical properties of components fabricated by DMLD. Special attention has been given to developing structures and coatings for use in aerospace, automotive, shipbuilding, and biomedical industries [51-54]. The following is a description of many of the most important processing parameters that can be manipulated to achieve the desired structure.

The average applied energy per interaction area during the scan is referred to as the energy density. The energy supplied by the laser must be high enough to melt the powder as well as a small amount of the substrate but not too high as to cause major dilution of the substrate [1]. The size of the melt pool created by the laser depends on

energy density which is a function of power and scan speed [1, 4, 54]. In theory, the size of the melt pool is predicted to be of equal volume for equal ratios of $P/\sqrt{\upsilon}$ where P represents power in Watts (W) and scanning velocity (υ) in mm/min. Increasing this ratio results in the formation of a larger melt pool [54]. Some have reported that increasing the power of the laser while keeping scanning velocity constant will result in larger grain sizes due to a slower cooling rate for a larger melt pool [54]. The large temperature gradient created in the melt pool can induce strong convection forces which are developed due to the Marangoni effect [1, 55]. As a result, the molten pool mixes and solidifies to form a dense, well-bonded clad layer.

It has been observed that the intense thermal gradients achieved during the DMLD process, resulting from extremely fast cooling rates, cause the buildup of residual stresses in the material [1, 54]. The structure must be built on a solid substrate to overcome the tendency for the material to curl due to the build-up of thermal stresses during the heating and cooling process. Furthermore, the thermal stresses have been known to induce segregation phenomena and the presence of non-equilibrium phases [54, 56].

Adjusting the scanning velocity allows the operator to maintain the same power and hatch spacing while increasing or decreasing the energy density by changing the ratio of $P/\sqrt{\upsilon}$. In industry, where high production rates to increase throughput are highly desirable, it is advantageous to increase the scanning speed of the process. Several studies have shown that irregularities in the scan track may appear in parts where the scanning velocity is too low. This can be attributed to instability in the melt pool as a result of hydrodynamic effects at slower velocities [54]. Furthermore, lower velocities may result

in a coarser microstructure as a result of a slower cooling rate due to a larger volume of material being melted [54].

Hatch spacing refers to the distance between successive scans of the laser beam as shown in Figure 7 [57]. Variation in hatch spacing allows further customization of energy density by influencing the amount of overlap between two neighboring melt tracks [54]. Lore *et al.* observed a decrease in hardness of Ti6Al4V based MMCs when the hatch spacing is increased [54].

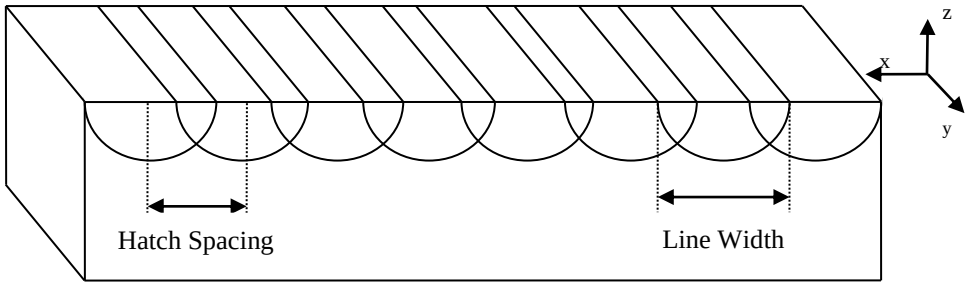

Figure 7. Hatch spacing and line width

The scanning strategy used in DMLD can have an effect on the growth direction of the elongated grains formed during rapid solidification of the melt pool. Grains will grow towards the melt pool. Typical scanning strategies may be either unidirectional or in a herringbone pattern. Lore *et al*. has reported a more isotropic microstructure and improved density in Ti6Al4V by rotating the scanning strategy from layer to layer making a grid pattern [54].

Titanium Metal Matrix Composites Via DMLD

Many studies can be found on the effect of adding carbide particles to a matrix of titanium for the purpose of increasing wear resistance. Despite the favorable properties of titanium and its alloys, they are often considered to have poor wear resistance [58]. When titanium alloys are used in severe friction and wear environments, the long-term use may

be restricted due to their poor tribological properties [55, 58-61]. Thus, the development of more wear-resistant surfaces on titanium alloys has seen much research. Titanium matrix composites have been applied in applications where WC-Co hard metals were once used [12, 62, 63].

Few studies examine corrosion and wear resistance of composites that have been fabricated by laser processes. DMLD is an attractive technique for creating carbide-reinforced metal matrix composites with a titanium matrix due to its potential for cost reduction. Since particles are fed by coaxial injection, it is easy to tailor a ceramic composite layer, creating MMCs with compositionally gradient interfaces [59, 64-67]. Many different composite formulations have been studied. Some of the most common include Ti-N, Ti-C-N, Ti-Al, Ti-SiC, Ti-TiC(WC), TiB and Ti-Co [58, 65]. The results of these studies have shown that laser surface modification can create MMC layers with ceramic particles on the surface of titanium alloys with the goal of combining the strength and ductility of bulk titanium with the excellent wear properties of ceramics.

Figure 8 presents a macrostructural view of a Ti-5wt% CNT coating as fabricated by DMLD [68]. It can be observed that solidification of the clad layer showed a homogeneous structure with excellent bonding to the substrate. The clad interface has a smooth profile with no cracks or porosity.

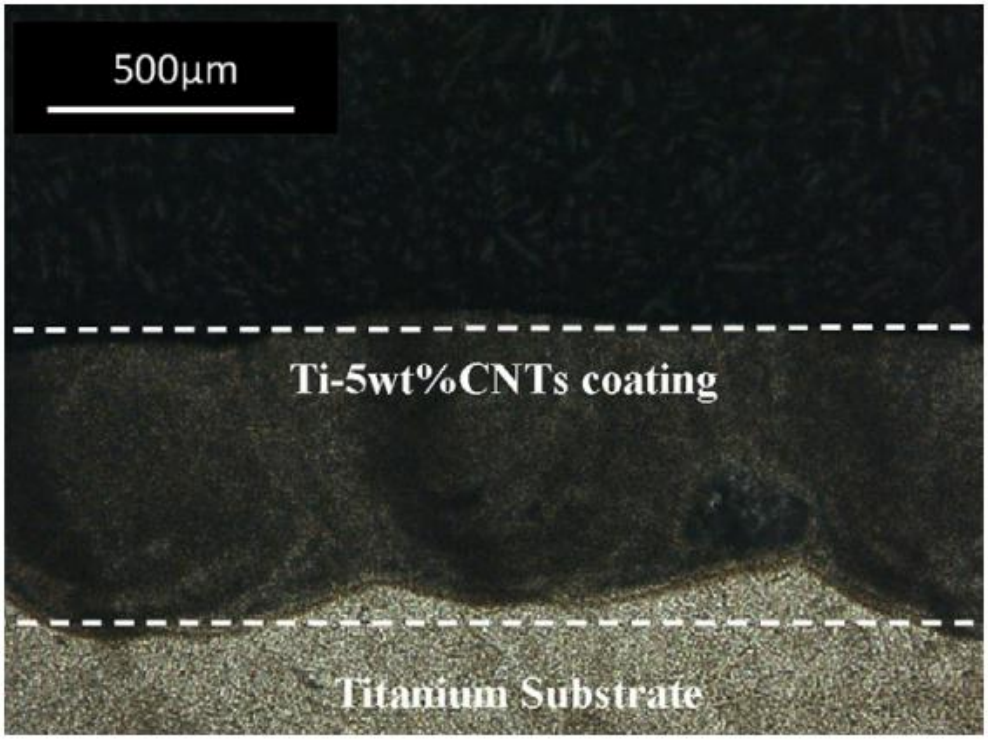

Figure 8. Cross-section of the Ti-5wt% CNT clad layer coating fabricated by DMLD with a laser power of 700 W and 10 mm/s. Used with permission [69].

Sun *et al.* examined cladding Ti-TiC and TiC+ NiCrBSi [3]. It was found that increasing specific laser energy decreased the depth of the TiC clad zone while the dilution zone increased. In this research microhardness values as high as 2100 HV– 2300 HV were observed in regions with clustered TiC particles. Areas in the MMC coating without clustered particles yielded a microhardness of 800 HV – 900 HV. In addition, an increase in specific laser energy produced a greater amount of TiC particles in solution as well as a higher microhardness in the TiC + NiCrBSi MMC, however the variation in microhardness was exaggerated with an increasing TiC volume fraction [3].

Candel *et al.* used TiC particles to reinforce titanium MMCs for the improvement of sliding wear resistance of Ti-6Al-4V [59]. Rockwell C hardness showed a significant increase due to the presence of the TiC particles and demonstrated that increasing the carbide content caused an improvement in sliding wear resistance. However, when the

laser specific energy was increased no improvement in hardness was seen. The authors suggest that this is a result of increasing dilution of the Ti-matrix [59].

Titanium boride (TiB) reinforced α-Ti matrix composites have been examined and are of interest due to Ti-TiB's similar coefficient of thermal expansion to Ti [70]. These composites have shown improved mechanical properties via several processing methodologies including combustion synthesis, rapid solidification processing and powder metallurgy [65]. Laser cladding of TiB powder to form a TiB dispersed α-Ti matrix composite yielded fine spherical whisker shaped TiB precipitates in α-Ti matrix. Also, the average microhardness of the MMC coating was found to show signicificant improvements in microhardness. Vickers hardness values of 290 HV to 500 HV were observed in a study by DuttaMajumdar and Li (2010) [70]. This was a significant improvement over the 250 HV commercially available α-Ti. Furthermore, the hardness on the TiB particles reached as high as 1275 VH [70].

DMLD of cobalt onto Ti6Al4V has also been investigated for coatings on hip and femoral prostheses [65]. DuttaMajumdar *et al.* have investigated using cladding to form a compositionally graded surface. They have reported that the microhardness in the Co-clad zone is very low (approximately 100 VH). However, nearer the surface, a higher hardness is achieved because of a greater amount of Co_2Ti, TiCo and Ti_2Co in the clad zone [65]. The hardness of the MMCs was as high as 900 HV. Furthermore, the presence of Co_2Ti, TiCo and Ti_2 Co in the MMC indicated an improvement in wear resistance over Ti6Al4V alloy as evaluated by a ball-on-disc wear testing unit. In this study, cyclic potentiodynamic polarization indicated that the pure Co-clad region demonstrated improved uniform corrosion resistance but deteriorated pitting resistance [65].

Pimenov and Starr investigated the electrochemical and corrosion behavior of Ti-xAl-yFe alloys fabricated by direct metal deposition was investigated [71]. The aim of the work was to assess the corrosion resistance of Ti-xAl-yFe alloys in Hank's simulated biofluid solution with Ti-MMCs fabricated by DMLD. Ti-xAl-yFe alloys with Al content ranging from 0 to 27% and Fe content between 0 and 25 wt% were fabricated with a DMD 3000 machine [71]. This is a 3000W CO_2 laser with powder injection. The powders used were blends of pure elemental powders of titanium, aluminum and iron. A Ti6Al4V substrate was used.

Electrochemical characterization was performed for each composition. Each layer was cut and mounted in epoxy resin and polished to 600 grit with carbide abrasive paper. Samples were washed in 10% HCl then rinsed with ethanol prior to testing [71]. A conventional three electrode cell with a Pt wire gauze as counter electrode with a saturated silver/silver chloride reference electrode was used. The geometrical area of working electrode was 0.8 cm^2 [71].

Prior to polarization scans, the samples were exposed to test solutions for 12 h to attain equilibrium conditions. The anodic potentiodynamic and cyclic voltammetry measurements were made with an EG&G Princeton potentiostat at a scan rate of 5mV/s between -0.6 and 2.5 V [71].

Results indicate that, for Ti-xAl a fine needle like α-phase referred to as fine lamellar or acicular microstructure exists [71]. After laser melting, high cooling rates cause α-phase to be changed to acicular martensitic product. Alpha prime martensite formed in the melted zone and the fine needle like acicular formation exhibits a hexagonal close packed crystal structure which demonstrates high hardness. Titanium

fabricated by DMD exhibited hardness of 458±10 HV compared to 120 to 240 HV by traditional manufacturing methods [71].

Open circuit potential (OCP) results indicated that overall the electrochemical behavior of pure titanium made by DMLD is similar to that of commercially pure titanium. However, the passive current density and corrosion rate show that DMLD titanium may exhibit higher corrosion resistance than titanium by traditional melting. The mechanisms of the pure titanium corrosion are suggested to be a result of the martensitic phase transformation because of rapid solidification. Small amounts of iron in titanium-based alloys improve the corrosion resistance of the alloy in Hank's solution [71]. A more noble OCP is suggested to be a result of the equiaxed microstructure [71].

Aluminum Metal Matrix Composites Via DMLD

The development of Al-MMCs with hard reinforcement particles distributed in a softer metal matrix has been evaluated with reinforcement particles like silicon carbide and titanium carbide [48, 49]. Al-MMCs can be manufactured with significantly increased yield and ultimate strengths by adding particles such as Al_2O_3, Al_3Ti, and $Ti B_2$ [7, 55, 60]. The addition of Si, SiC, Si_3N_4,TiC, and Mo-WC reinforcement particles can increase the bulk hardness and wear resistance [60, 72-74]. In addition, Al_20_3/TiO_2, $ZrO_2/Y2O_3$, TiC, Ni, Cr have also been investigated [75-77].

Chong *et al*. described the microstructure and wear properties of DMLD MMCs of Mo-WC on AA6061 [55]. In this work, the authors fabricated samples using a 2kW Nd-YAG laser with a scanning speed of 17 mm/s and power of 1400 W. The specimens were approximately 1mm in thickness with sufficient mixing due to the Marangoni flow effect. However, it was observed that the higher the carbide concentration, the less

effective the Marangoni flow effect was at mixing the materials. They observed epitaxial growth of dendrites on the partially melted surface of WC particles. In addition, wear resistance was studied by pin-on-disc abrasive wear testing. The Mo-WC particles in the powder formulation caused the MMC to exhibit significantly improved hardness and wear properties [55].

Corrosion properties of Al-MMCs have been examined for other fabrication methodologies. For example, SiC_5/5A06 aluminum MMCs fabricated by cerium conversion treatment have been used to improve the corrosion resistance of aluminum alloys [72]. Aziz *et al.* indicate that corrosion of the matrix alloy occurs slower than SiC_p/5A06 Al-MMCs due to the presence of intermetallics and crevices at the interface of the matrix. Based on potentiodynamic polarization of the SiC_p/5A06 Al-MMCs, Aziz *et al.* indicate that the anodic and cathodic processes are restricted by the formation of oxides/hydroxides and an Al-oxide film over the rest of the composite [72]. In addition, negative shifts in corrosion potential indicate that the cathodic branch of the polarization curves indicate cathodic inhibition of corrosion [72, 78]. The treatment also causes the pitting potential (E_{pp1}) to increase as a result of the formation of Al_2O_3 on the surface. However, they have reported that the SiC_p/5A06 Al-MMC indicated no effective improvement in corrosion resistance in comparison to the untreated matrix as a result of greater discontinuities in the matrix.

Mission of the Present Research

This research aims to assess the feasibility of fabricating titanium- and aluminum-based MMCs by direct metal laser deposition. This was done by investigating the microstructure, composition, hardness, wear and corrosion properties of Al-MMCs on the

surface of AA 5083 and AA 7075 and Ti-MMCs on Ti6Al4V. The MMC formulations are made from aluminum, titanium, tungsten carbide, and chromium carbide nickel superalloy powders. The processing conditions and details regarding the methods of analysis are presented in the following chapter.

CHAPTER II

METHODOLOGY

Direct Metal Laser Deposition

Direct Metal Laser Deposition (DMLD), as described in Chapter I, is a fabrication technique for creating MMC coatings or 3-D parts layer-by-layer. In this research, DMLD was performed with an ILT Inc.® Multi-Function Workstation. A 1 kW fiber-coupled diode laser from IPG Photonics®, generated a continuous wave beam with a 1070 - 1080 nm wavelength. The power, cooling, and control of the laser system were provided by peripheral units that allowed the laser processing parameters to be monitored. CNC 5-axis control provided precise (± μm) movement of the work piece relative to the laser beam. The Precitec® YC50 laser cladding head moved in the X and Z axis directions while the rotation and tilt control stage moved the work piece along the Y axis.

The laser beam was focused on the surface of the work piece using a 200 mm focal length objective lens integrated into the Precitec® YC50 cladding head with a 100 mm focal length collimation lens. A 400 micron fiber, provided by IPG Photonics®, was used for the fabrication of the aluminum composites which produced a theoretical 800 micron (0.032") spot. After damaging this fiber in an unrelated operation, an 800 micron fiber with a 1600 micron (.064") spot was employed for the fabrication of the Ti-MMCs. Also, a 0.5 mm coaxial powder delivery nozzle was used to deliver powder to the melt

pool. The powder assist gas flowed through the coaxial nozzle at 20 liter/min with a 50 liter/min flow of argon gas through the surrounding annulus which shrouded the melt pool from oxidation. Figure 9 shows the 1 kW fiber-coupled diode laser workstation and peripheral units used in this research.

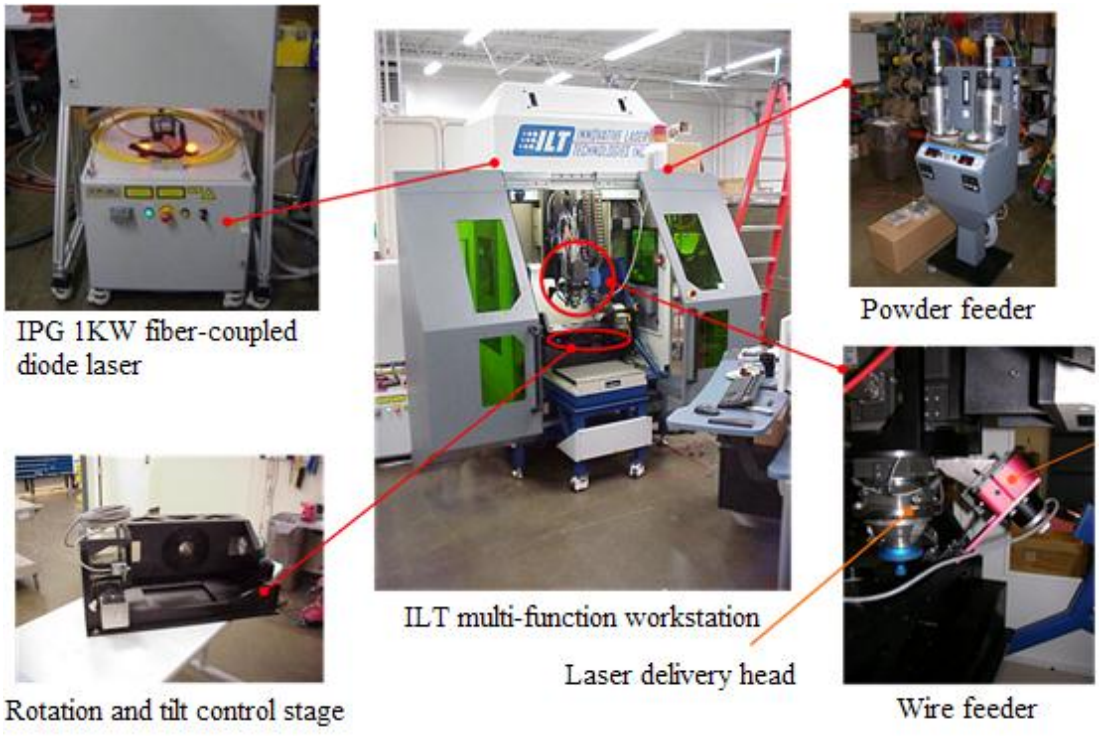

Figure 9. Fiber coupled diode laser system and peripherals at the University of North Dakota's Advanced Engineered Materials Center

Figure 10 presents the laser scanning strategy used to fabricate the MMCs. The Precitec® YC50 laser cladding head transversed across the samples in a left to right motion, with reference to the observer. The beam was programmed to turn on at the beginning of each trace and turn off once the trace had been completed. The YC50 cladding head would then move the hatch spacing distance specified in the program, before proceeding to trace in the opposite direction. This was done between 10 and 15 times to create a large MMC area. Each MMC coating was made with only one layer of deposition.

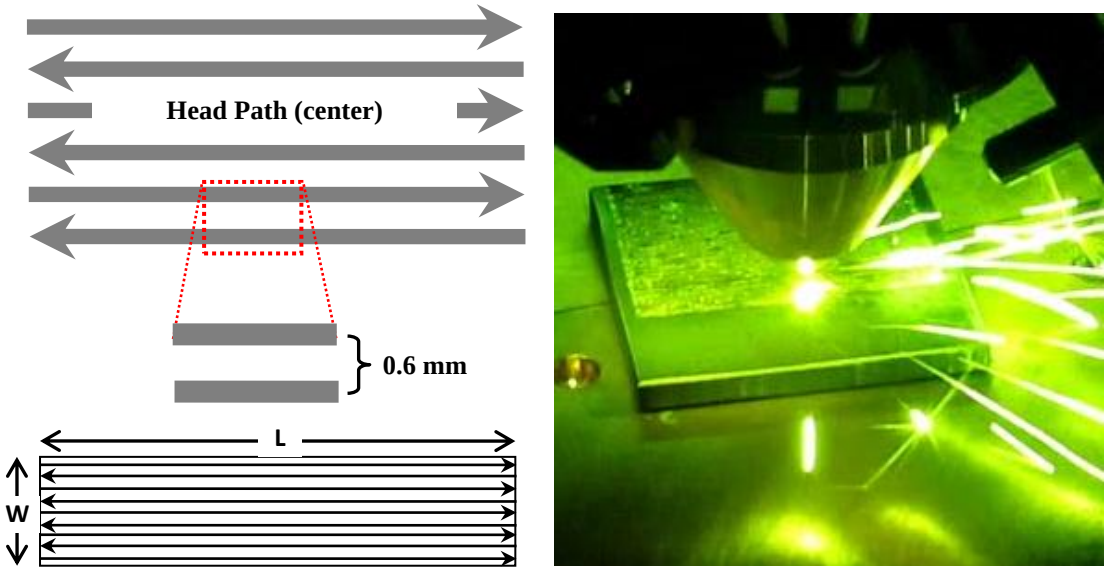

Figure 10. Laser scanning strategy employed for the fabrication of Ti- and Al-MMCs (a) and live image of the DMLD process used at the Advanced Engineered Materials Center (b).

Figure 10 also presents an image taken during the processing of a Ti-MMC. Observe the bright colored laser as it is emitted from the Precitec YC50 cladding head. The sparks are powder particles, not part of the molten melt pool that are bouncing off the specimen.

The ILT Inc.® Multi-Function Workstation allowed precise control over laser processing parameters. Laser power was varied between 500 W and 800 W while the cladding head moved with speeds between 800 and 1600 mm/min. Varying these parameters sample-to-sample created specimens that could be analyzed to determine if laser energy density had an effect on corrosion performance. Also, the powder feed rate, represented in % of maximum rpm was set at 3% for all MMCs. The parameters were chosen based on previous work which focused on determining the optimum processing parameters for achieving MMCs with adequate bonding to the surface of the substrate. The processing parameters used are described in Table 1.

Table 1. Specimen names and processing parameters

Sample Name	Substrate	Powder Composition	Laser Power (W)	Powder Feed Rate (%rpm)	Scanning Speed (mm/min)	Fiber spot size (μm)
6W6AL1	AA 7075	Al1	600	3	600	400
6W8AL1	AA 7075	Al1	600	3	800	400
6W10AL1	AA 7075	Al1	600	3	1000	400
7W13AL1	AA 7075	Al1	700	3	1300	400
7W16AL1	AA 7075	Al1	700	3	1600	400
7.5W15-3.0AL2	AA 5083	Al2	750	3	1500	400
7.5W15-2.0AL2	AA 5083	Al2	750	2	1500	400
8W15-3.0AL2	AA 5083	Al2	800	3	1500	400
8W15-2.0AL2	AA 5083	Al2	800	3	1500	400
Ti1-01	Ti6Al4V	Ti1	700	3	1400	800
Ti1-02	Ti6Al4V	Ti1	700	3	1000	800
Ti1-03	Ti6Al4V	Ti1	500	3	800	800
Ti1-04	Ti6Al4V	Ti1	800	3	1400	800
Ti2-01	Ti6Al4V	Ti2	700	3	1400	800
Ti2-02	Ti6Al4V	Ti2	700	3	1000	800
Ti2-03	Ti6Al4V	Ti2	500	3	800	800

Raw Materials

The powder formulations for the MMCs with aluminum or titanium matrices were made from Metco 54NS aluminum powder, Metco 4017 titanium powder, Metco 70C-NS chromium carbide powder and SM 5803 tungsten carbide nickel superalloy powder. The powders were acquired from Sulzer-Metco Inc. (Westbury, NJ). Figure 11 shows SEM images of each powder used in the formulations. All compositions were thoroughly mixed by shaking in a large container before laser processing. For Al-MMCs, quarter inch thick plates of AA 7075 and AA 5083 were used for the powder formulations *Al1* and *Al2* respectively, as shown in Table 2. Ti6Al4V plates, 6mm thick, were used as substrates for both formulations of Ti-MMCs.

Table 2. Composition of lightweight aluminum- and titanium-based metal matrix composite powder formulations

Comp	Aluminum, Metco 54NS (wt%)	Titanium, SM 4017 (wt%)	Tungsten carbide-Nickel Super Alloy, SM 5803 (wt%)	Chromium Carbide, Metco 70C-NS (wt%)
Al1	50	-	25	25
Al2	70	-	15	15
Ti1	-	50	25	25
Ti2	-	70	15	15

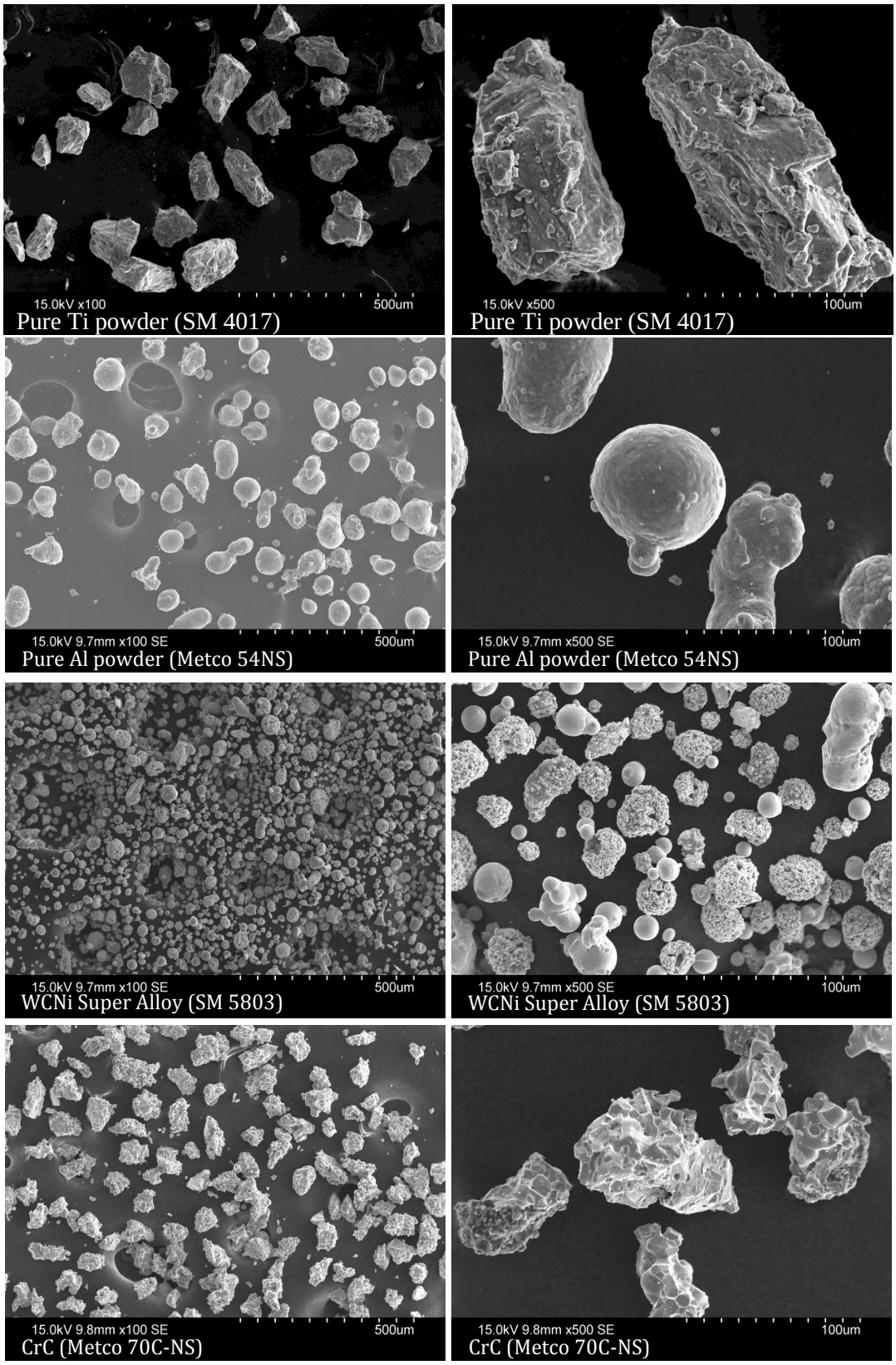

Figure 11. SEM imagery of as-received powder particles

Physical Characterization

Optical Microscopy

For optical microscopy, a LSM 5 Pascal Confocal Microscope by Carl Zeiss MicroImaging, Inc. (Thornwood, NY) was fitted with an AxioCam® MRc 5 camera in addition to several objective lenses ranging from 5x to 50x. Cross-sections of the specimens were prepared through standard metallurgical procedures. Al-MMCs were etched with Vilella's etchant. Ti-MMCs were etched with oxalic tint etchant to reveal the microstructure and analyze grain boundaries, phase boundaries, and inclusion distribution.

Scanning Electron Microscopy

The scanning electron microscope (SEM) employed in this research was a Model S-3400N made by Hitachi Science Systems, Ltd. (Pleasanton, CA). This type of electron microscope takes an image of a sample by shooting a high-energy beam of electrons at the surface of a sample in a raster scanning pattern. The interactions of this electron beam with the atoms in the sample's surface reveal critical information about the topography, conductivity, composition, and electrical properties of the specimen. The primary purpose of scanning electron microscopy was to obtain highly magnified images with high-resolution and to obtain chemical analysis of micron-sized areas.

In the Hitachi system, the electron source was a tungsten hairpin filament that used a three stage electromagnetic lens reduction optical system. In this research the accelerating voltage was 15 V_{acc}. Other parameters such as probe current, gun bias and working distance were determined by the auto-filament saturation function provided by the Hitachi system.

Energy Dispersive X-Ray Spectroscopy

Energy dispersive x-ray spectroscopy (EDS) is a common technique for identifying the elemental composition of materials that have been imaged in a SEM. In this research an EDS2004 system from IXRF Systems, Inc. (Houston, TX) with a Model 500 Analyzer was used. In this system, the electron beam traces across the sample generating X-ray fluorescence from the atoms in its path. The energy of the X-ray photons are characteristic of the element from which it was produced and may be plotted against known elemental electron-voltage to produce a spectrum with full quantitative analysis of the sample composition. In this research the Fast Map® function was used to trace an area and present a colored map of the distribution of elements in the surface.

Mechanical Characterization

The mechanical properties of the MMCs were evaluated in terms of microhardness, nanohardness, reduced elastic modulus and Taber Wear Index. Hardness is usually measured to determine the susceptibility of a material to localized plastic deformation as a result of some treatment or working condition. Reduced elastic modulus is an efficient means of determining the stiffness of thin films or coatings without performing a tensile test. Taber abrasion testing provides a manner to quantitatively compare the resistance to abrasive wear.

Nanoindentation Methodology

Depth sensing indentation or instrumented indentation is a method which continuously measures indentation load and displacement in order to achieve ultra-low-load indentation or nanoindentation. One of the primary advantages depth sensing indentation is that elastic modulus can be determined from the same data as hardness.

Instrumented indentation experiments were conducted using a Ubi 1 nanomechanical test instrument with a diamond Berkovich tip from Hystron Inc. (Minneapolis, MN). The tip area function was calibrated on a Fused Quartz sample with reduced modulus (E_r) = 69.6 GPa and hardness (H) = 9.25 GPa by performing a set of 81 indentations with maximum loads ranging from 100 μN to 1000 μN. Specimens were prepared by the standard metallurgical procedure of grinding on silicon carbide abrasive paper to 1200 grit followed by polishing down to 0.05 μm SiO_2 suspension.

Twenty-five indentations with 1000 μN loads were made at two different locations in each MMC. The loading rate was 1200 μN/s with 5 s loading and unloading periods. Unload occurred 10 s after the peak force was reached. Both sets of twenty five indentations were analyzed together to determine the average and standard deviations of hardness and reduced modulus.

The hardness and reduced modulus of the specimens were determined from depth-sensing indentation data using the multi-curve analysis option in TriboScan® version 8.1.1 (Hystron Inc, Eden Prarie, MN). This process for determining hardness and reduced modulus was in accordance with the standard method for indentation data analysis outlined by Oliver and Pharr [79]. First, the unloading curve is fitted with a power law relation. The *Upper Fit %* and *Lower Fit %* parameters were 95% and 20%, respectively. This indicates the portion of the unloading curve to fit the power law relation as presented in equation 2.1.

$$P = A\left(h - h_f\right)^m \tag{2.1}$$

Where P is the indentation load, h is penetration depth, h_f is the residual displacement after unloading, and A and m are parameters determined by the fitting procedure. Finding

the power law relation is the first step in calculating the hardness and reduced modulus, E_r. The derivative of this relationship with respect to penetration depth at max load yields the contact stiffness, *S*.

$$S = \left.\frac{dP}{dh}\right|_{h_c} \tag{2.2}$$

Contact depth, h_c, is then calculated by the relationship in equation (2.3).

$$h_c = h_{max} - 0.75 \cdot \frac{P_{max}}{S} \tag{2.3}$$

Hardness is calculated with equation (2.4) where $A(h_c)$ is defined as the area function.

$$H = \frac{P_{max}}{A(h_c)} \tag{2.4}$$

Reduced modulus is calculated with equation (2.5).

$$E_r = \frac{\sqrt{\pi}}{2\sqrt{A(h_c)}} \cdot S \tag{2.5}$$

Microindentation Methodology

Microhardness was observed using a Mitutoyo® HM-112 microhardness test machine. The testing system was designed to find Vickers hardness by dividing the force applied during indentation by the surface area of an indentation left by the indenter. The area of indentation is found using the average diagonal length across the indentation when a specific load is applied. The diamond indenter used had a face-to-face angle of 136 degrees as shown in Figure 12.

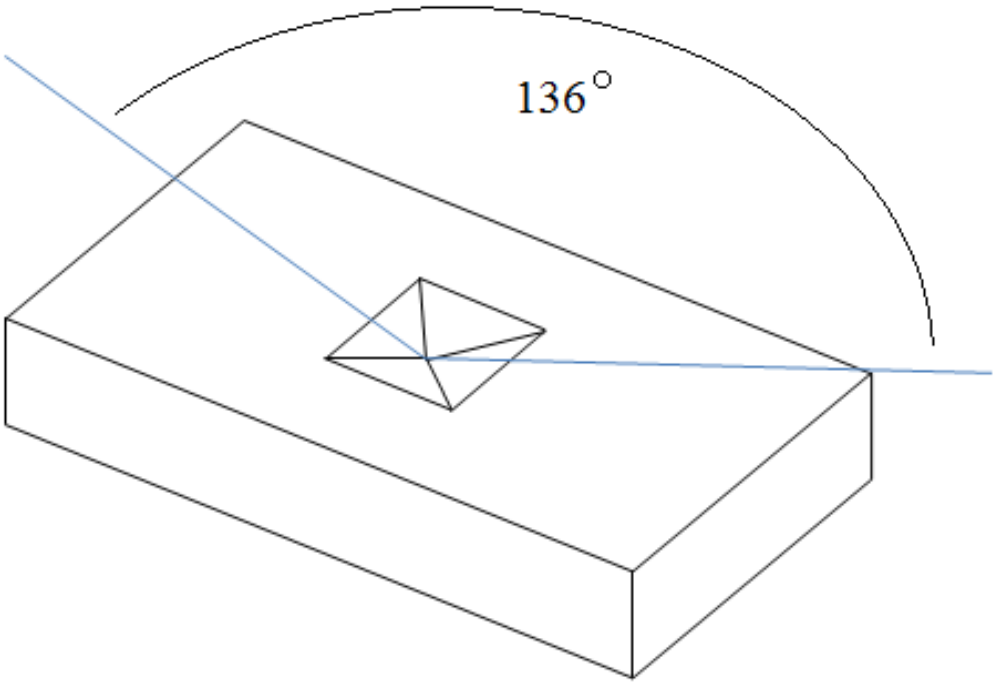

Figure 12. Indentation for measuring Vickers hardness through microindentation

In this research, an indentation load of 100 g with a dwell time of 15 seconds was used during indentation. By determining d1 and d2 using the optics on the Mututoyo HM-112 as shown in Figure 13, Vickers hardness could be determined from the equation relating HV to indentation force and indentation area as follows.

$$HV = k\frac{F}{S} = 0.102\,\frac{F}{S} = 0.102\,\frac{2F\sin\frac{\theta}{2}}{d^2} = 0.1891\frac{F}{d^2} \qquad (2.6)$$

Where k is a constant ($k = 1/g_n = 0.102$), F is the test force in N, surface area S is given in mm^2, d is the average length of d1 and d2, θ is the face-to-face apex angle of the diamond indenter and g_n is the standard acceleration due to gravity.

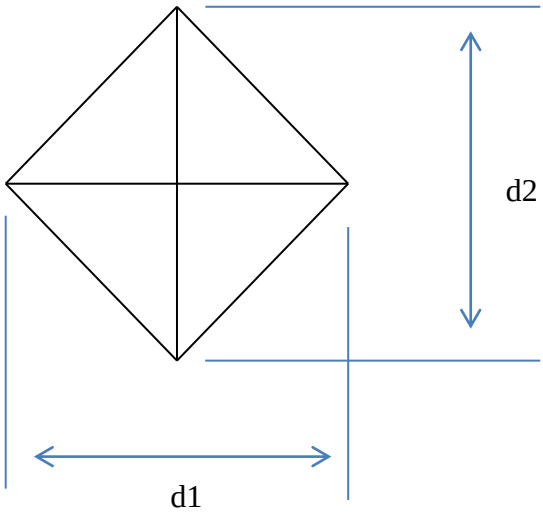

Figure 13. Determining d1 and d2

Taber Rotary Abrasion Testing

Wear tests were performed using a Taber® Rotary Platform Abrasion Tester Model 5135. This instrument is designed to test a material's resistance to rubbing abrasion. The tests were performed with two 500 g loads at 2000 cycle intervals. Taber Industries CS-17 standardized abrasion test wheels were used and refaced after every 1000 cycles. Mass loss was determined and thus the Taber Wear Index (TWI) may be calculated, as shown in equation 2.7, by the weight loss method where N_{cycles} represents the total number of cycles performed.

$$TWI = \frac{Wt_{lloss} \cdot 1000\ Cycles}{N_{cycles}} \tag{2.7}$$

Electrochemical Characterization

Preparation of Aqueous Solution

To simulate sea water, 0.5 M NaCl was used for all electrochemical tests. The solution was freshly prepared prior to testing with demineralized water. To make the solution, 29.22 g NaCl was thoroughly mixed with 1 L demineralized water.

Sample Preparation

Each specimen was sectioned using an Isomet® low speed wafering saw so as to not disturb the surface of the specimen. The surface area of each sample was cut to approximately 1.0 cm^2. Each sample was connected to a copper wire using Loctite® thermal epoxy. The edges of the specimens were painted with Amercoat® epoxy paint to prevent crevice corrosion. Specimens were then mounted in epoxy resin with the copper wire protruding from resin in a glass tube to prevent immersion of the wire in aqueous solution. Samples were polished to 1200 grit with carbide abrasive papers and washed with isopropyl alcohol then ultrasonically rinsed with demineralized water prior to testing.

Electrochemical Cell

The electrochemical cell is an important part of the experimental set up because it provides the environmental conditions in which the measurements are to be performed. It must allow the development of a stable reference with a known potential to aide in the control and measurement of the test. A Gamry PC4 potentiostat (Gamry Instruments, Warminster, PA) was used for sample monitoring. The corrosion properties of the specimens were studied in naturally aerated aqueous 0.5 M NaCl solution at room temperature under ambient conditions.

For open circuit potential (OCP) and polarization resistance (R_p) a three electrode cell was used with the specimen as the working electrode and a saturated calomel electrode (SCE) as the reference electrode. The SCE allows accurate measurement of the potential applied to the working electrode. In this research, a SCE, which contains

potassium chloride, was used because the experiment is being performed in a Cl^- rich environment of NaCl.

Also, a platinum mesh was used as the counter electrode. The highly corrosion-resistant platinum mesh counter electrode prevented the chemistry of the solution from changing as a result of a corroding counter electrode. The working electrode (specimen to be tested) was placed approximately 2 – 4 mm away from the reference electrode which provides a stable "reference" against which the applied voltage may be measured. Also, the testing was performed in a ferritic cage to shield from external radiation which might interfere with the potential measurement.

Cyclic potentiodynamic polarization was performed using a slightly different electrode configuration. Instead of directly exposing the tip of the reference electrode to the surface, a Luggin capillary was used to provide a salt water bridge for the electrolyte to the reference electrode. The reference electrode was submerged in a separate beaker of fresh 0.5 M NaCl to allow the reference electrode to provide an accurate reference during this destructive test.

Figure 14 shows the electrochemical cells used for both open circuit potential and polarization resistance in (A) and cyclic potentiodynamic polarization in (B). The copper wire attached to the working and counter electrode are connected to the Gamry system which is not pictured. Spacing of 2 – 4 mm can be observed between specimen and SCE or Luggin capillary.

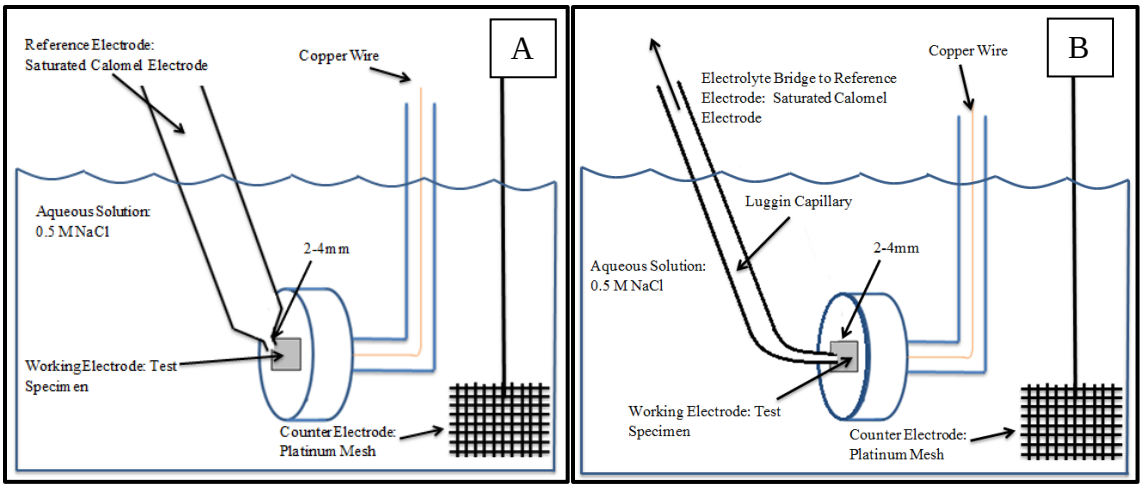

Figure 14. Electrochemical cells for monitoring OCP, Rp (A) and Potentiodynamic Polarization (B)

Open Circuit Potential

The trends in OCP and R_p were monitored every 2.5 h for 25 h with the Gamry PC4 potentiostat. OCP was monitored at each interval for 240 s. Density and equivalent weight of aluminium were 2.78 g/cm^3 and 8.9934 g, respectively. Density and equivalent weight of titanium, on the other hand, were 4.51 g/cm^3 and 11.963 g, respectively. Freshly prepared specimens were exposed to a new electrolyte for 30 min prior to taking measurements in order to let the cell reach steady-state.

Open circuit potential (OCP) is the intersection point of the anodic and cathodic regions on the potential vs. current density curve and is sometimes called the corrosion potential. Varying potential values can result from changes in either the anodic or cathodic process, or both. However, in this research, changes in cathodic kinetics are unlikely; therefore, variations in OCP are considered to primarily reflect changes in anodic kinetics. Thus, an increase in OCP likely results from a decrease in the anodic passive current density and reflects the development of a more protective surface film.

Conversely, a decrease in the OCP likely results from an increase in the passive current density, which reflects a less protective surface film.

Polarization Resistance

Polarization resistance (R_p) is a method of electrochemical examination used to estimate corrosion resistance of specimens; ASTM G59-97 was followed. Again, the Gamry PC4 potentiostat was used with the same three electrode electrochemical cell that was used for OCP. R_p data was collected in sequence with OCP therefore; OCP and Rp could be collected from the same specimen. To determine R_p, potential was scanned at 0.125 mV/s over a range of ± 25 mV (vs. OCP). *Rp* ($\Omega \cdot cm^2$) was then analysed using CorrView® software from Scribner Associates, Inc., Southern Pines, NC.

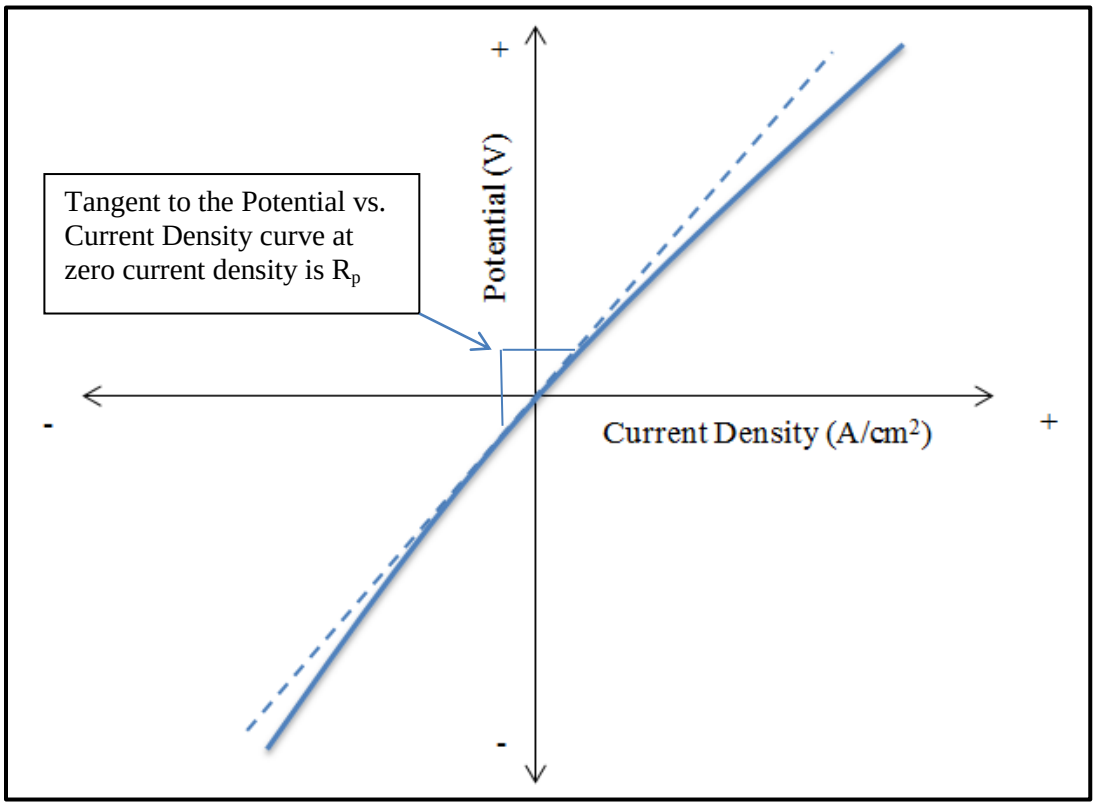

Figure 15. Determining R_p by linear polarization

The polarization resistance or R_p of the specimen is defined as the slope of the potential (voltage) vs. current density curve at OCP, as shown in Figure 15 and described in equation 2.8. The rate of corrosion is inversely proportional to polarization resistance which serves as a simple method to rank materials in order of resistance to general corrosion.

Equation 2.8 describes mathematically the slope of the potential per current density when the current density is zero.

$$R_p = (\frac{\partial \Delta E}{\partial i})_{i=0, dE/dt \to 0} \tag{2.8}$$

where E is potential (V) and i is the current density (mμA/cm^2). Finding R_p (ohm-cm^2) allows the determination of corrosion current density ($i_{corr,}$). The corrosion current density is related to polarization resistance by the Stern-Geary coefficient, B, in equation 2.9.

$$i_{corr} = 10^6 \frac{B}{R_p} \tag{2.9}$$

The Stern-Geary coefficient is determined from anodic and cathodic Tafel slopes, b_a and b_c respectively as described in equation 2.10. The units of the Tafel slopes are V.

$$B = \frac{\beta_a \beta_c}{2.303(\beta_a + \beta_c)} \tag{2.10}$$

Corrosion rate (CR, mm per year) can be determined from corrosion current density, equivalent weight and density of the material.

$$CR = 3.27 \times 10^{-3} \frac{i_{corr}\, EW}{\rho} \tag{2.11}$$

It can be seen that R_p is inversely proportional to corrosion rate. Thus, R_p can be used to make relative comparisons between specimens. Instead, corrosion rates were determined from cyclic potentiodynamic polarization curves where appropriate.

Cyclic Potentiodynamic Polarization

Potentiodynamic polarization tests were performed in the 0.5 M NaCl solution at room temperature in the naturally aerated condition, as per ASTM Standard G5-94. Specimens were exposed to a fresh electrolyte solution for a period of 60 min prior to testing. The Gamry-PC4 potentiostat was again used for specimen monitoring. The potential was scanned from 1.0 V below the corrosion potential at 0.3 mV/s in the anodic direction until a potential of 1.6 V was reached for aluminum and Al-MMC samples. Scanning was performed between 0.5 V and 2.5 V for Ti and Ti-MMC samples. Titanium specimens were scanned to a higher potential to better observe the occurrence of pitting.

Polarization of the specimen at voltages close to the open circuit potential can reveal a lot of information about the electrochemical properties of the specimen. Figure 16 presents a theoretical polarization curve. Below the corrosion potential the specimen is undergoing a cathodic reaction. As the specimen reaches the corrosion potential, however, the reaction becomes anodic as the potential crosses a corrosion current density of zero. By monitoring the potential, one can determine the slope of the potential vs. current density for the anodic and cathodic reactions. The intersection of these slopes is termed the corrosion current. Corrosion current can be related to corrosion rate by equation 2.11 and is called Tafel analysis.

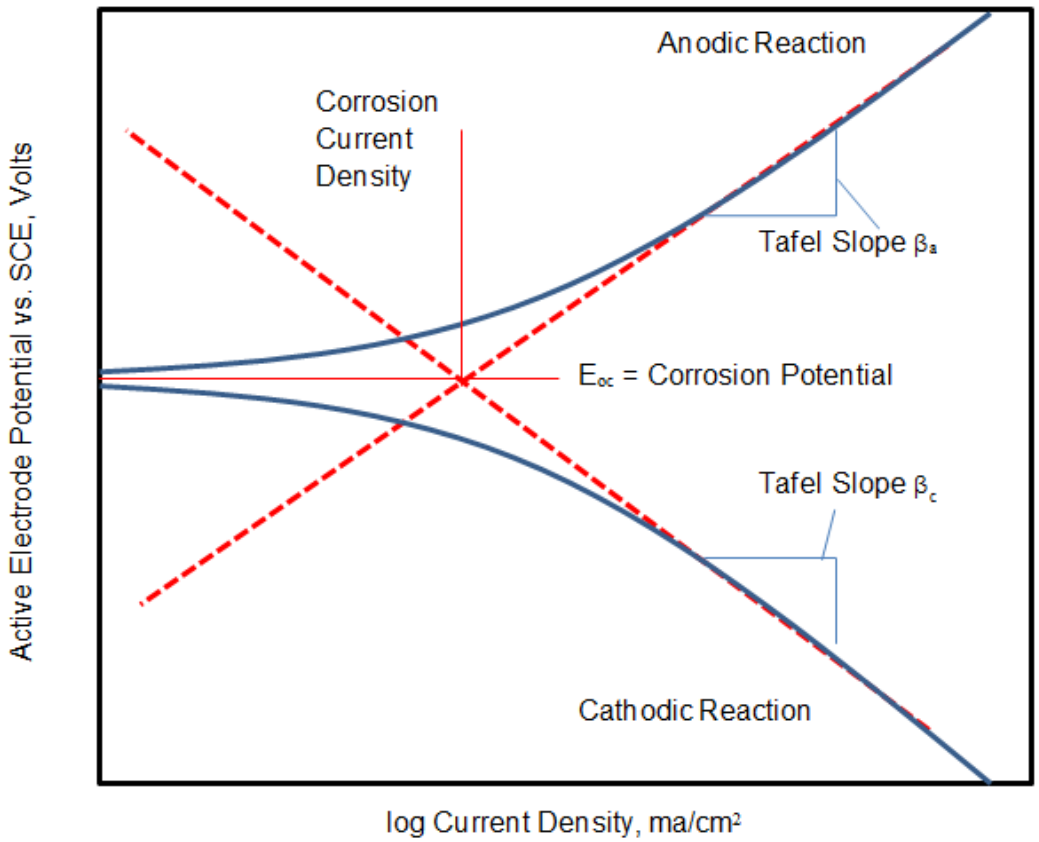

Figure 16. Hypothetical cathodic and anodic polarization diagram

Cyclic polarization is used to determine the susceptibility of specific materials to pitting corrosion. When the potential is swept in forward and reverse scans, the observation of hysteresis between values of starting OCP and size of the loop indicate the amount of pitting on the surface. Figure 17 presents an idealized cyclic polarization curve with electrode potential (V) as a function of current density. In general, the lower the corrosion current, the lower the corrosion rate. In addition, pitting can be determined from this type of analysis by observing the behavior of the curve on the reverse scan. Typically, if the potential behaves with hysteresis causing the reverse potential to cross the passive current density, the material exhibits pitting. If, however, the curve never intersects the original passive current density, no pitting occurs.

As the material is scanned in the forward direction it exhibits cathodic behavior until OCP is reached as described previously. After this point, the curve becomes anodic and will eventually reach a passive current density where increasing potential does not correspond to an increase in current density at the specimen surface. The pitting potential (E_{pp1}) is reached when an increase in potential again produces an increase in current density. The scan will eventually reach an apex potential (1.6 V for Al alloys and 2.5 V for Ti alloys) upon which the reverse scan begins. The point at which the reverse curve intersects the passive current density is the repassivation potential (E_{pp2}). E_{pp1}-E_{oc} yields the pitting growth resistance which indicates the resistance of a specific material to pit formation. E_{pp1}-E_{pp2} yields the pit nucleation resistance which describes how easily the material is repassivated after pitting begins.

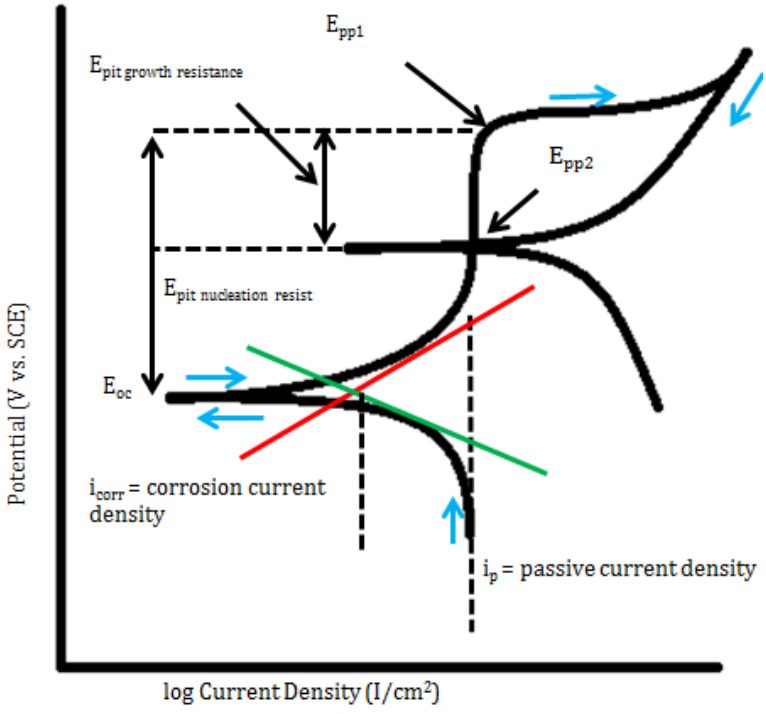

Figure 17. Theoretical cyclic potentiodynamic polarization curve

CHAPTER III

CHARACTERIZATION OF TITANIUM-BASED METAL MATRIX COMPOSITES

Physical Characterization of Ti-MMCs

The top surfaces of the titanium-based metal matrix composites (MMC) were visually inspected and subsequently cross-sectioned to examine the micro and macrostructures using optical and scanning electron microscopy. Typical top surface macrostructures of the MMCs deposited on Ti6Al4V are presented in Figure 18. The powder compositions, *Ti1* and *Ti2*, are given in Table 2.

Figure 18. Macrostructure of Ti1-MMCs on Ti6Al4V substrate

The MMCs exhibit slight variations in thickness with very hard and rough surfaces due to the presence of carbide reinforcing particles in the MMC formulations. During the process, the metal powder and a small portion of the surface is melted by the laser beam. Thermal gradients in the melt pool promote mixing of the molten powders before they are rapidly quenched by the surrounding inert gas flow provided by the ILT Multifunction Workstation. This produces a MMC that exhibits minimal dilution of the substrate. This is confirmed by energy dispersive X-ray spectroscopy (EDS) which is presented later in this section.

Figure 19 presents the cross-sectional microstructure of sample *Ti1-01* fabricated in this research. The microstructure indicates that the substrate exhibits grains of primary

α in a matrix of transformed β containing acicular α. Near the surface, it is observed that the structure is primary α in a matrix of α' (martensite). This is due to rapid cooling rates experienced near the surface of the material during the direct metal laser deposition (DMLD) process. Phase transformations can be either diffusion-controlled or diffusionless. In the case of martensitic transformations, the cooling occurs quickly enough to prevent diffusion-controlled transformations which result in the existance of nonequilibrium martensitic phases in the alloy.

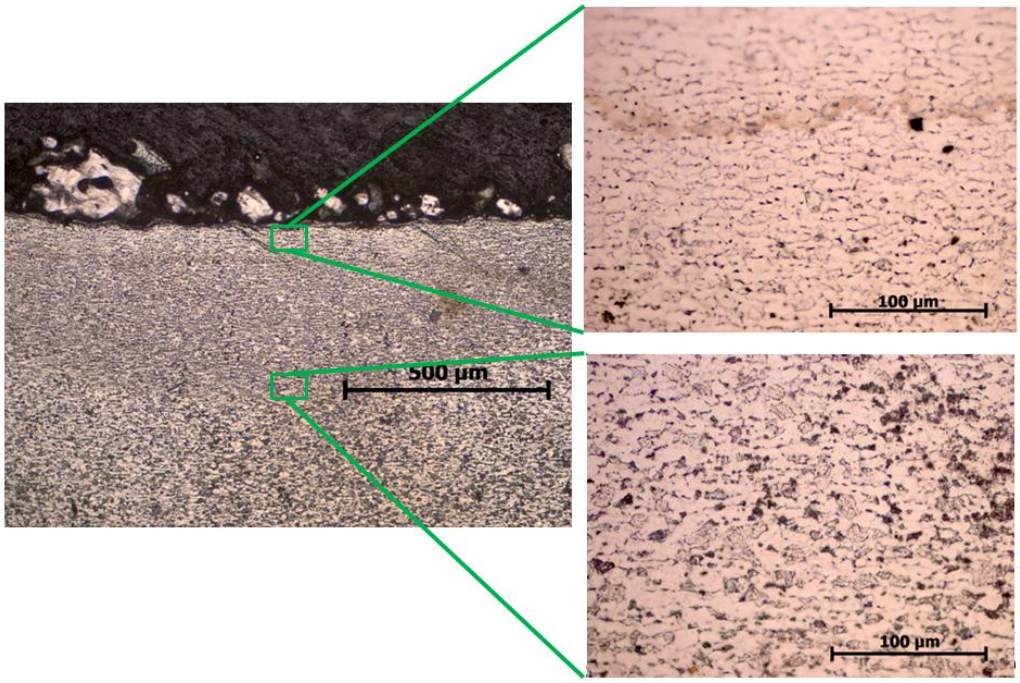

Figure 19. Microstructure of Ti1-MMC on Ti6Al4V

Energy dispersive X-ray spectroscopy (EDS) mapping indicates a high level of carbide reinforcing particles in the MMCs. Figure 20 and Figure 21present EDS mapping for *Ti1-* and *Ti2-MMCs*, respectively. In each sample, the fusion boundary zone can clearly be defined by the difference in contrast between the MMC and the parent alloy. The red color indicates the presence of carbon and is representative of the phenolic resin used to mount the samples. Individual element maps are shown in Appendix A.

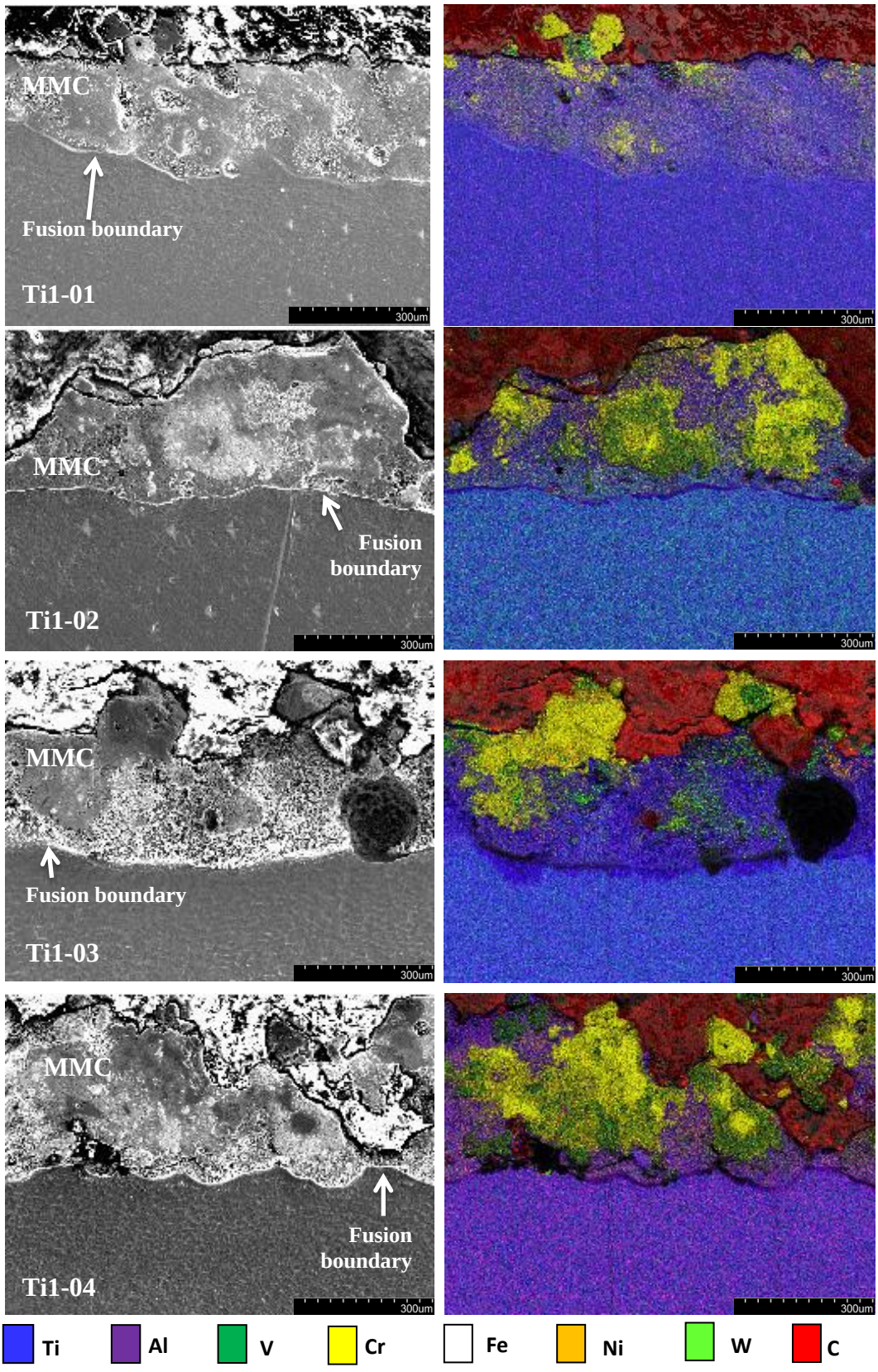

Figure 20. EDS compositional mapping for Ti1-MMCs on Ti6Al4V

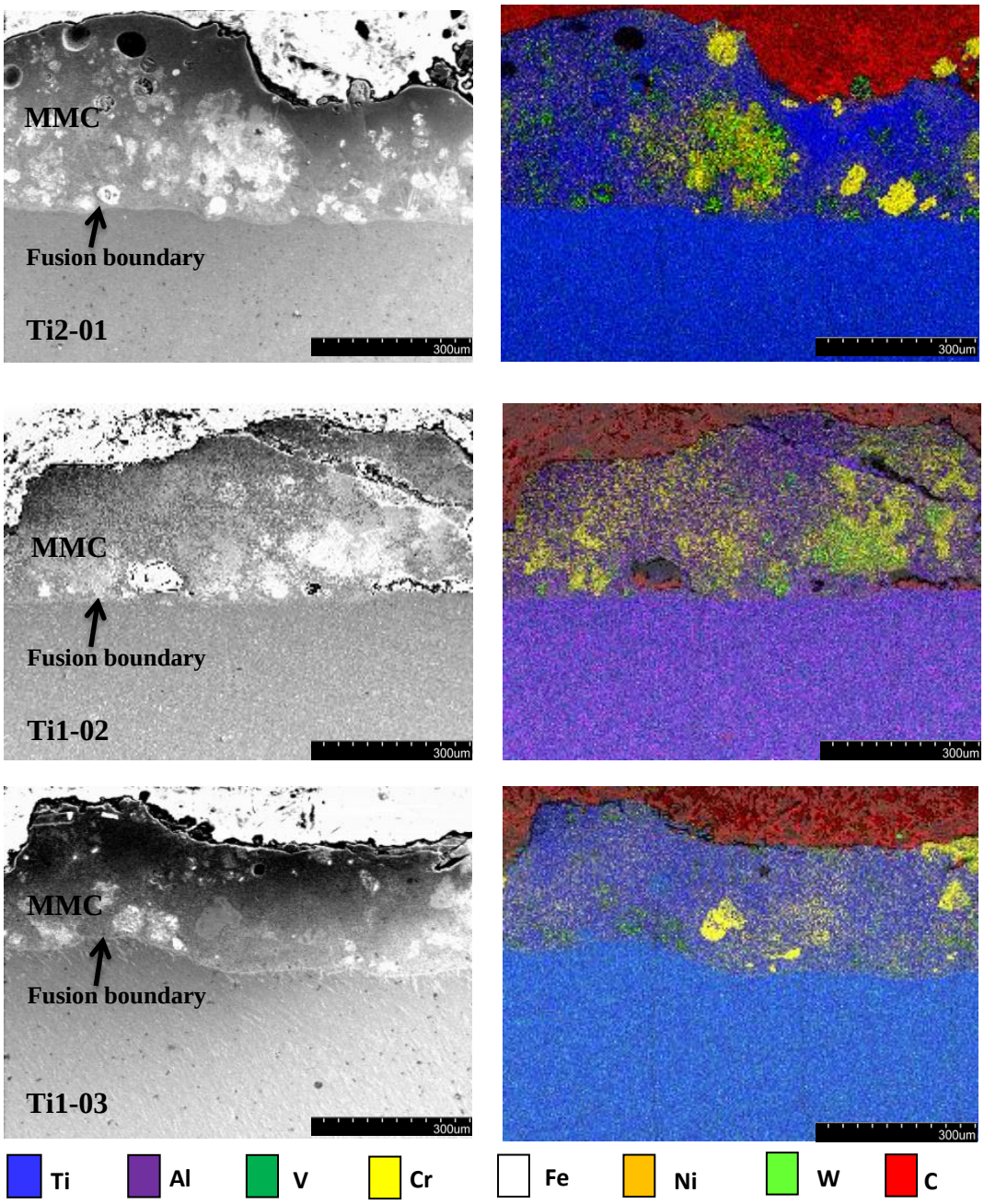

Figure 21. EDS compositional mapping for Ti2-MMCs on Ti6Al4V

Quantitative analysis of the EDS data further indicates the presence of CrC and W-C-Ni superalloy as observed in Table 3. MMCs with composition *Ti1* (50 wt% Ti powder, 25 wt% CrC and 25 wt% W-C-Ni superalloy) indicated a titanium matrix with levels ranging from 29% to 58%. Composites from composition *Ti2* (70 wt% Ti powder,

15 wt% CrC and and 15 wt% W-C-Ni superalloy) indicated similar levels of titanium content ranging from 35 wt% to 56 wt%. According to the powder formulation there should be 75 wt% titanium content in the *Ti2*-MMCs. This discrepancy in the data could result from differences in elemental identification as a result of overlapping peaks in energy spectra as frequently common to EDS analysis. However, in this case, it is much more likely to be a result of insufficient mixing of powders during powder injection to the melt pool. This could be caused by differences in particle densities.

Table 3. Ti1- and Ti2-MMC EDS composition analysis

	EDS Elemental Composition (wt%)							
Sample	Ti (wt%)	Al (wt%)	V (wt%)	Cr (wt%)	Fe (wt%)	Ni (wt%)	W (wt%)	C (wt%)
Ti1-01	58	5	0	14	0	3	7	12
Ti1-02	29	1	0	23	0	9	24	14
Ti1-03	37	1	0	19	0	5	21	17
Ti1-04	30	2	0	21	1	9	25	13
Ti2-01	49	1	0	14	1	6	17	12
Ti2-02	35	1	0	23	1	7	18	16
Ti2-03	56	1	0	14	0	4	1	14
Ti6Al4V	90	8	1	0	0	0	0	0

The imagery presented in Figure 20 and Figure 21 also indicates varying thicknesses throughout the MMC. The carbide reinforcing particles and have a propensity to cluster together in the composite causing nonhomogeneous composition. The composition *Ti1* appears to have a more rough appearance than the *Ti2* specimens. This could be as a result of a smaller proportion of CrC and W-C-Ni superalloy particles in the *Ti2* samples.

Mechanical Evaluation of Ti-MMCs

For many industrial applications it is important to acquire understanding of the mechanical properties of DMLD structures. The mechanical properties of the MMCs were studied by micro and nanohardness, reduced modulus and taber wear index.

Nanoindentation

Nanomechanical testing was carried out to determine nanohardness and reduced modulus of the MMCs. The force vs. displacement curves and hardness and reduced modulus vs. indentation depth curves are presented in Appenxix B. The Ti-MMCs indicated a significant increase in hardness and reduced modulus over bulk Ti6Al4V, likely due to the carbide reinforcing particles in the composite formulations. *Ti2-01*, *Ti2-02* and *Ti2-03* showed an average hardness of 13.1 GPa (1336 HV), 27.9 GPa (2845 HV) and 40.1 GPa (4089 HV), as observed in Table 4. This is in agreement with the microhardness indentation results which are presented in the next section.

Table 4. Nanomechanical testing of Ti1 and Ti2 MMCs

Specimen		Contact Depth (nm)	Reduced Modulus (GPa)	Hardness (GPa)
Ti1-01	Average	68.9	158	5.8
	Standard Deviation	14.4	49	2.3
Ti1-02	Average	67.6	122	5.6
	Standard Deviation	9.6	19	1.3
Ti1-03	Average	66.2	137	5.9
	Standard Deviation	9.9	19	1.6
Ti1-04	Average	70.2	143	5.7
	Standard Deviation	17.3	65	2.2
Ti2-01	Average	39.5	209	13.1
	Standard Deviation	6.8	45	4.6
Ti2-02	Average	42.0	263	27.9
	Standard Deviation	9.9	63.8	15.3
Ti2-03	Average	33.8	355	40.1
	Standard Deviation	6.2	64	18.2
Ti6Al4V	Average	63.5	126	4.1
	Standard Deviation	9.1	13	0.7

Microindentation

Figure 22 presents the microhardness indentation strategy and results for sample *Ti1-01*. The plots for all other specimens may be found in Appendix C. Indentations were made in the MMC region, fusion boundary region (FB), base metal. Based on the elevated hardness observed in the MMC, it is evident that the MMCs contain carbide particles. The variation in measured hardness is a result of the relative composition of the MMC. Thus, some of the areas in the MMC coating will exhibit the hardness of the titanium matrix and some will exhibit the higher hardness of carbide reinforcing particles.

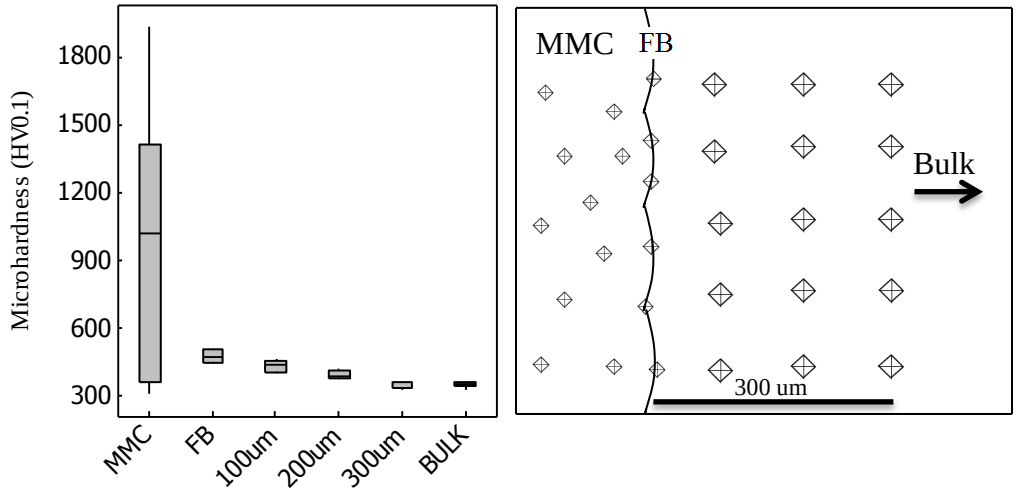

Figure 22. Microindentaion strategy and results for Ti1-01

Further evidence of elevated hardness due to carbide reinforcing elements can be seen in Figure 23 which presents an optical micrograph of several indentations made in the Ti-MMC. It can be observed from the image that there are large indentation marks and small indentation marks located in close proximity to each other. The smaller impressions indicate the presence of carbide particles while the larger indentations indicate regions of matrix.

The separation of matrix carbides may indicate that the powders were not sufficiently mixed to create a compositionally homogeneous MMC with carbide reinforcing elements discretely scattered throughout the matrix. It appears that the carbide particles tend to stick together and form areas of densely scattered carbide elements. There is also evidence of this in the EDS analysis as presented previously.

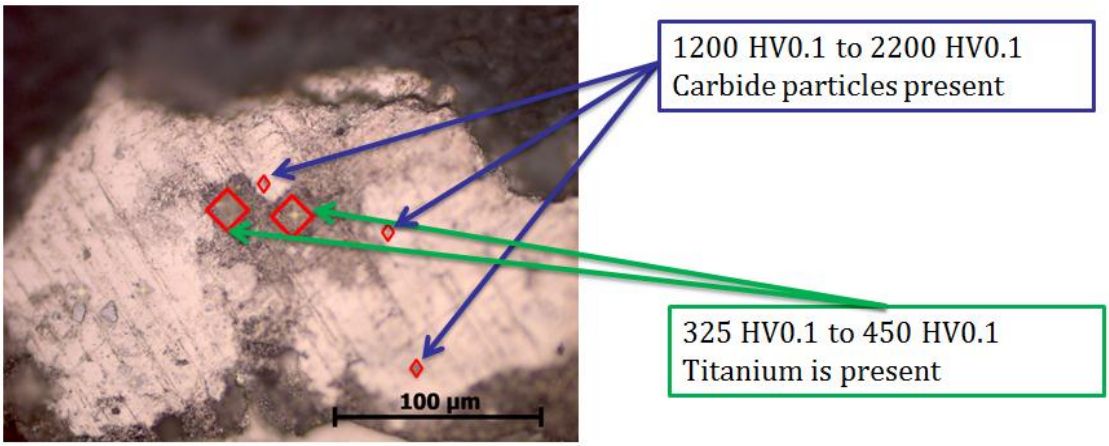

Figure 23. Optical microscopy of microindentations

A comparison between average microhardness observed in each Ti-MMC and bulk Ti6Al4V is presented in Figure 24. This figure describes a 95% confidence window for the mean hardness. In sample *Ti1-01* the sample showed hardness values as high as 1400 HV0.1 and as low as 325 HV0.1 for bulk Ti6Al4V. Sample *Ti1-02* indicated hardness values in the MMC coating of as high as 2200 HV0.1. Overall, the Ti-MMCs exhibited an increase of between 200 and 350% in average microhardness over the Ti6Al4V substrate. There was no significant difference in average hardness between compositions *Ti1* and *Ti2*. However, there was a slight reduction in maximum hardness. This is again due to more thorough mixing of carbide reinforcment particles in the *Ti2* MMCs.

The variation in observed microhardness was smaller in the *Ti2* sample as confirmed by a two sample F test for variance. This may be the result of a more consistent clad due to a lower concentration of carbides in the formulation leading to better mixing of the powders in the melt pool.

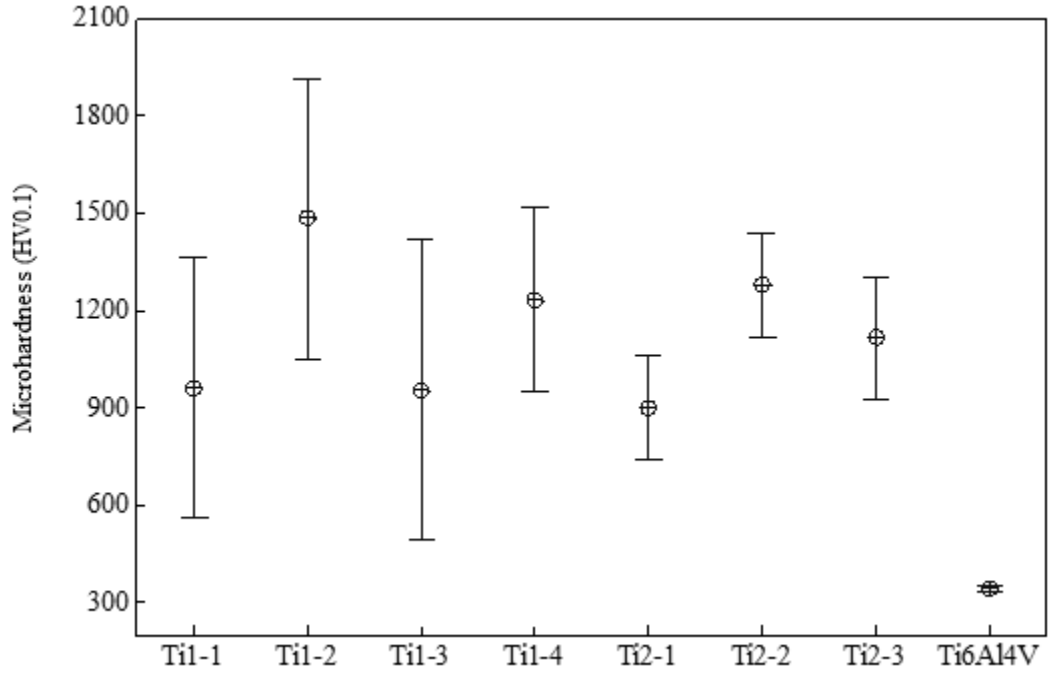

Figure 24. Average microhardness of Ti-MMCs

Taber Wear Index

Taber rotary platform abrasion testing was performed using CS-10 Calibrase ® and refacing discs while refacing after every 1000 cycles. Mass loss was measured every after 2000, 4000, and 6000 cycles. Specimens were polished with 600 grit abrasive paper prior to testing to ensure similar contact areas.

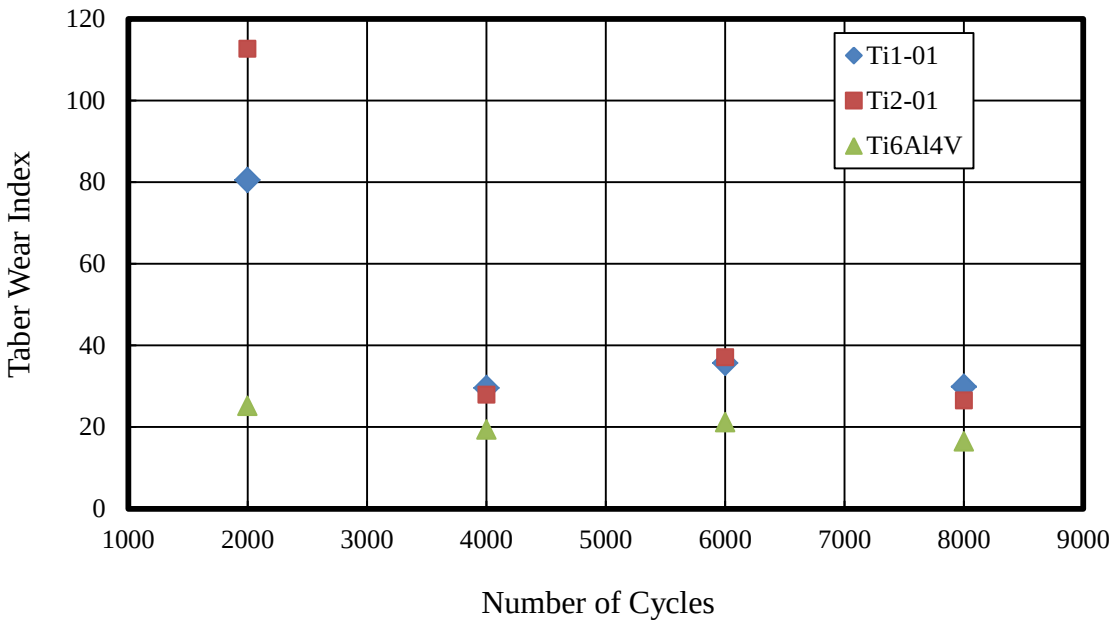

Figure 25. Taber Wear Index (TWI) for Ti1-01, Ti2-01, and Ti6Al4V

A 1000 g load was applied to the abrasive wheels causing rub-wear action, or sliding rotation, on the surface of the specimen. A vacuum system removed debris during testing. Figure 25 presents the Taber Wear Index (TWI) as calculated by Equation 2.7 for Ti1-01 and Ti2-01. After 2000 cycles the Ti1-01 and Ti2-01 composites showed an increase in the TWI of 219% and 350% respectively. TWI of the Ti-MMCs significantly dropped after 2000 cycles. After 4000 cycles the TWI, for both compositions of Ti-MMC appear to remain relatively constant until 8000 cycles, fluctuating between 29.5 and 37.0 respectively. Thus, after 4000 cycles the specimens exhibited between 52% and 75% increase in TWI. The poor wear performance may be a result of poor bonding between the hard and dense carbide reinforcing particles and the matrix. However, this research does not provide any supporting microscopy or other observations to confirm this conclusion. This is an area that should be examined in future work.

Corrosion resistance of Ti-MMCs

Open Circuit Potential

Open Circuit Potential (OCP) is the intersection point of the anodic and cathodic curves. Increasing OCP likely results from a decrease in the anodic passive current density and, thus, reflects the development of a more protective surface film. Conversely, a decrease in the OCP likely results from an increase in the passive current density, which reflects a less protective surface film.

The titanium-based metal matrix composites *Ti1-01*, *Ti1-02*, *Ti1-03*, and *Ti1-04* exhibit more negative open circuit potentials by about 82.3, 122, 52.2, and 68.4 mV respectively, compared to Ti6Al4V. This is evidence that the MMC structures do not develop a surface film that is as protective or noble as Ti6Al4V. However, the difference is relatively insignificant when compared to the OCP of 5xxx series aluminium alloys like AA 5083 and AA 5456. Figure 26 shows OCP for *Ti1* and *Ti2* MMCs in comparison to Ti6Al4V and several 5xxx series aluminium alloys.

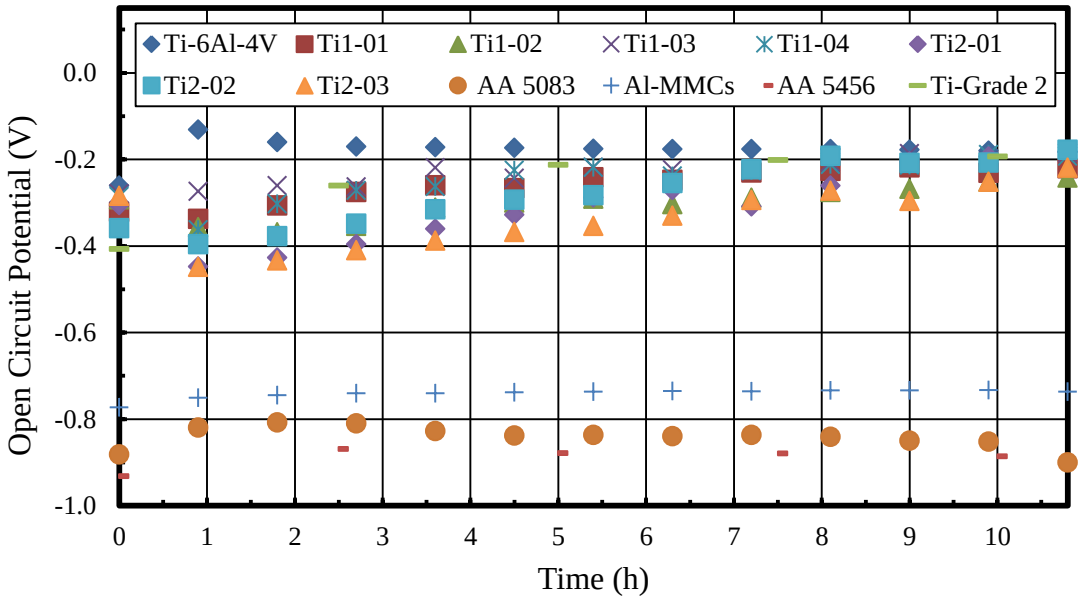

Figure 26. Open circuit potential for MMCs of composition Ti1 and Ti2 in comparison to Ti6Al4V, Grade 2 Titanium, AA 5083, and AA 5456 alloys

Polarization resistance

Figure 27 presents the polarization resistance (R_p) for the Ti-MMCs. The samples show a significant reduction in polarization resistance from the substrate. This decrease in R_p corresponds to an increase in corrosion rate over the untreated Ti6Al4V substrate. Ti6Al4V showed a constant polarization resistance over the 10 h immersion with an average resistance of 5.85 MΩ·cm^2. The *Ti1*- and *Ti2*-MMCs, while also constant, indicated averages between 10.0 kΩ·cm^2 and 17.8 kΩ·cm^2 for *Ti1-02* and *Ti1-01*, respectively. This is a significant reduction in polarization resistance which directly corresponds to an increase in corrosion rate. However, the Ti-MMC samples behaved similarly to what was observed for 5xxx series aluminum alloys immersed in the same solution of 0.5 M NaCl.

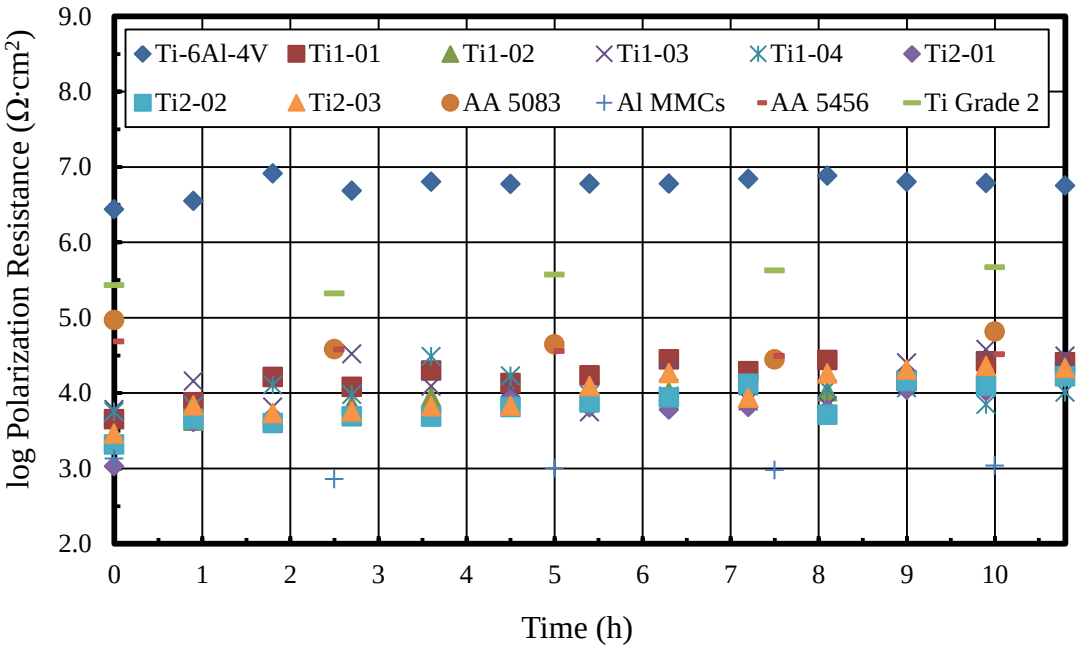

Figure 27. Polarization resistance for MMCs of composition Ti1 and Ti2 in comparison to Ti6Al4V, Grade 2 Titanium, AA 5083, and AA 5456 alloys

Cyclic Potentiodynamic Polarization

Figure 28 presents the cyclic potentiodynamic polarization curves of *Ti1* samples immersed in 0.5 M NaCl solution. The behavior of the *Ti1* samples show similar trends in behavior as constant potential is applied to the sample in the electrochemical cell. The corrosion potential is -0.25 ± 0.05 V for all seven Ti-MMC samples. The Ti6Al4V sample, however, shows a corrosion potentitial of -0.46 V. Furthermore, the behavior of the curve after it reaches an apex potential of 2.5 V above OCP indicates that no pitting exists in the material. This is evident by observing that the reverse scan does not intersect the forward scan near passive current density. It can be said that the pit nucleation resistance is less than 0, thus indicating that no pitting is occuring on the surface.

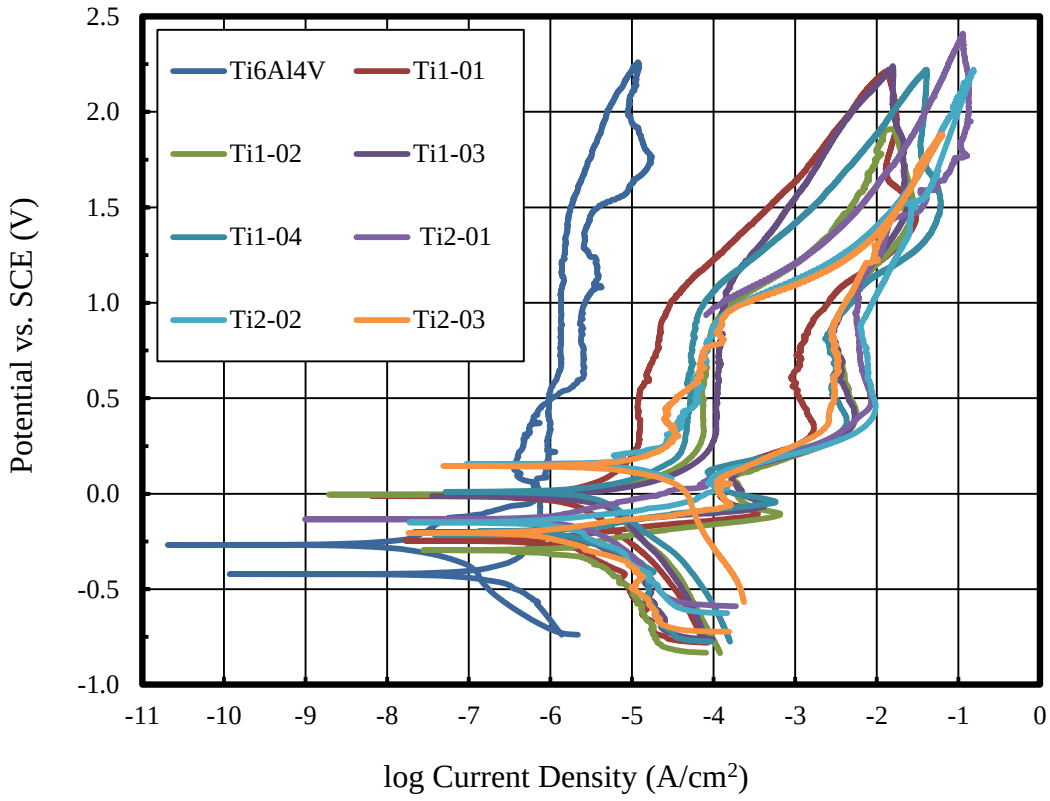

Figure 28. Cyclic potentiodynamic polarization of Ti-MMCs

Tafel Analysis

It appears that the corrosion current of the Ti6Al4V sample is much lower than the Ti-MMCs. To confirm this, Tafel analysis was performed to determine the corrosion current and corrosion rate for the samples. Corrosion current is the current density at which the anodic and cathodic slopes, based on OCP ± 150 mV, intersect. The Tafel curves are presented in Appendix D.

Table 5 shows the anodic and cathodic slopes (β_a and β_c respectively), corrosion current (I_c), OCP (E_o), and corrosion rate (CR) for Ti6Al4V, Ti1 MMCs, 316 stainless steel and AA 5083.

Table 5. Tafel analysis of Ti-MMCs

	β_a (mV)	β_c (mV)	I_o (nA/cm^2)	E_o (V)	CR (MPY)
Ti-6Al-4V	247.9	153.0	24	-0.27	0.01
Ti1-01	55.7	164.0	893	-0.25	0.31
Ti1-02	84.2	201.2	1494	-0.30	0.51
Ti1-03	56.1	146.9	939	-0.20	0.32
Ti1-04	87.7	155.4	1767	-0.22	0.61
Ti2-01	138.3	228.7	1938	-0.13	0.67
Ti2-02	81.5	275.1	1743	-0.15	0.60
Ti2-03	61.5	145.5	778	-0.21	0.27
316 SS	914.7	100.3	221	-0.24	0.10
AA 5083	104.3	71.2	543	-1.08	0.70
Ti Grade 2	181.7	141.8	70	-0.30	0.01

Figure 29 presents relative compariasons between the corrosion rate of Ti6Al4V, Ti1 MMCs, and other materials as determined by Tafel analysis. It is apparent that the Ti MMCs have a greater corrosion rate than Ti6Al4V, Grade 2 Titanium, and 316 SS but possibly equal to or better than some aluminum alloys, specifically AA 5083.

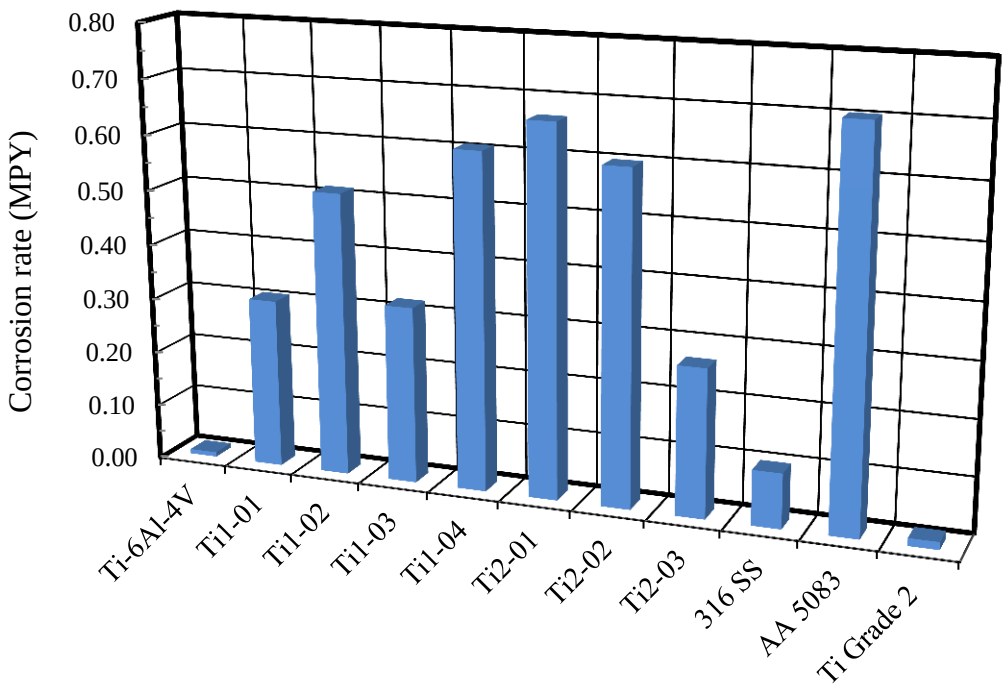

Figure 29. Comparison of corrosion rates in Ti-MMCs, Ti6Al4V and other common alloys

Overall, the reduction in corrosion resistance of the Ti-MMCs is likely a result of inconsistent repassivation of the protective surface oxide which gives titanium its exceptional corrosion resistance. Inconsistent repassivation will lead to holes in the protective oxide layer that will cause accelerated localized corrosion.

This research has demonstrated the effectiveness of creating Ti-MMCs with high hardness which could translate to improved wear performance in structures entirely fabricated by this process. The wear performance in this research was hindered as a result of minimal melting of the substrate material which caused weak bonding between the MMC and the substrate. While the corrosion resistance was reduced in comparison to Ti6Al4V, it was shown that structures could be created with very high hardness and properties that are equal to if not better than other alloys known to possess good corrosion resistance.

CHAPTER IV

CHARACTERIZATION OF ALUMINUM-BASED METAL MATRIX COMPOSITES

Physical Characterization of Al-MMCs

Like the Ti-MMCs in this research, the top surface of the aluminum-based metal matrix composites were visually inspected and subsequently cross-sectioned to examine the micro and macrostructures using optical and scanning electron microscopy. The top surface macrostructure of *Al1*-MMC (7W13AL1) on AA 7075 is presented in Figure 30.

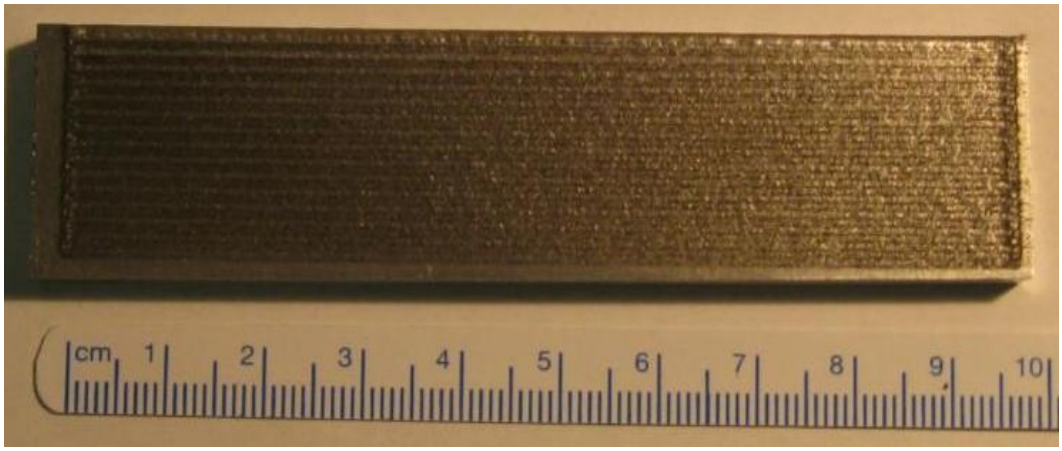

Figure 30. Macrostructure of 7W13Al1 on AA 7075 sbustrate

The depth of the MMCs showed minor sample-to-sample variation. Figure 31 presents the depth of the clad zone for 6W8AL1. Table 6 shows the average and standard deviation of the MMC thickness for *Al1*- and *Al2*-MMCs. No significant trends were found in the clad depth based on laser power and scanning speed.

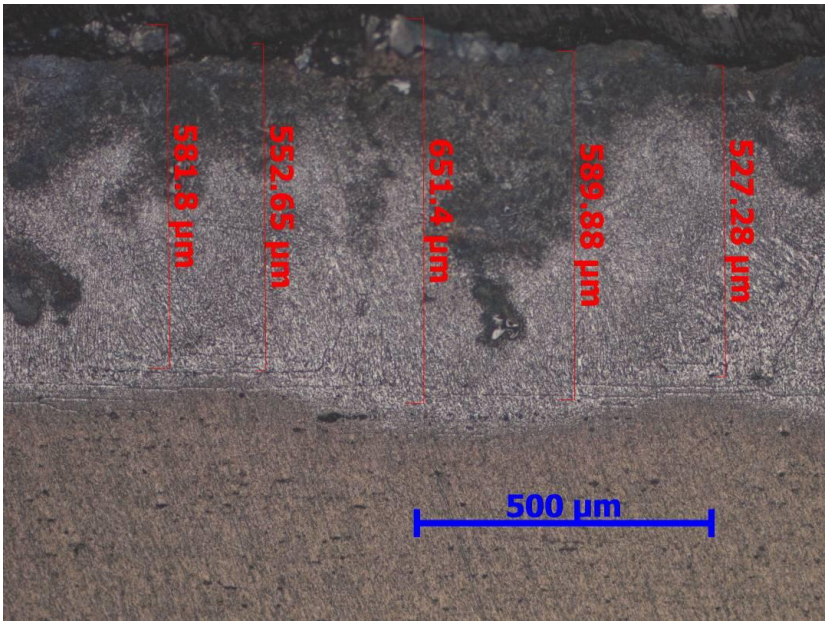

Figure 31. Depth of MMC for 6W8Al1

Table 6. Average thickness of Al-MMCs (A) composition *Al1* and (B) *Al2*

Table 6.1	6W6AL1	6W8AL1	6W10AL1	7W13AL1	7W16AL1
Average Depth (µm)	506	581	550	472	657
Standard Dev. (µm)	58	47	59	62	34

Table 6.2	8W15-3.0AL2	8W15-2.0AL2	7.5W15-3.0AL2	7.5W15-2.0AL2
Average Depth (µm)	469	463	397	402
Standard Dev. (µm)	25	28	40	31

It is evident from the image that the fusion boundary zone is free of voids and cracks that could damage the bond strength of the coating. Figure 32 and Figure 33 present the formation of dendrites in the MMC coating. The growth of dendritic grains formed in the composite is produced a result of rapid solidification of the melt pool during laser treatment. Rapid solidification of aluminum alloys may result in microstructural refinement resulting in a smaller dendrite arm and eutectic spacing in the alloys [13].

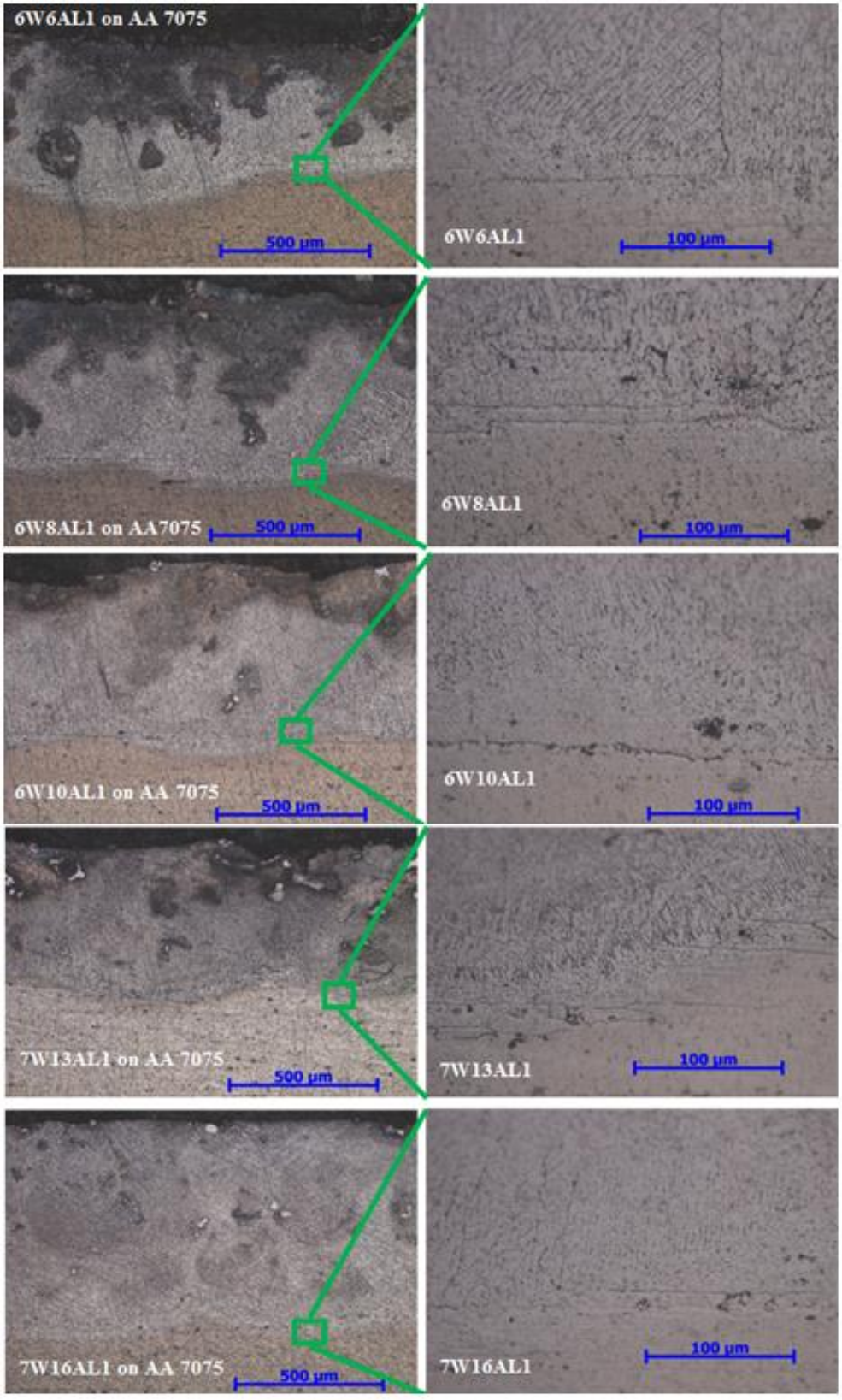

Figure 32. Microstructure of the Al1-MMCs on AA 7075

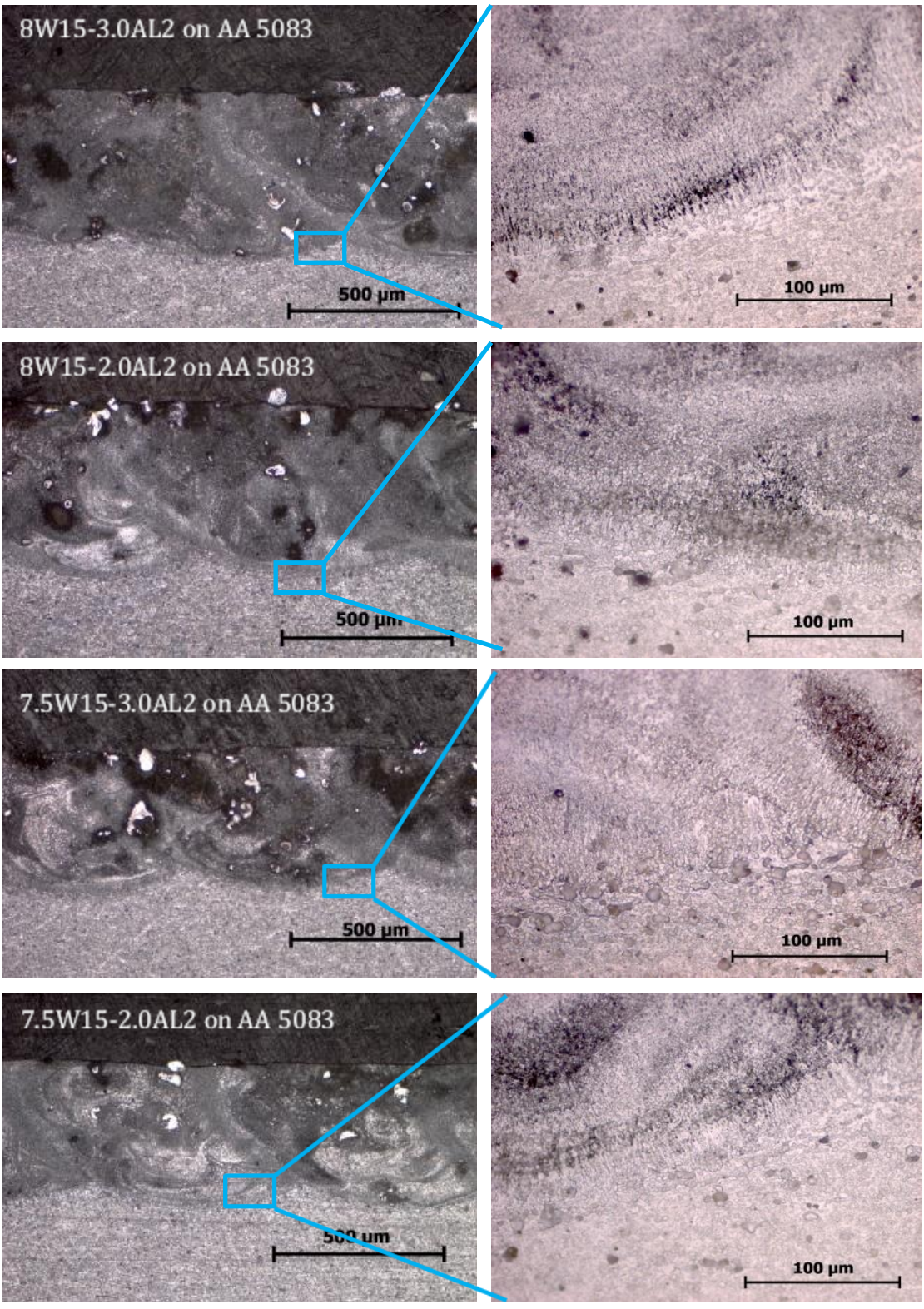

Figure 33. Microstructure of the Al2-MMCs on AA 5083

Scanning electron microscopy of the melt region and heat-affected regions also indicate the formation of fine grains due to high quench rates. As the melt pool solidifies, the grain refinement and growth of the dendritic structure is a result of rapid solidification that rejects solute from the melt pool reducing the dendrite tip radius [1]. This is evident in Figure 34 and Figure 35 which present SEM imagery several of the *Al1*-MMCs and *Al2*-MMCs respectively.

The MMCs appear to be free of coarse constituent precipitates of zinc (AA 7075 substrate) and magnesium (AA 5083 substrate). This is evidence of rapid solidification in the melt pool with small amounts of dilution of the substrates. This indicates the formation of a strong bond between the MMC and the substrate.

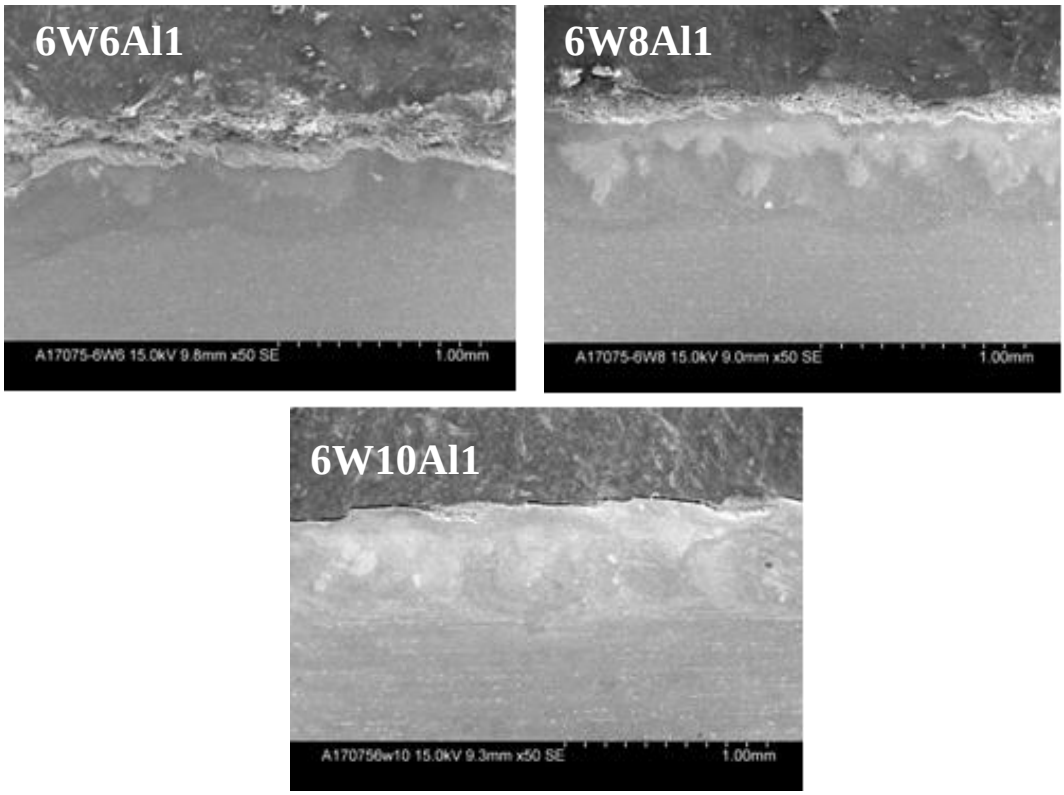

Figure 34. SEM images of Al1-MMCs on AA 7075 substrate

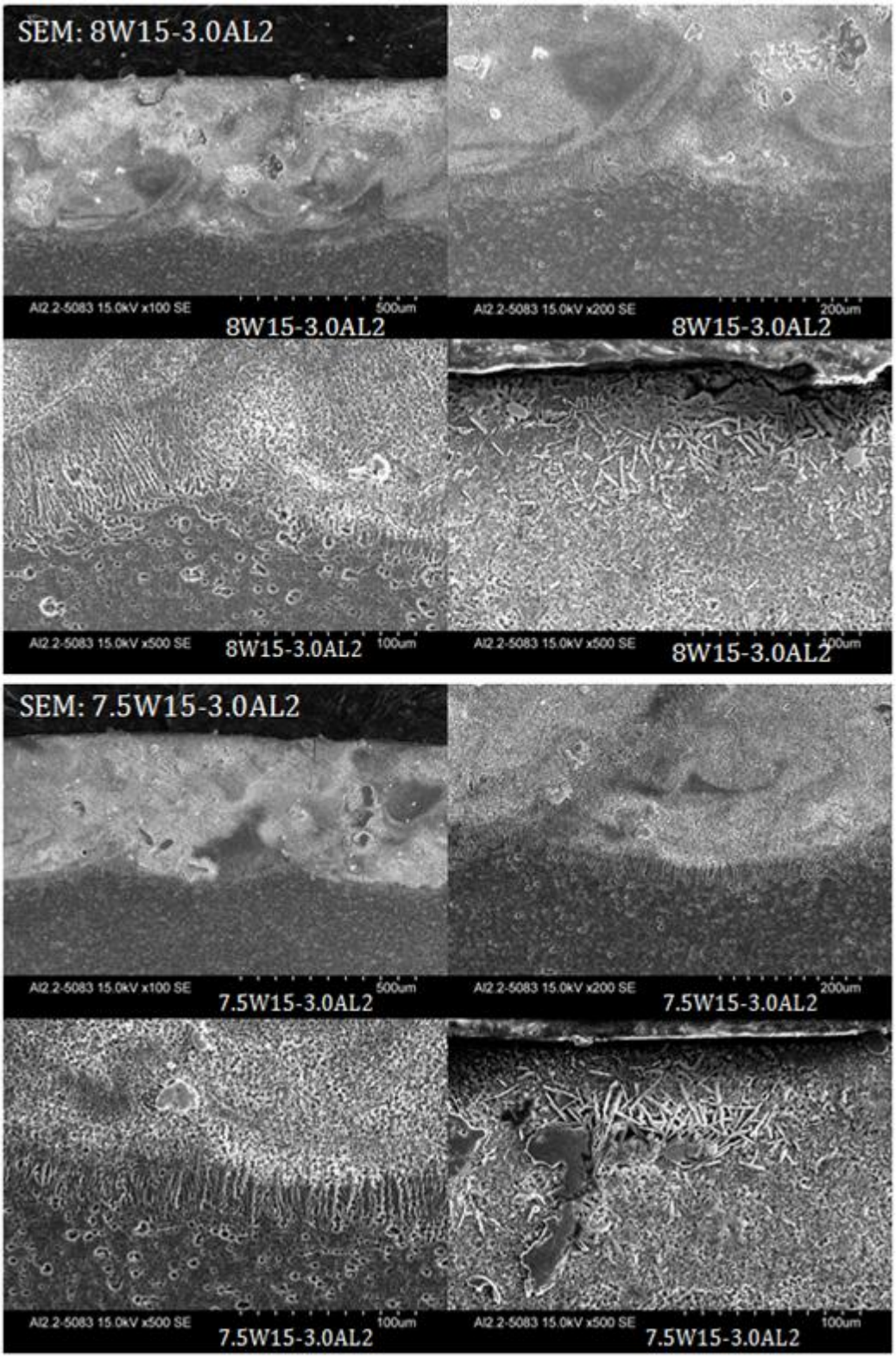

Figure 35. SEM images of Al2-MMCs on AA 5083 substrate

EDS mapping indicates a high level of carbide particles in the MMC. Figure 36 presents EDS compositional mapping for *Al2*-MMCs on AA 5083. In each sample, the fusion boundary zone can be observed between the substrate and the MMC. The red color indicates the presence of carbon and is representative of the phenolic resin used to mount the samples. *Al1*-MMCs were not mapped in this study; however, quantitative compositional analysis was performed using the same detector.

Quantitative analysis of the MMC compositions further indicates the presence of CrC and W-C-Ni superalloy as observed in Table 7. MMCs with composition *Al1* (50 wt% Al powder, 25 wt% CrC and 25 wt% W-C-Ni superalloy) indicated an aluminum matrix with levels ranging from 55% to 83%. Composites from composition *Al2* (75 wt% Al powder, 12.5 wt% CrC and and 25 wt% W-C-Ni superalloy) indicated higher levels of aluminum content, as expected, ranging from 73 wt% to 87 wt%. This provides evidence to confirm the presence of fewer carbide particles in *Ti2*-MMCs.

The fluctuations in wt% could result from minor changes in the laser processing parameters or minor differences in elemental identification as a result of overlapping peaks in energy spectra as frequently common to EDS analysis.

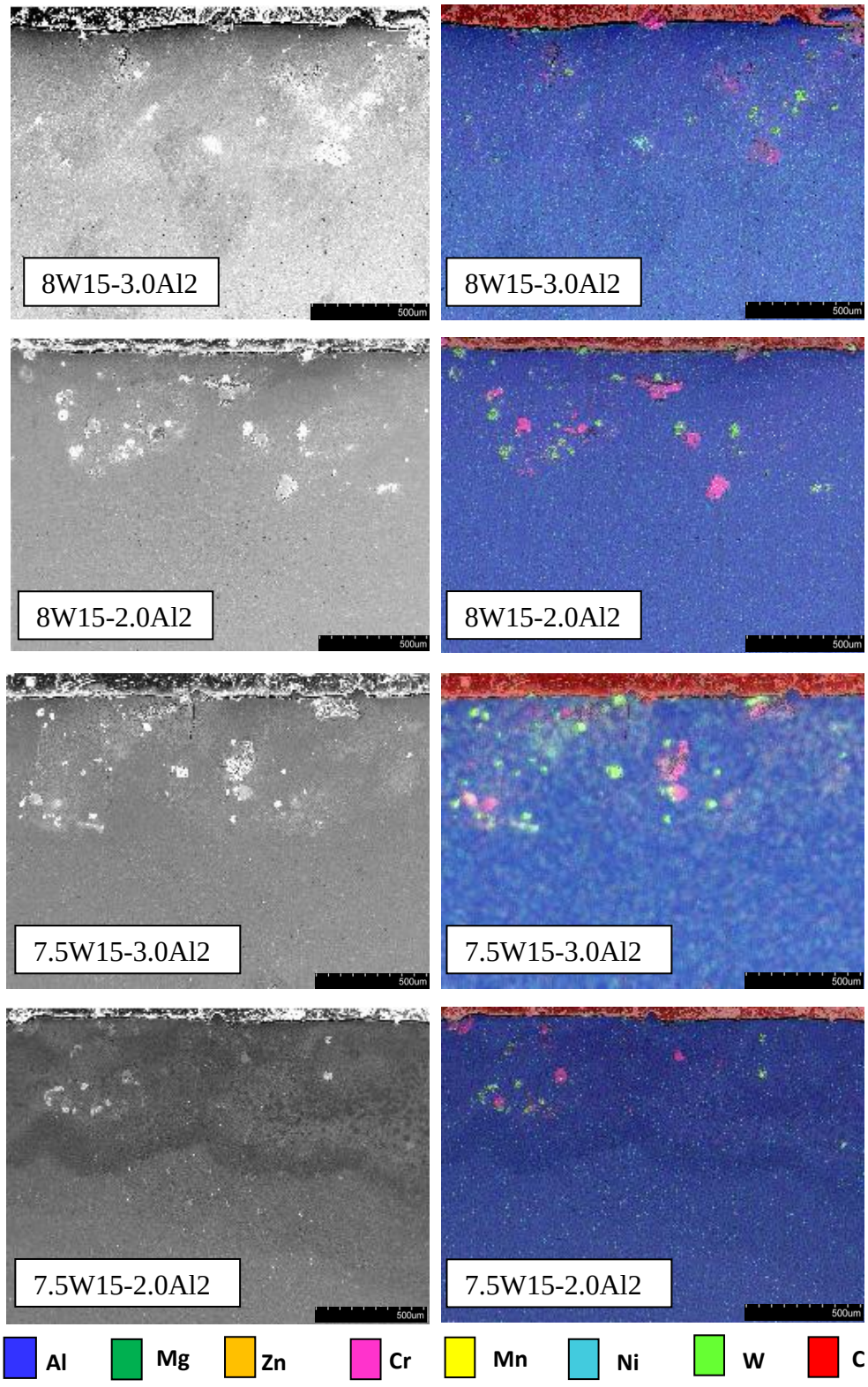

Figure 36. EDS composition mapping for Al2-MMCs

Table 7. Ti1 and Ti2-MMC EDS composition analysis

Elemental Composition (wt%)							
Sample	Al (wt%)	Zn (wt%)	Cr (wt%)	Ni (wt%)	W (wt%)	Mg (wt%)	Cu (wt%)
6W6Al1	61.0	0.8	12.3	3.5	9.1	0.8	0.9
6W8Al1	55.5	0.3	11.4	3.6	7.4	0.5	0.8
6W10Al1	63.1	0.5	7.5	2.3	6.1	1.3	1.1
7W13Al1	70.8	1.6	2.6	0.5	1.6	2.0	0.8
7W16Al1	83.9	1.6	2.6	0.7	3.5	2.6	0.8

EDS Elemental Composition (wt%)								
Sample	Al (wt%)	Mg (wt%)	Cr (wt%)	Mn (wt%)	Ni (wt%)	Zn (wt%)	W (wt%)	C (wt%)
8W15-3.0Al2	87.9	3.6	1.7	0.5	0.6	0.1	1.6	4.2
8W15-2.0Al2	85.8	3.8	2.1	0.6	0.6	0.0	1.9	5.1
7.5W15-3.0Al2	83.8	3.4	2.5	0.6	0.9	0.1	2.6	6.0
7.5W15-2.0Al2	73.5	3.3	1.1	0.5	0.4	0.1	1.0	20.1
AA 5083	90.4	4.9	0.1	0.5	0.1	0.1	0.7	3.3

Mechanical Evaluation of Al-MMCs

Nanoindentation

Table 8 presents reduced modulus and nanohardness for Al1-MMCs. The data collected behaved in a linear manner from sample to sample which is predicted by the nature of nanoindentation as outlined by Oliver and Pharr [79].

The nanohardness was increased in the 700W1600 sample while there is no significant difference in hardness for the other specimens. A maximum hardness and reduced modulus of 2.47 GPa and 87.43 GPa, respectively, were recorded for the composite in sample 700W1600. Hardness and reduced modulus of the AA 7075 substrate were 1.45 GPa and 70.63 GPa, respectively; this yields a 78% increase in hardness. Samples 600W600, 600W800, 600W1000, and 700W1300 indicated no improvement in hardness or modulus. Sample 8W15-3.0Al2 also indicates an

approximately 48% increase in hardness over AA 5083. This, however, is not representative of a homogeneous MMC. This is primarily indicative of the matrix material and not representative of carbide reinforcing particles dispersed throughout the melt region. Table 8 shows the average contact depth, reduced modulus, and nanohardness for Al1- and Al2-MMCs on AA 7075 and AA 5083 respectively.

Table 8. Al1- and Al2-MMC nanoindentation analysis

Sample		Contact Depth (nm)	Reduced Modulus (GPa)	Hardness (GPa)
AA 7075	Average	384	71	1.5
	Standard Deviation	40	8	0.3
600W600	Average	392	77	1.4
	Standard Deviation	37	8	0.3
600W800	Average	365	84	1.6
	Standard Deviation	29	8	0.3
600W1000	Average	435	77	1.7
	Standard Deviation	38	19	0.8
700W1300	Average	404	75	1.3
	Standard Deviation	24	5	0.2
700W1600	Average	300	87	2.5
	Standard Deviation	49	12	0.9
8W15-3.0Al2	Average	101	102	3.1
	Standard Deviation	22	20	1.2
8W15-2.0Al2	Average	107	95	2.6
	Standard Deviation	13	22	0.9
7.5W15-3.0Al2	Average	101	91	2.8
	Standard Deviation	8	7	0.4
7.5W15-2.0Al2	Average	108	101	2.6
	Standard Deviation	17	20	0.7
AA 5083	Average	120	83	2.1
	Standard Deviation	13	10	0.4

In DMLD, the carbide particles are scattered throughout the clad region as observed in particle reinforced composites. The values measured in four of the five *Al1* DMLD specimens appear to be representative of the Al matrix. The fifth 700W1600 shows evidence of carbide particles in the melt region. The same is observed in the *Al2* composites. Only the sample 8W15Al2-3.0 indicates significant change over the substrate, 8W15Al2-3.0.

Regions with greater amounts of carbide particles will have higher hardness and reduced modulus values than regions where only Al matrix exists. Thus, nanoindentation appears to be a less desirable choice for determining the hardness throughout the melt region as an entity because of its small scan area. It is, however, an excellent method for determining the hardness of individual carbide particles. However; motion control allowing this is not available on the Hysitron-TI950 Nanomechanical Tester.

Microhardness

Figure 37 presents microhardness data collected for MMCs with composition *Al2*. Microindentations were made with an indentation load of 100g and a hold time of 15s. The indentations were made at incremental distances from the surface in order to determine the hardness profile of the MMC; however, Figure 37 only presents indentations made in the MMC. See Appendix C for the hardness through the profile.

The data indicates the presence of carbide particles throughout the clad layer. Also, the larger observed variance in the clad region is attributed to the discontinuous dispersion of carbide particles as a result of molten metal flow due to the intense thermal gradients produced in the melt pool in the laser cladding process.

The samples with composition *Al2* contain an increased proportion of aluminum metal matrix. These samples were tested using a Vickers microhardness tester. Indentations were made in a systematic manner with an average of five indentations made at increasing distances from the surface. The microhardness results are presented as a function of distance from the surface of the composite in Figure 37. The varying magnitude of hardness is due, again, to the discontinuous dispersion of hard carbide particles in the clad region. The average microhardness in the Al-MMCs was between 47% and 79% higher than AA 5083. The entire melt pool containing carbide particles exhibits variations in hardness due to the mixing of the melt as a result of rapid mixing from intense thermal gradients created during the process.

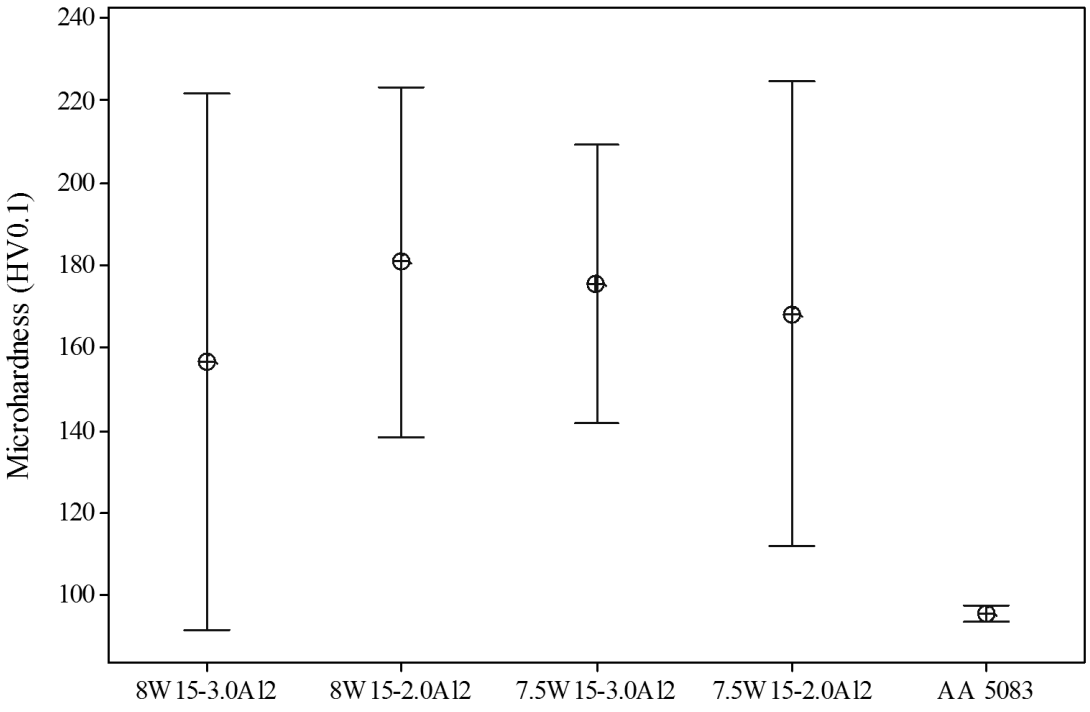

Figure 37. Microhardness (Vickers) of Al2-MMCs and AA 5083

Taber Wear Index

Taber rotary platform abrasion testing was performed using CS-10 Calibrase ® and refacing discs while refacing after 1000 cycles. Mass loss was measured after 2000 cycles. A 1000 g load was applied to the abrasive wheels causing rub-wear action, or sliding rotation, on the surface of the specimen. A vacuum system removed debris during testing. Figure 38 presents the Taber Wear Index (TWI) as calculated by Equation 2.7 for Al2-MMCs and AA 5083 as adapted from the unpublished work of Dr. Samar Kalita and Joshua Johnson of the Advanced Engineered Materials Center.

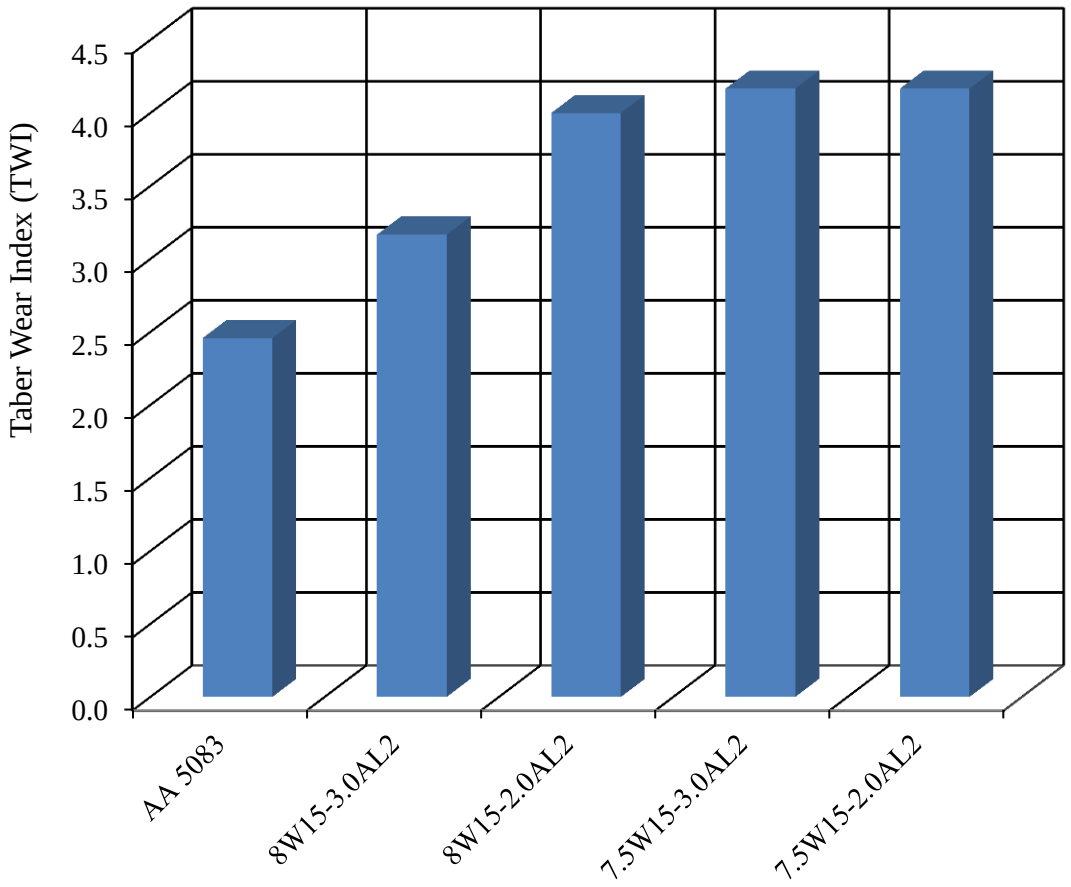

Figure 38. Taber Wear Index (TWI) for AA 5083 and Al2-MMCs

After 2000 cycles, the Al2-MMCs indicated a greater total mass loss indicating a higher TWI. 8W15-3.0AL2 had the smallest change in TWI with a 29% increase over AA 5083. 7.5W15-2.0AL2 indicated a 69% increase in TWI. The increase in TWI, like the Ti-MMCs is likely due to insufficient bonding at the interface of the matrix and reinforcing particles.

Corrosion resistance of Al-MMCs

Open Circuit Potential

Figure 39 presents OCP vs. Immersion Time for *Al1*- and *Al2*- MMCs. The AA 7075 samples treated with powder composition *Al1* indicated a similar OCP to that of untreated AA 7075. The open circuit potential (E_o) remained relatively constant during the 35 hour immersion for most of the samples. However, 6W8AL1, 6W10AL1 and 7W13AL1 took a longer time for the potential to reach steady state. This indicates that the sample requires more time to achieve its protective surface film from a decrease in the anodic passive current density. Untreated AA 7075 exhibited an average E_o of -790 mV. 7W16AL1 presented the most positive open circuit potential of all Al-MMC specimens while 7W13AL1 displayed the most negative. However, in comparison to other aluminium alloys, this difference is quite small. For example, AA 5083 and AA 5456 indicated a more highly negative potential of -843 mV and -892 mV respectively.

Formulation *Al2* was deposited onto an AA 5083 substrate. It is evident from the data that the OCP of the MMCs of this composition share a very similar OCP, fluctuations (<25 mV), to the parent AA 5083. AA 5083, as previously mentioned, showed a potential of approximately -740 mV. MMCs with composition *Al2* showed a similar potentials ranging from -737 mV for 8W15-3.0AL2 and -752 mV for 7.5W15-2.0.

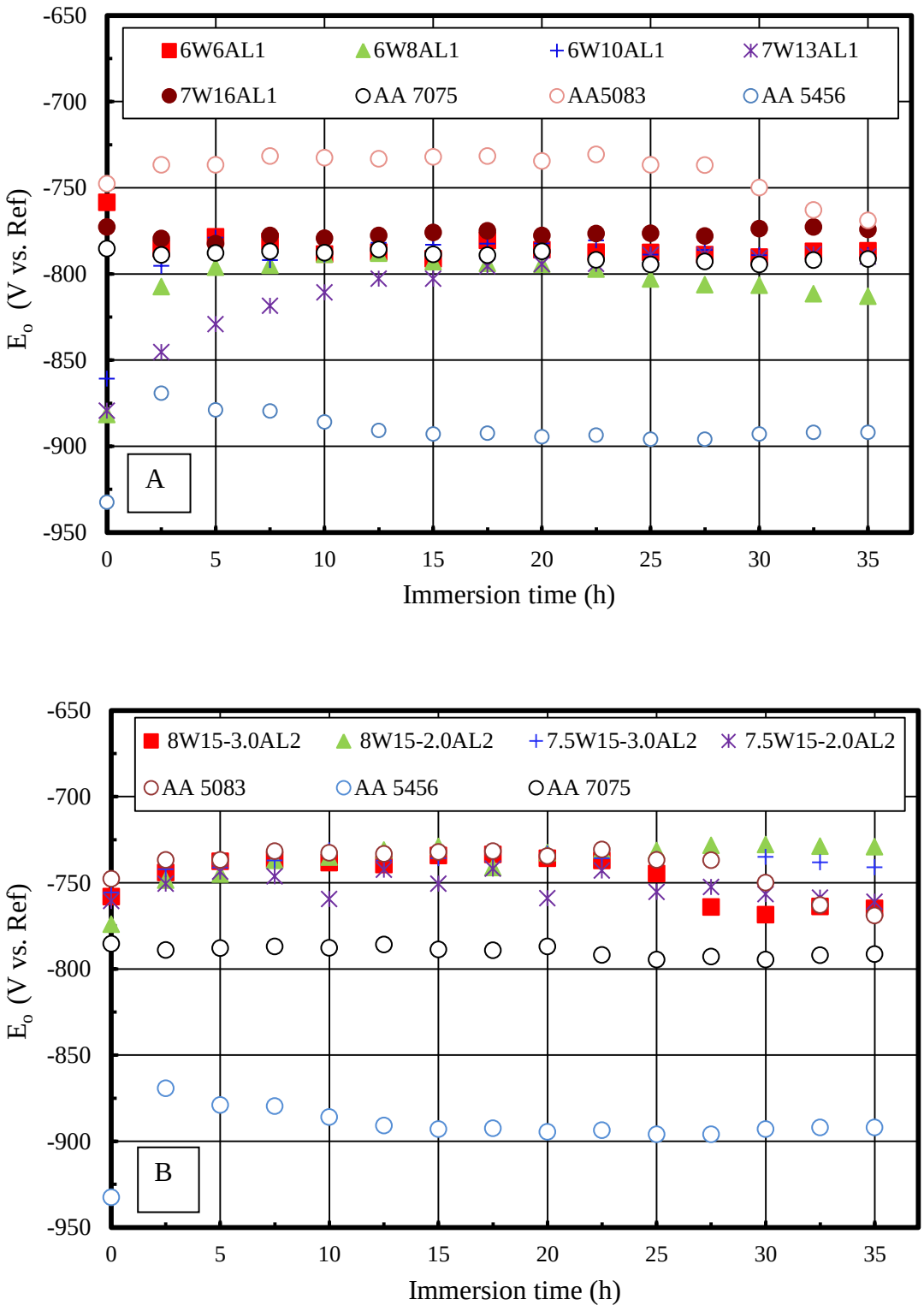

Figure 39. Open Circuit Potential for Al1 (A) and Al2 (B) MMCs on AA 7075 and AA 5083

Polarization Resistance

Polarization resistance, R_p, of a material is defined as the slope of the potential (voltage) vs. current density curve at OCP. The rate of corrosion is inversely proportional to polarization resistance. Figure 40 presents the time history of polarization resistance on a log scale for all four specimens.

The initial R_p for AA 7075 was 1.35 kΩ·cm^2. Over the entirety of the immersion the R_p reached a maximum of 19.0 kΩ·cm^2. The increase in R_p may indicate the formation of a more passive surface over the duration of the experiment. Samples with composition *Al1*-MMC to a AA 7075 substrate showed a similar increase in R_p. However, these samples indicated, in general, a reduced R_p throughout the entire experiment. Sample 7W13AL1 showed the lowest polarization resistance. At time 0s, 7W13AL1 exhibited a resistance of 0.159 kΩ·cm^2 and steadily increased to a maximum of 3.56 kΩ·cm^2. The best performing sample, 6W10AL1, had an initial R_p of 0.277 kΩ·cm^2 and increased to a maximum of 5.54 kΩ·cm^2.

R_p for AA 5083 and AA 5456 are also provided in Figure 40 to qualify the results from the *Al1*-MMCs. These samples remain relatively constant for the duration of the experiment with averages of 50.3 kΩ·cm^2 and 34.3 kΩ·cm^2 respectively. This indicates that the *Al1*-MMCs behave more similar to the AA 7075 alloy on which they are clad. This may be evidence of mixing with the parent alloy and that the clad composition *Al1* did not improve the corrosion resistance of AA 70075.

Composition *Al2* was deposited onto substrates of AA 5083. However, the behaviors of the samples show no improvement over the AA 7075 alloy. The composition *Al2*, on AA 5083, like *Al1* on AA 7075 showed increasing values over the duration of the experiment. Sample 8W15-3.0AL2 indicated resistances ranging from

0.612 - 7.44 kΩ·cm^2. While there are slight differences between *Al2* samples, it appears that the difference in R_p as a result of processing parameters has a minimal effect on the overall performance of the sample. It appears that composition of the clad may have a more significant effect on the corrosion performance of the DMLD structures.

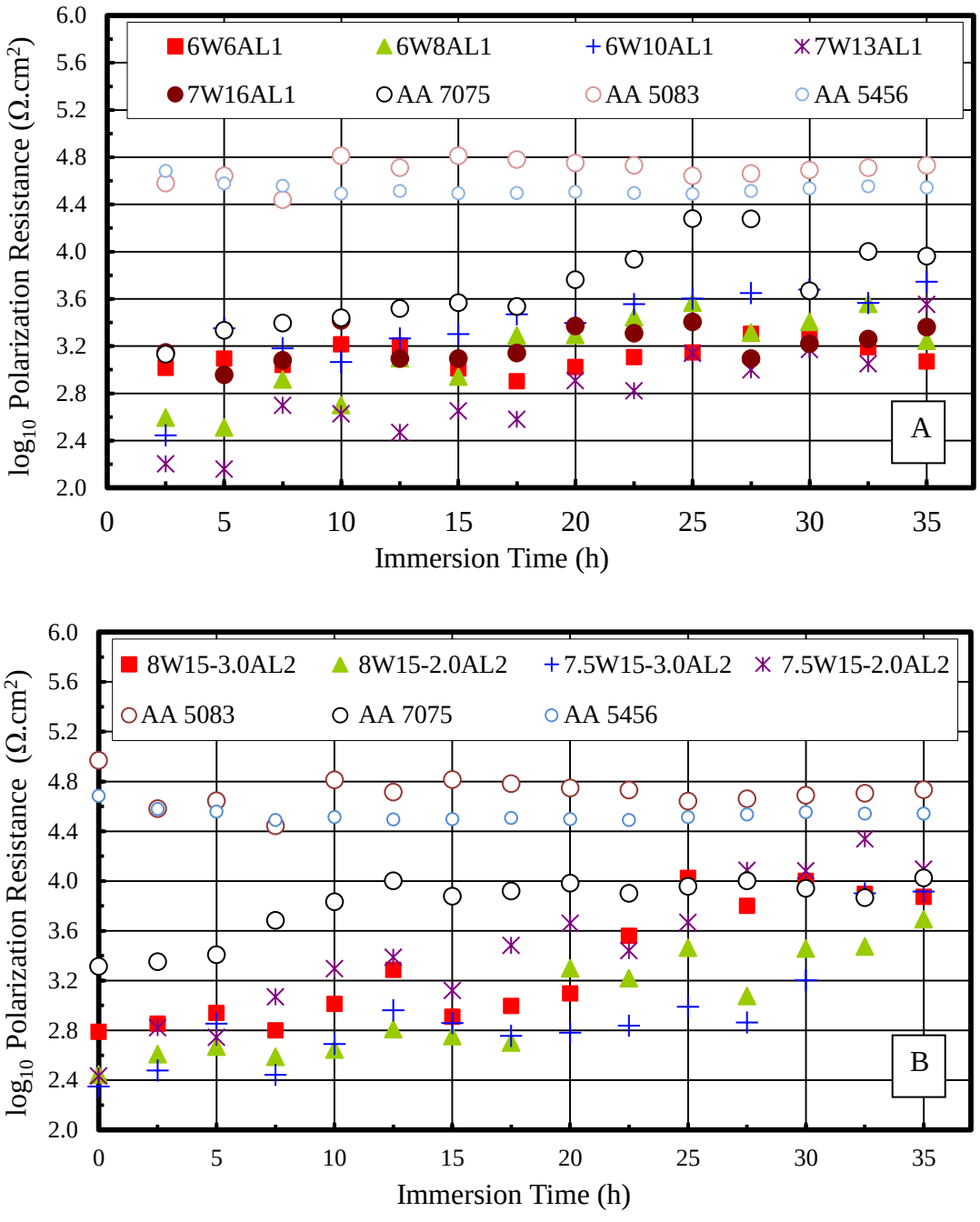

Figure 40. R_p for *Al1* (A) and *Al2* (B) MMCs on AA 7075 and AA 5083 respectively.

Potentiodynamic Polarization

Figure 41 presents the potentiodynamic polarization curves of *Al1* and *Al2* MMCs immersed in 0.5 M NaCl solution. The kinetic behavior of the samples as they arescanned with with constant potential was similar for AL-MMCs, AA 7075 and AA 5083 alike.

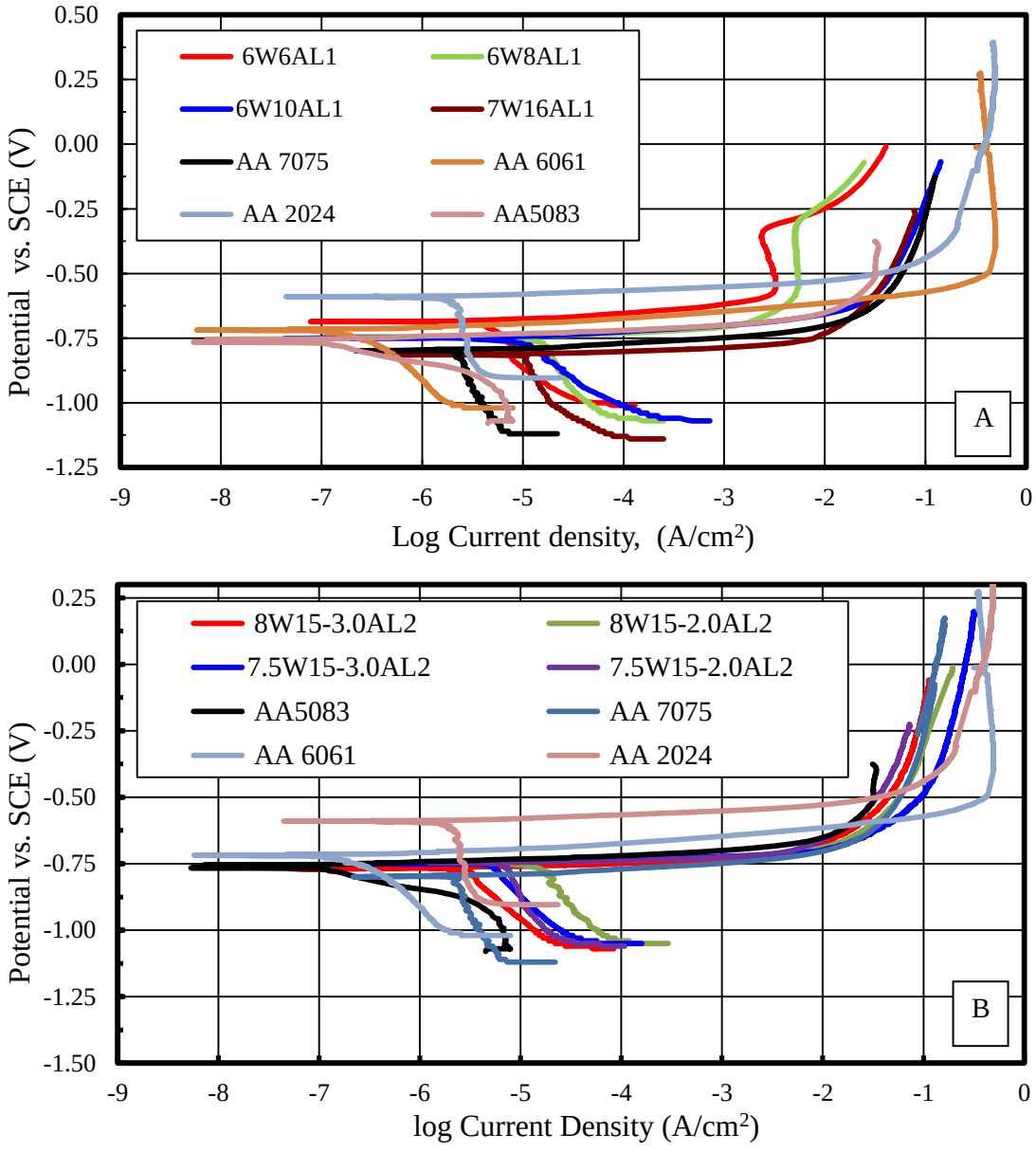

Figure 41. Potentiodynamic Polarization for Al1 (A) and Al2 (B) MMCs on AA 7075 and AA 5083.

The corrosion potential is -0.7 ± 0.05 V for all eight Al-MMC samples as well as for AA 5083 and AA 7075. AA 2024 is also shown for comparison in Figure 5.11. Unfortunately, the difference in anodic and cathodic slopes make quantatative Tafel analysis an inappropriate choice of characterization. However, what one may deduce from the curves is an observable positive shift (to the right) in current density where the approximate intersection of the anodic and cathodic slopes intersect. This further confirms the results obtained by polarization resistance that the Al-MMCs show less corrosion resistance than their AA 7075 and AA 5083 substrates. This is likely due to the compositional changes observed in the composite as confirmed by EDS tracing. The introduction of WC particles into the surface of the MMC may cause inconsistent repassivation of the surface causing accelerated corrosion. These observations are consistent with what has been seen for the Ti-MMCs as presented in Chapter III.

However, as with the titanium-based composites, there still exist advantages to the composites fabricated in the present study. Increased hardness was seen in the MMC structures which suggests the possibility of creating 3D structures with increased hardness or wear resistance assuming sufficient bonding is observed between succsesive layers.

Again, the corrosion resistance is lower than alloys like AA 2024 and AA 5083. However, it appears that the performance is only slightly worse than AA 7075. Like the Ti-MMCs it appears that there is a reduction in corrosion performance at the expense of hardness.

CHAPTER V

CONCLUSIONS

A systematic study of the corrosion and wear resistance of titanium- and aluminum-based MMCs fabricated by DMLD was undertaken to determine the effect of adding carbide reinforcement particles to the MMC formulation.

1.) DMLD was successfully employed to create Ti- and Al-MMCs on the surface of various substrate materials
2.) Ti-MMCs indicated titanium matrices ranging from 29 wt% to 58 wt% for Ti1 formulation consisting of 50 wt% Ti powder, 25 wt% W-C-Ni, and 25 wt% CrC powder. The Ti2 formulation (50 wt% Ti powder, 25 wt% W-C-Ni, and 25 wt% CrC) powder indicated higher slightly titanium matrix percentage but still ranged from 35 wt% to 56 wt%.
3.) Minimal dilution of the substrate material was seen in the Ti-MMCs as observed by EDS. This caused a weak bond between the MMC and substrate.
4.) The average microhardness of the Ti-MMC was between 207% and 350% higher than Ti6Al4V. Al-MMCs exhibited an increase of between 47% and 79%.
5.) The Ti-MMCs demonstrated a TWI that was significantly greater, meaning that the resistance to wear was not improved in the composites. The difference was quite significant after 2000 cycles, 219% and 350% greater, respectively.

At 4000, 6000, and 8000 cycles the TWI of the Ti-MMCs was 50% greater. In the Al-MMCs, as performed by S.K. Kalita and J. Johnson, again, no improvement in wear resistance was observed.

6.) OCP indicates that neither the Ti- nor the Al-MMCs develop a surface film that is as protective or noble as the substrate on which they were fabricated. Ti-MMCs exhibited more negative potentials by between 68 and 122 mV. Similarly, the Al-MMCs showed differences of between 53 and 103 mV.

7.) In the Ti-MMCs of both *Ti1* and *Ti2* compositions, R_p decreased from 5.85 $M\Omega \cdot cm^2$ to between 10.0 and 17.9 $k\Omega \cdot cm^2$. This indicates an increase in the passive current density of the surface which reflects a less protective surface film. The Al-MMCs also exhibited a decrease in $R_{p,}$ indicating no improvement in corrosion resistance.

8.) Ti-MMCs exhibited no pitting corrosion during cyclic potentiodynamic polarization. However, the corrosion current was increased as a result of inconsistent repassivation of the protective surface oxide as supported by OCP and Rp results. This indicates a higher corrosion rate in comparison to Ti6Al4V. However, the corrosion performance of the Ti-MMCs still exhibits better corrosion resistance than several 5xxx series aluminum and 316 stainless steel alloys as determined by Tafel analysis. While quantitative Tafel analysis was not performed on the Al-MMCs, it can be qualitatively observed that the corrosion performance is also reduced in comparison to the parent AA 7075 and AA 5083 alloys.

The results presented in this study, while showing no improvement in corrosion resistance over Ti6Al4V in Ti-MMCs, show that composites can be fabricated by DMLD with increased hardness while maintain corrosion performance better than 5xxx and 316 stainless steel.

Future Work/Recommendations

Results suggest the possibility of creating 3-D structures with increased hardness or wear resistance assuming sufficient bonding is observed between successive layers. However, this research was limited to one layer DMLD MMC coatings. The results cannot be extrapolated to structures fabricated with multiple layers. Thus, further tests should be done with multiple layers. In doing so, sufficient MMC bonding from layer-to-layer should be confirmed before any other quantitative analysis. Multi-layer tests will be crucial in determining the commercialization potential of DMLD as a wear or corrosion resistant method for aerospace and marine applications.

APPENDICES

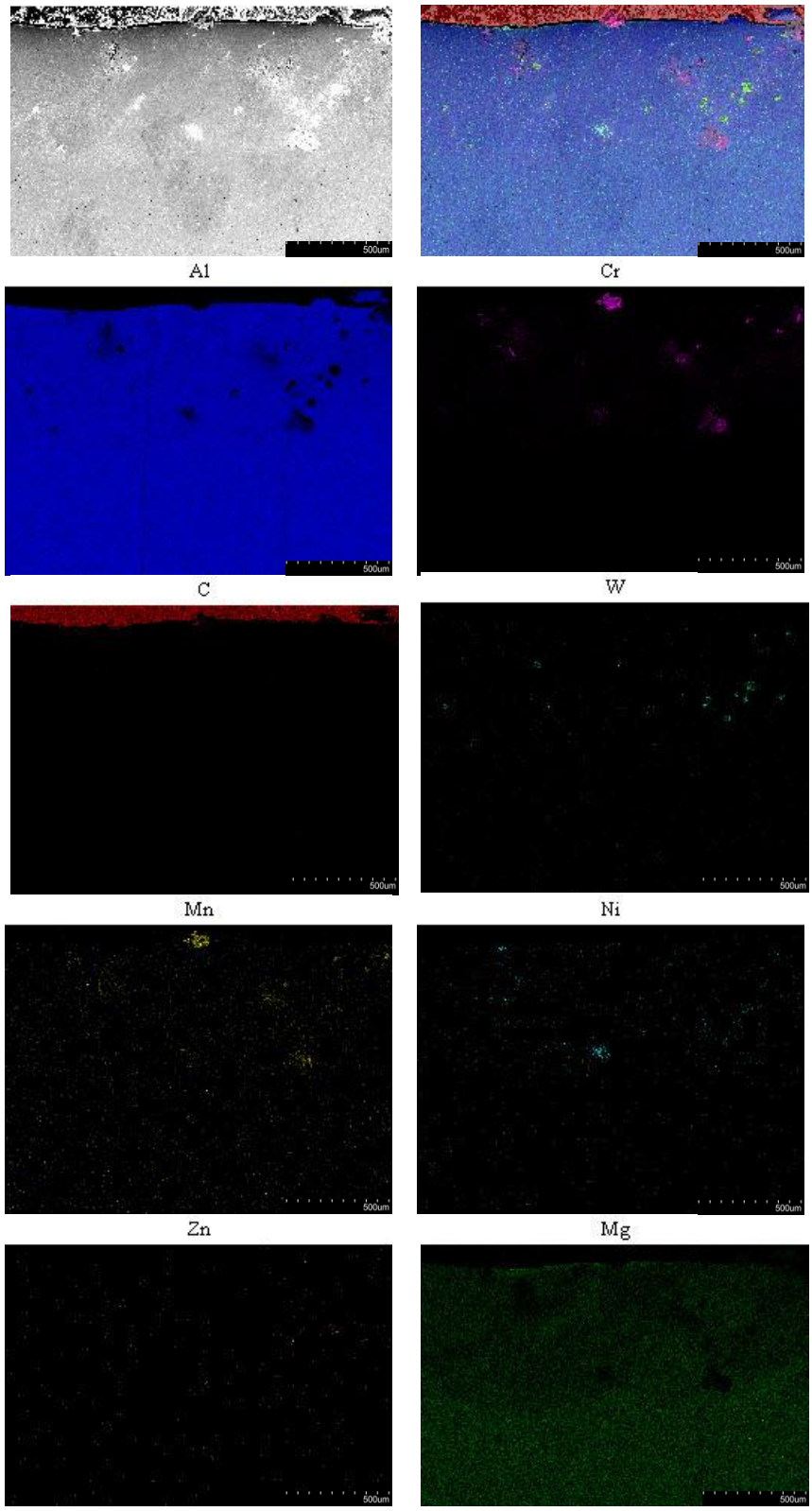

Figure 42. EDS element maps for specimen 8W15-3.0AL2

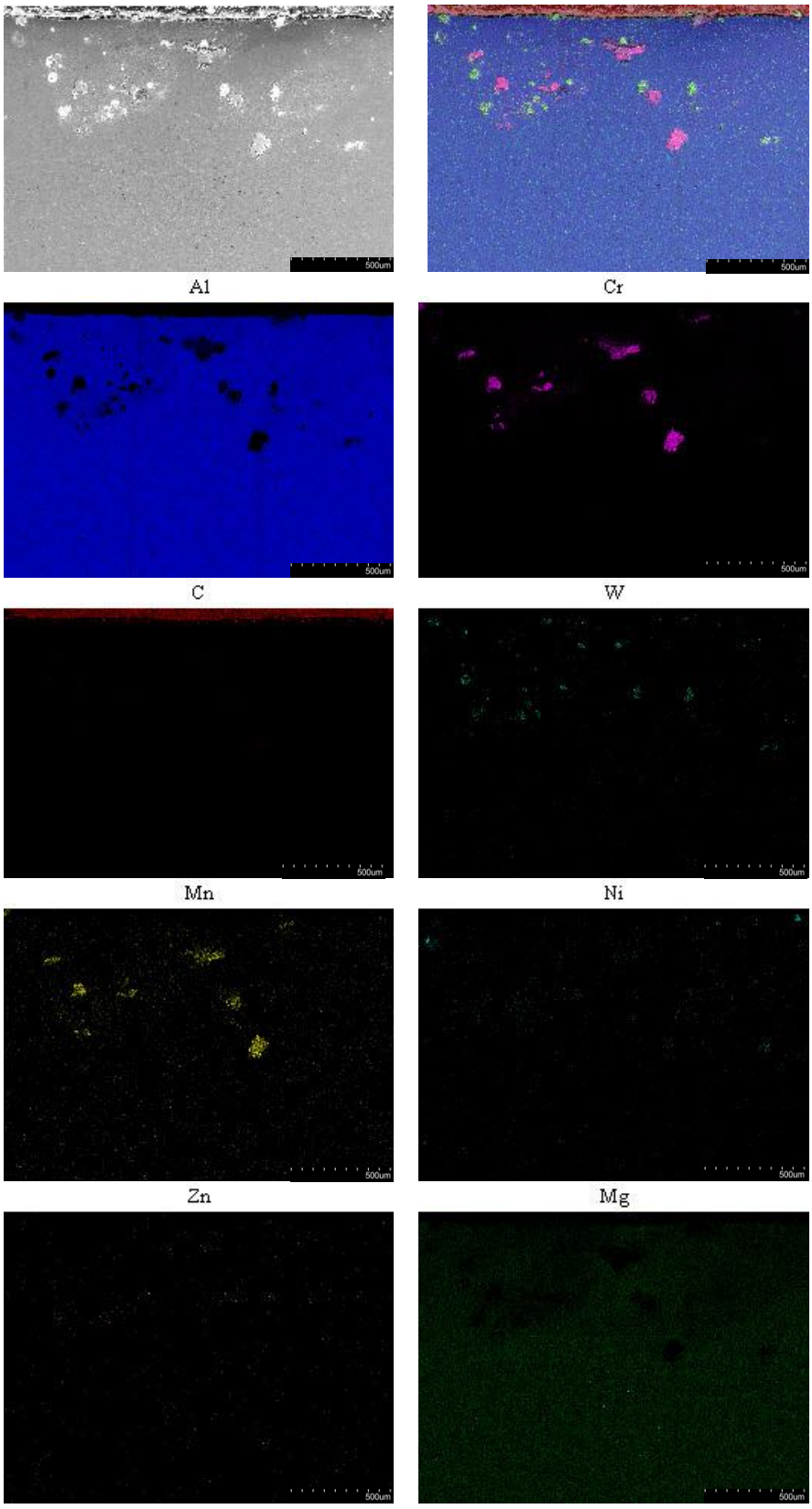

Figure 43. EDS element maps for specimen 8W15-2.0AL2

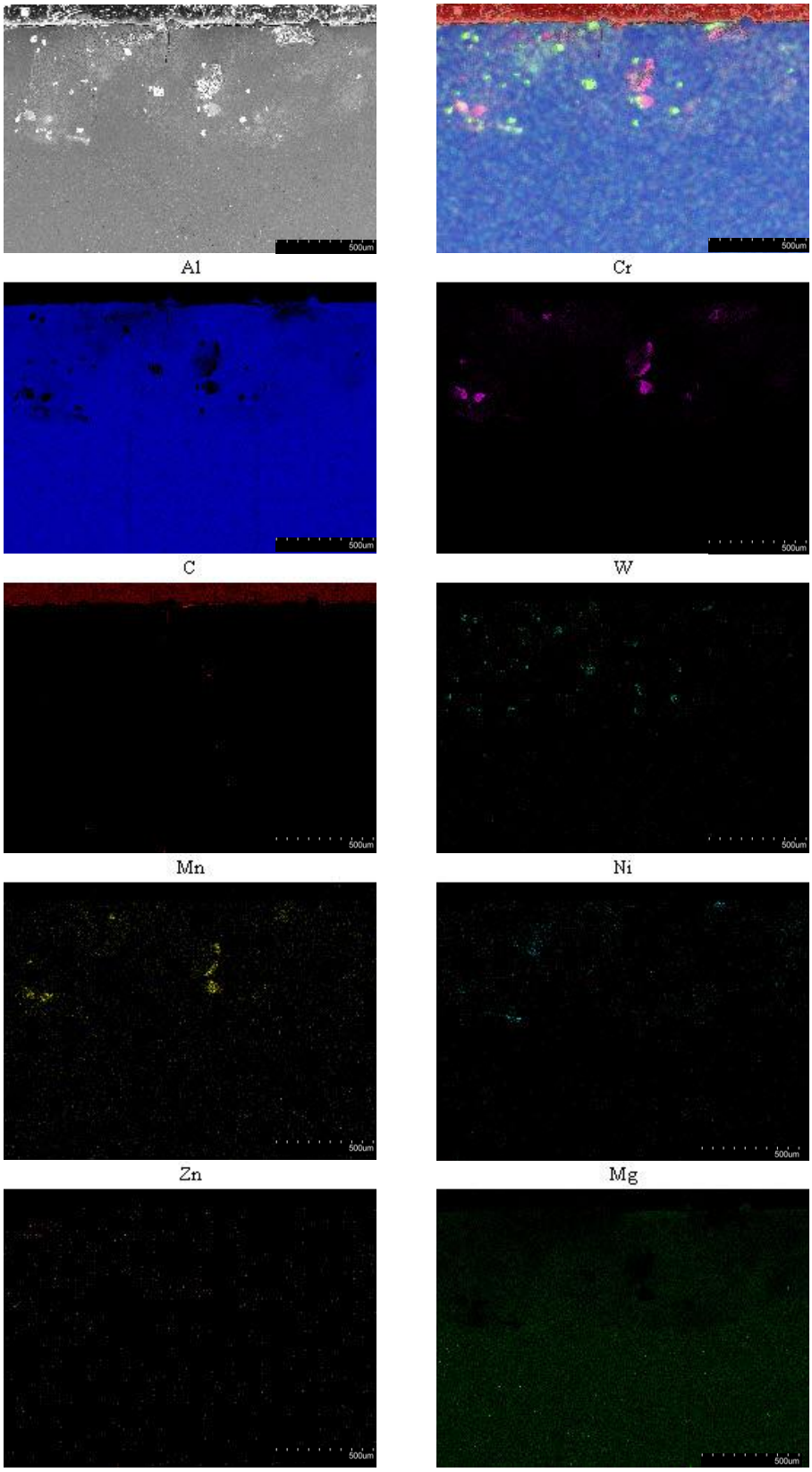

Figure 44. EDS element maps for specimen 7.5W15-3.0AL2

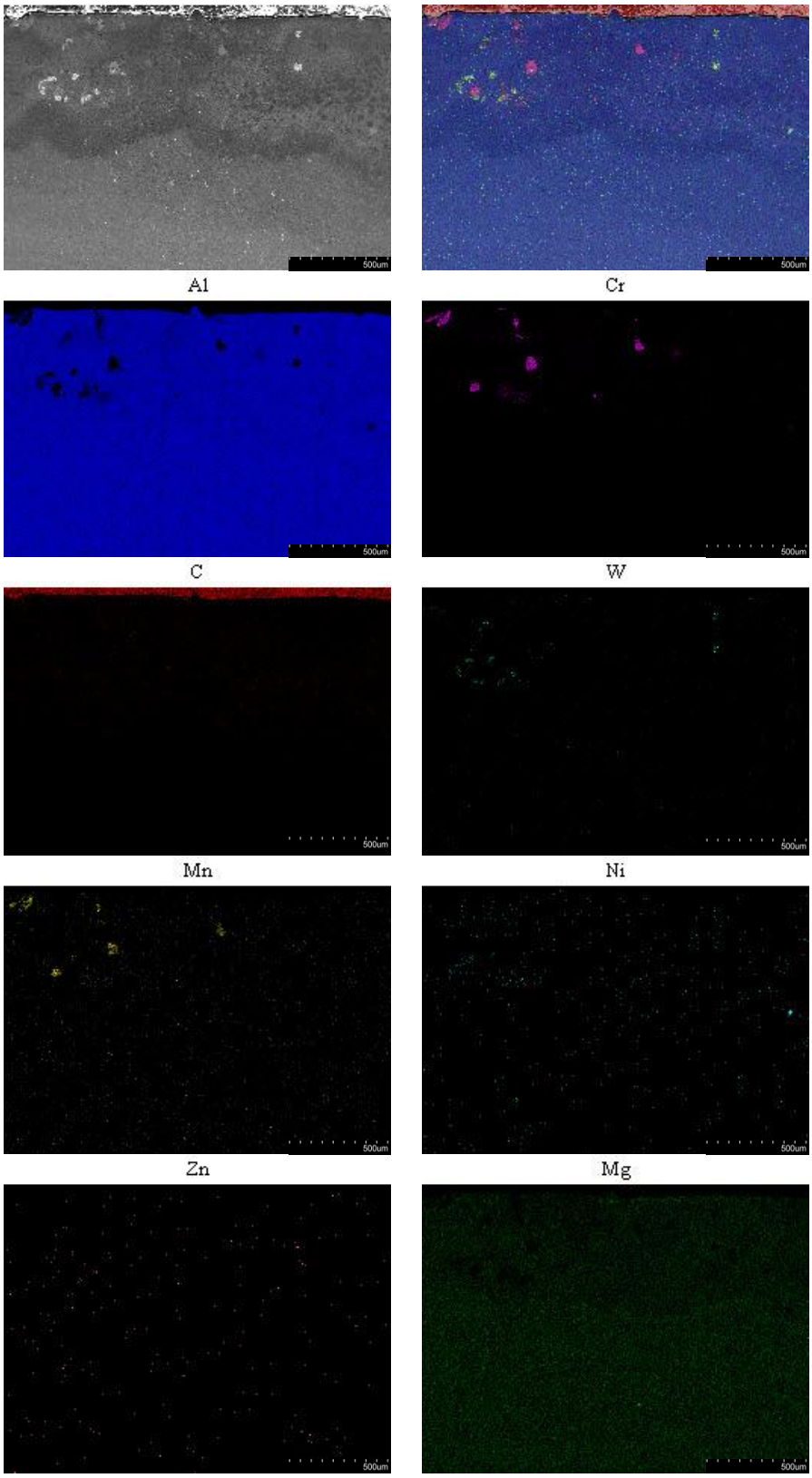

Figure 45. EDS element maps for specimen 7.5W15-2.0AL2

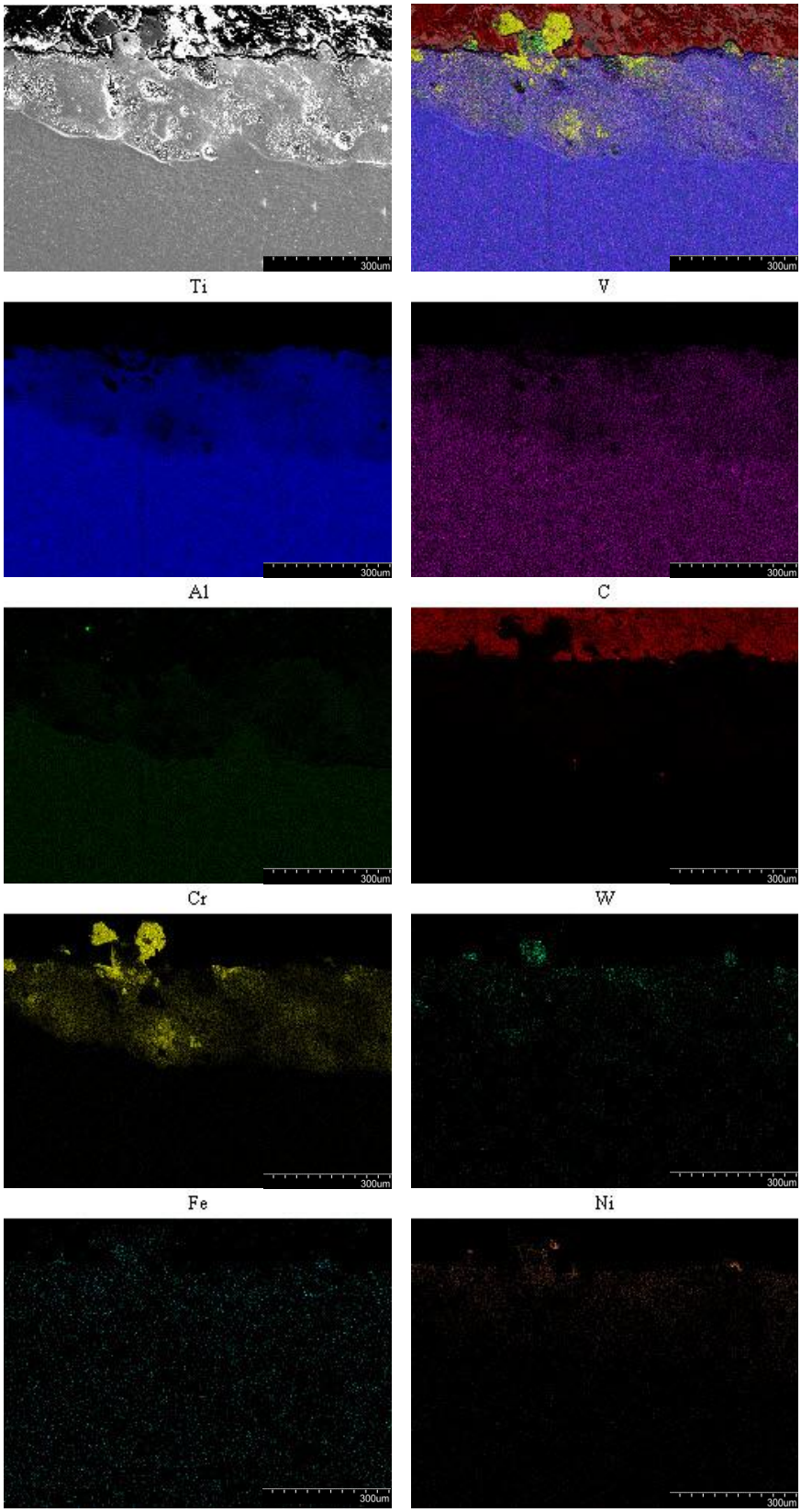

Figure 46. EDS element maps for specimen Ti1-01

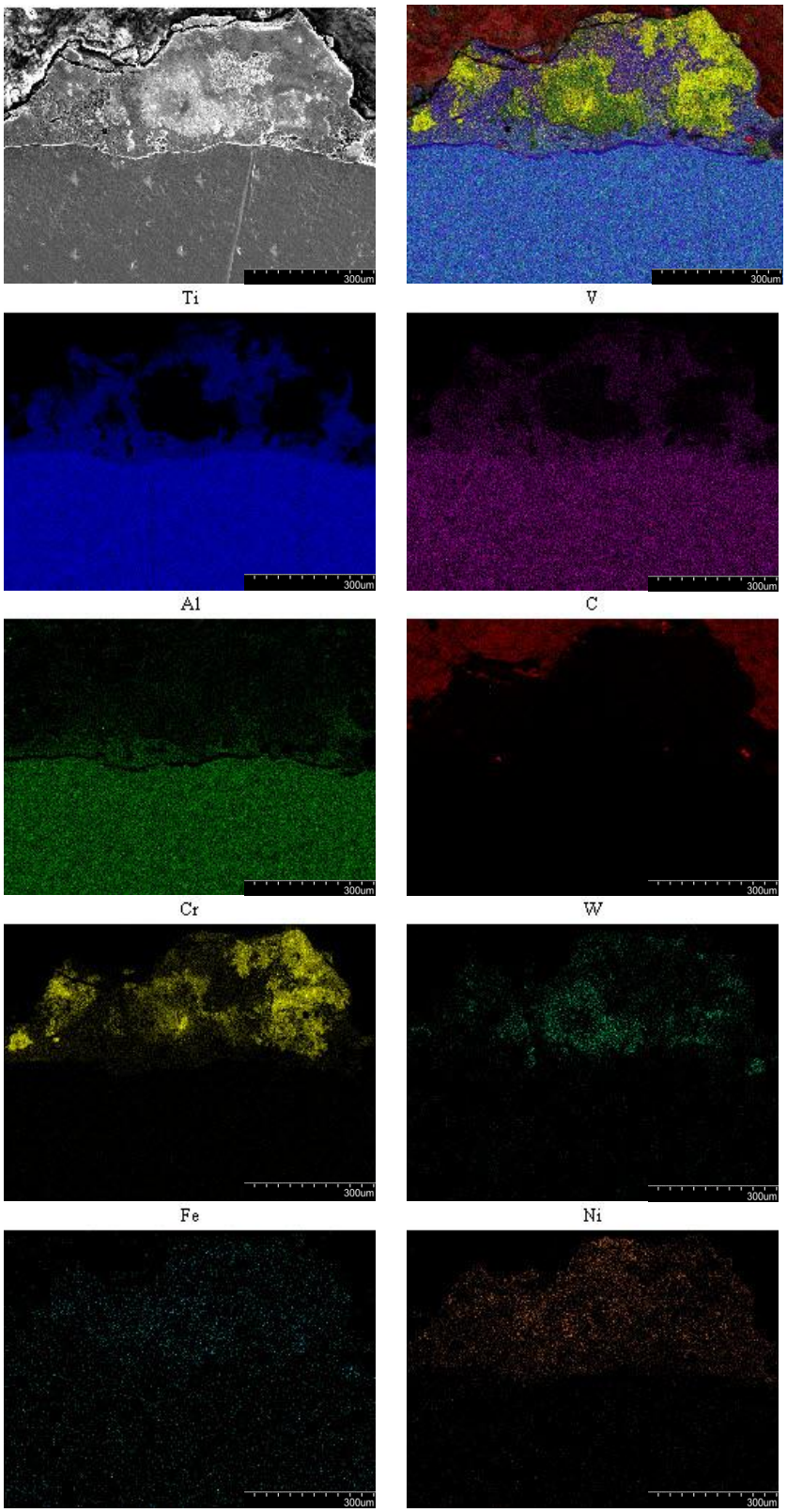

Figure 47. EDS element maps for specimen Ti1-02

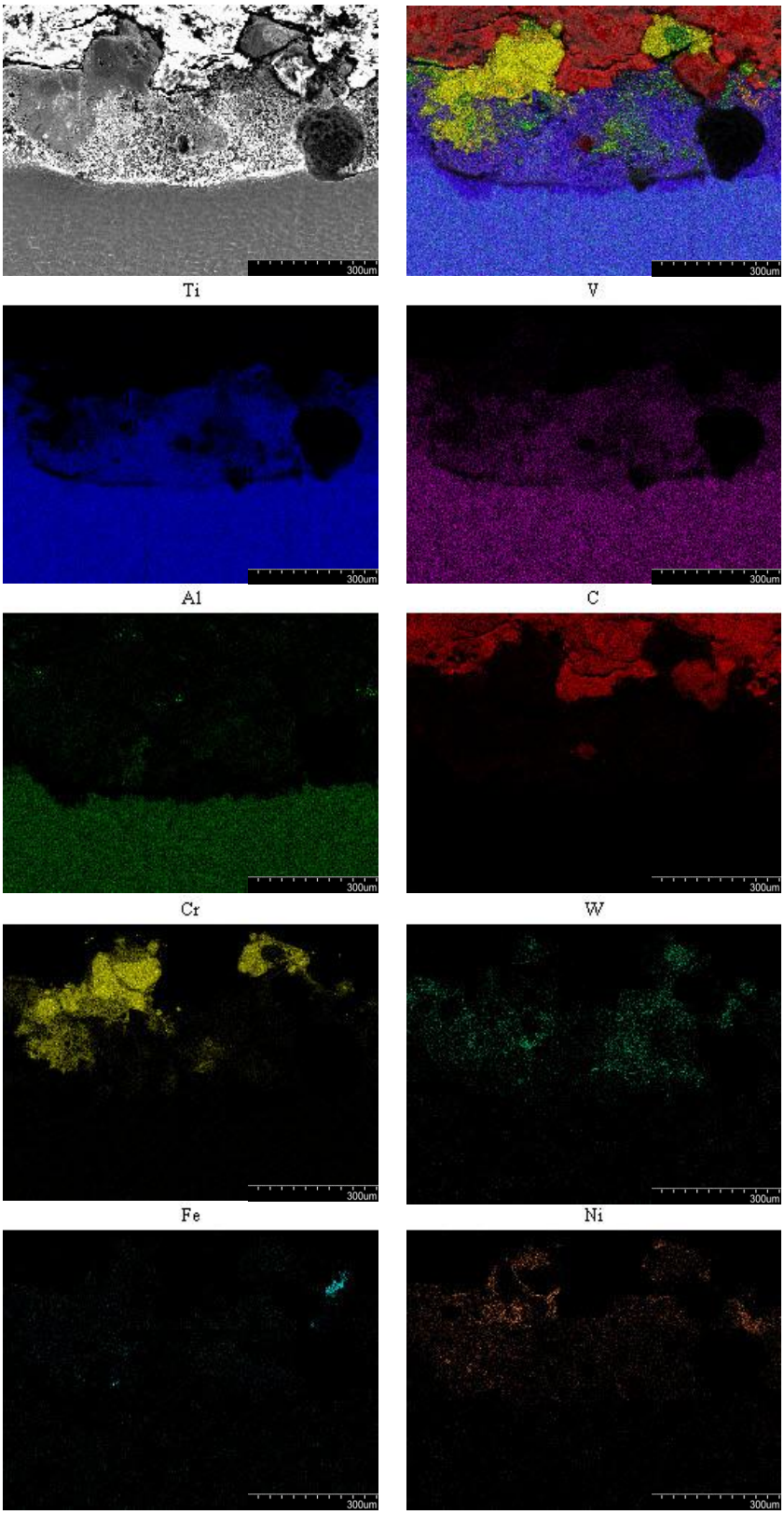

Figure 48. EDS element maps for specimen Ti1-03

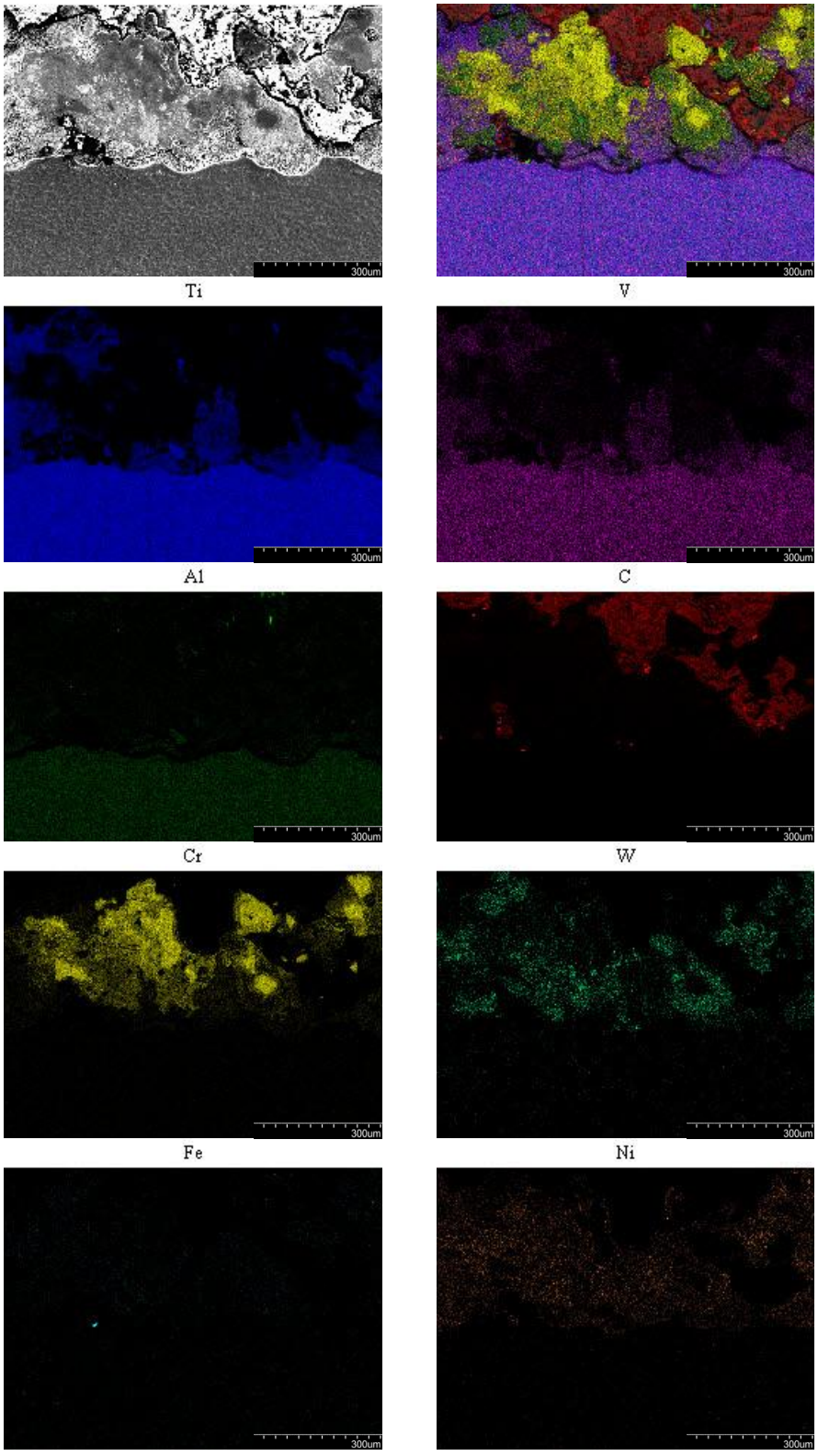

Figure 49. EDS element maps for specimen Ti1-04

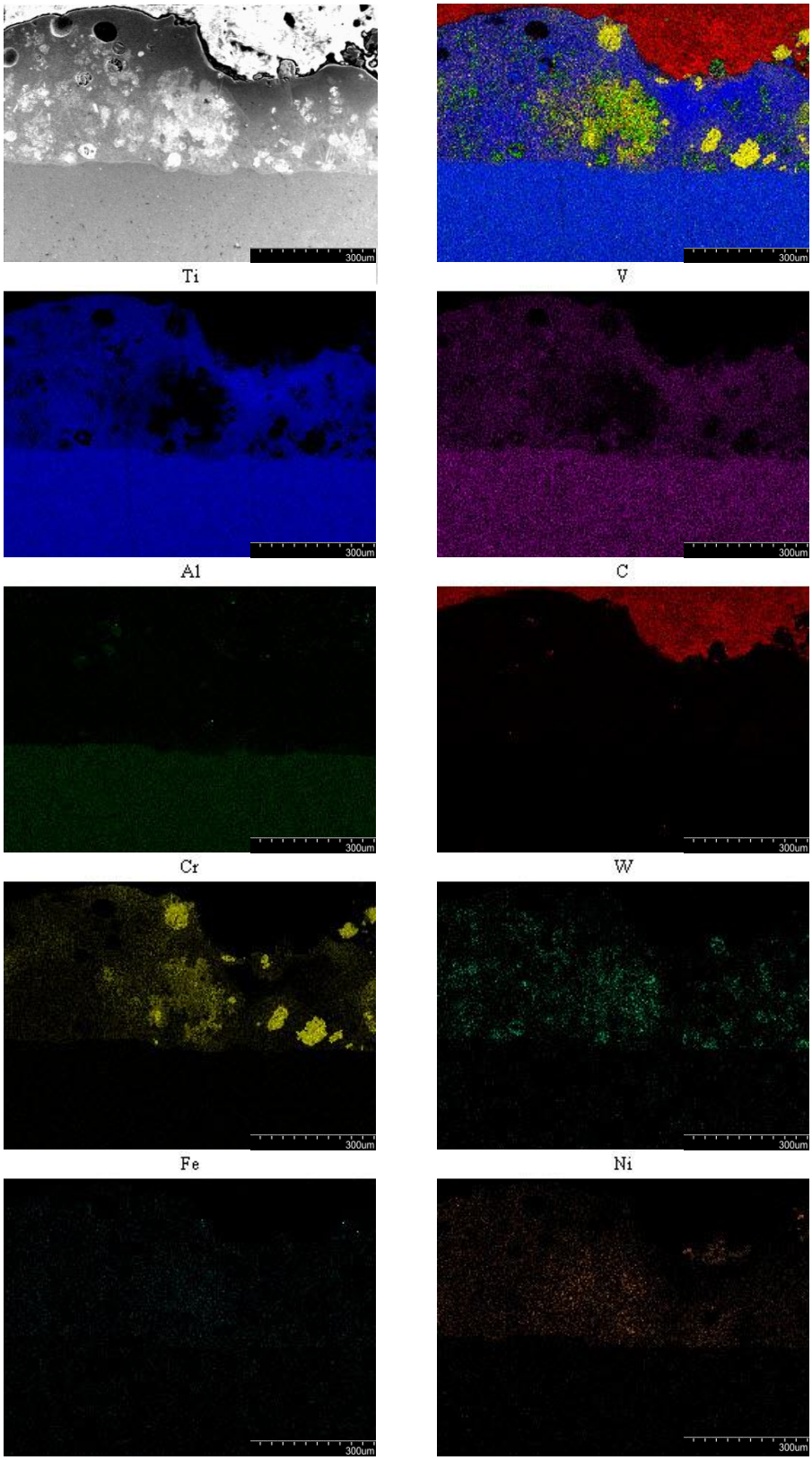

Figure 50. EDS element maps for specimen Ti2-01

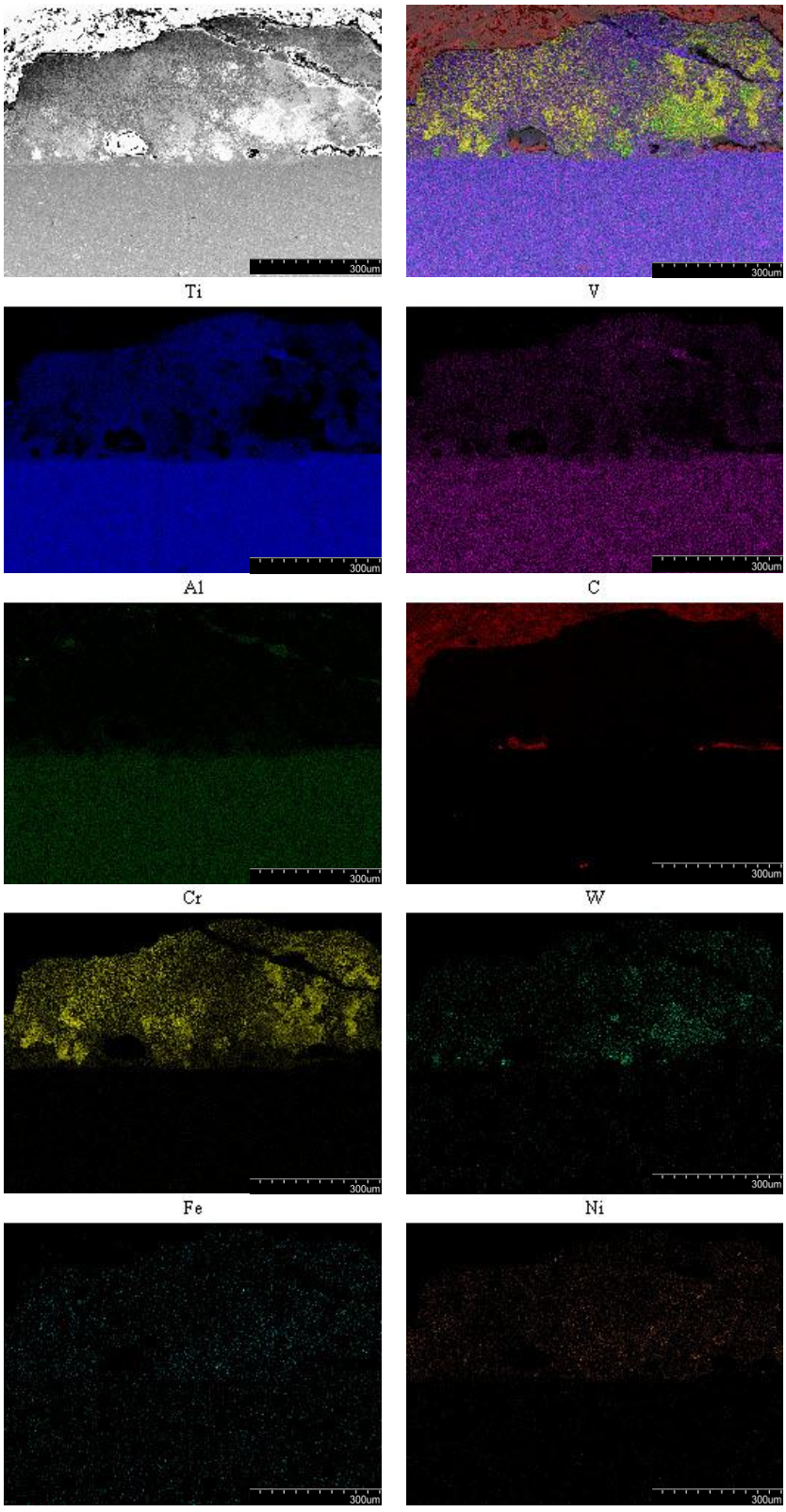

Figure 51. EDS element maps for specimen Ti2-02

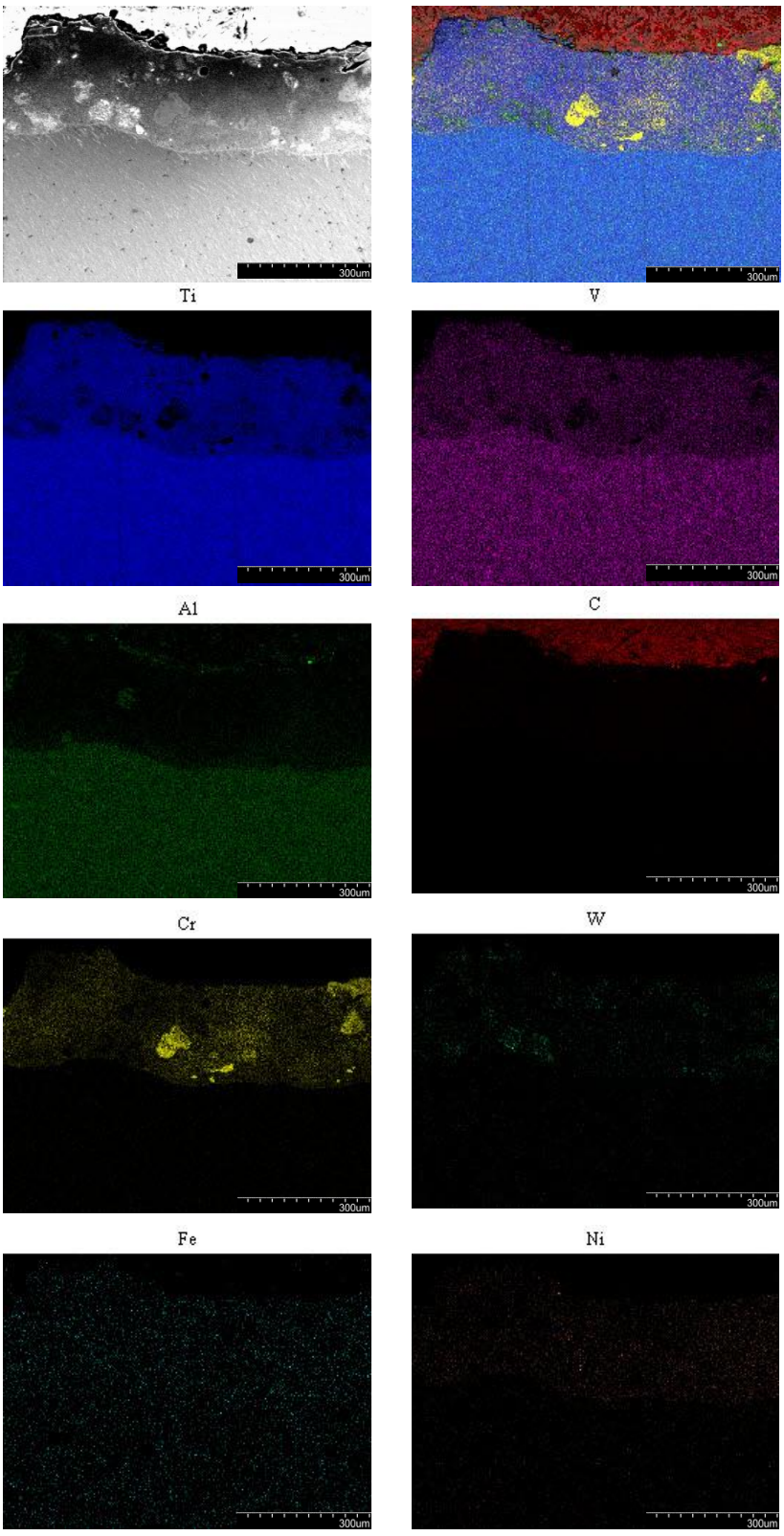

Figure 52. EDS element maps for specimen Ti2-03

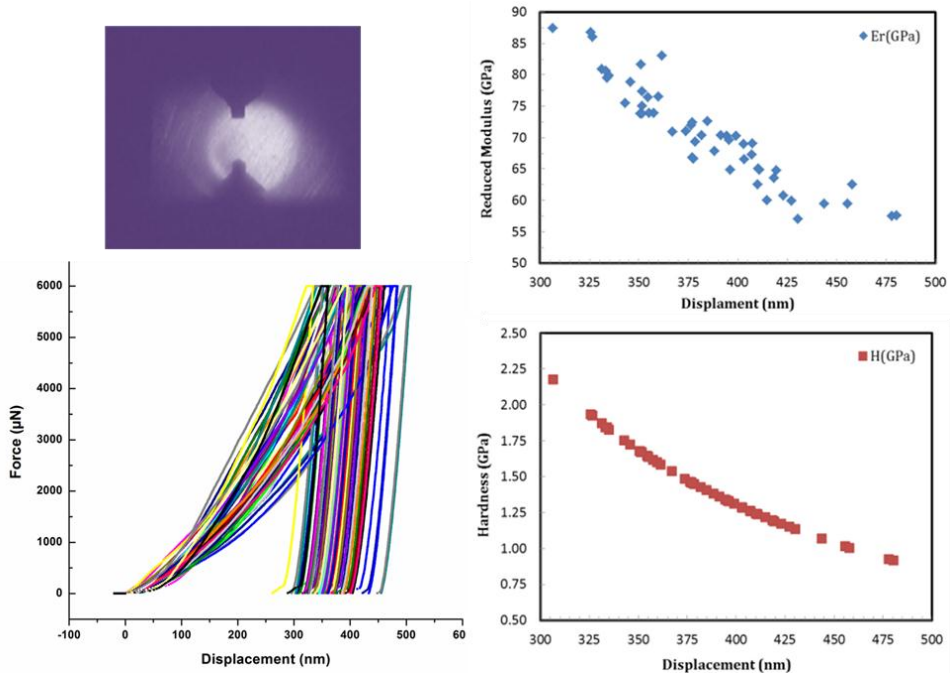

Figure 53. Location, P vs. displacement curves, and H and E_r vs. h_c for AA 7075.

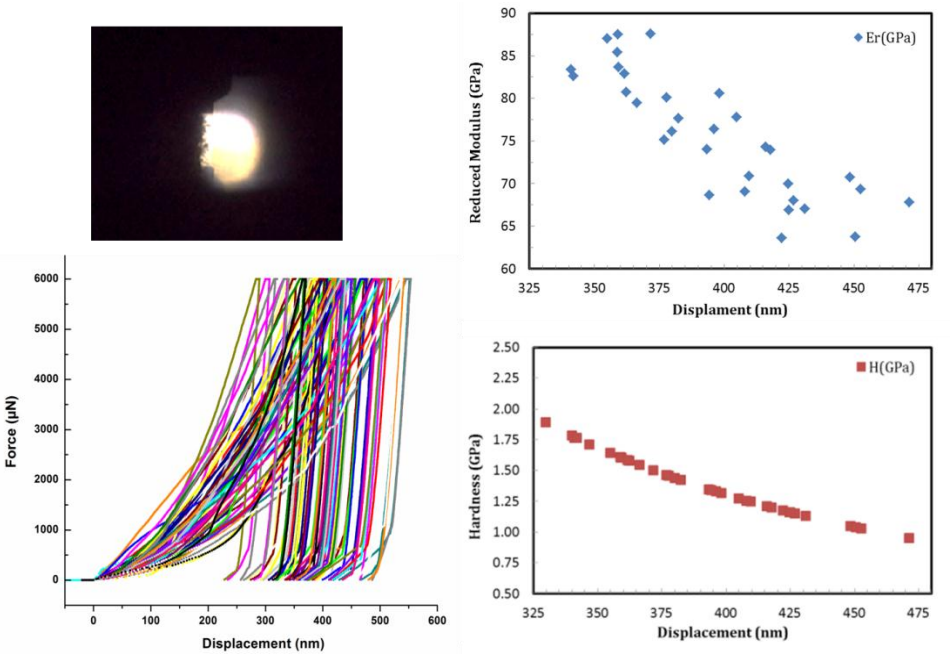

Figure 54. Location, P vs. displacement curves, and H and E_r vs. h_c for 6W6Al1.

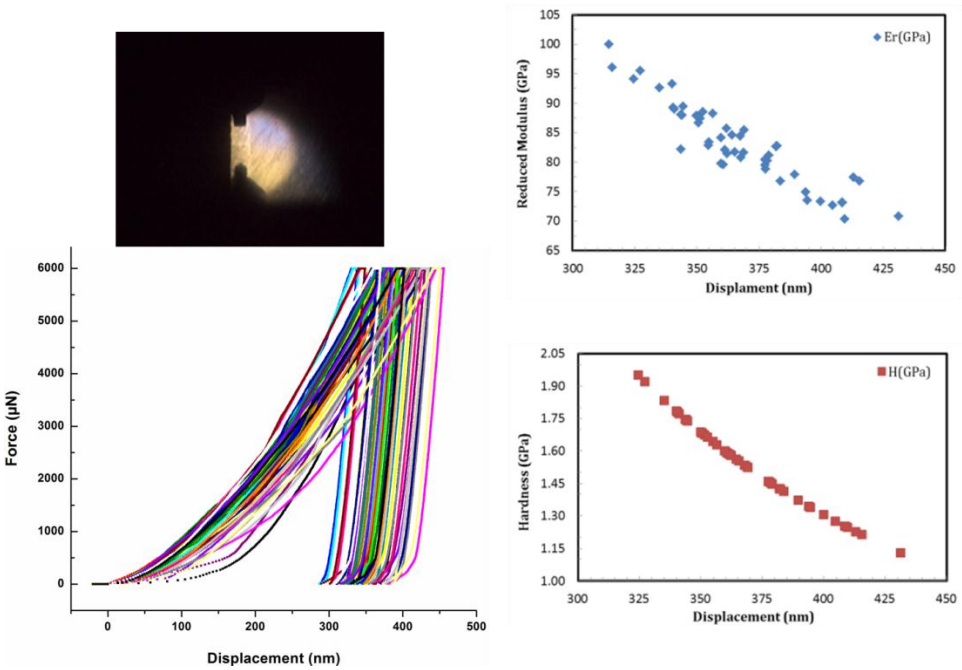

Figure 55. Location, P vs. displacement curves, and H and E_r vs. h_c for 6W8AL1.

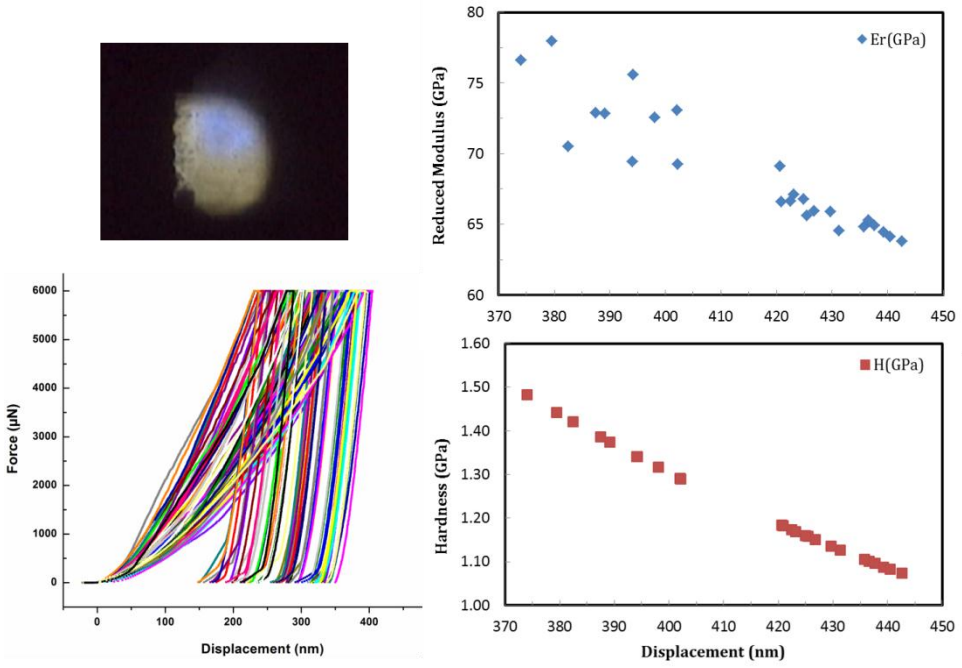

Figure 56. Location, P vs. displacement curves, and H and E_r vs. h_c for 6W10AL1.

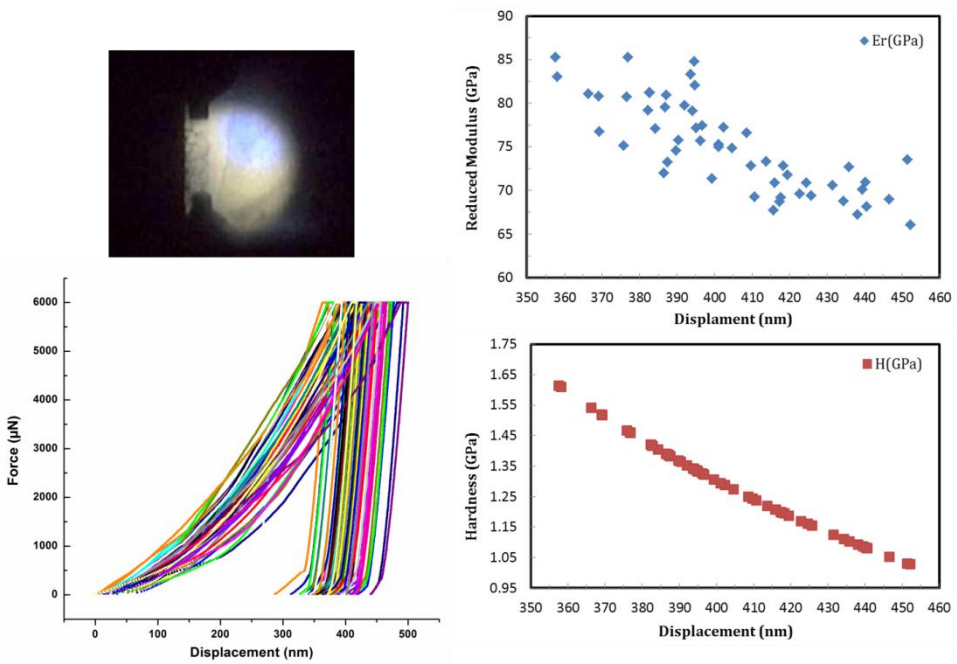

Figure 57. Location, P vs. displacement curves, and H and E_r vs. h_c for 7W13AL1.

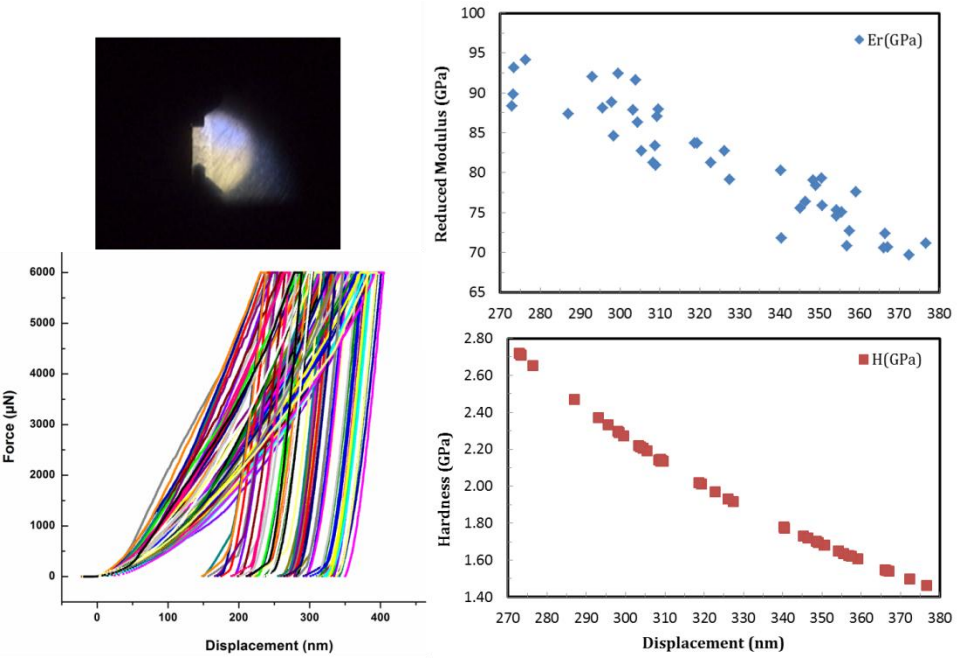

Figure 58. Location, P vs. displacement curves, and H and E_r vs. h_c for 7W16AL1.

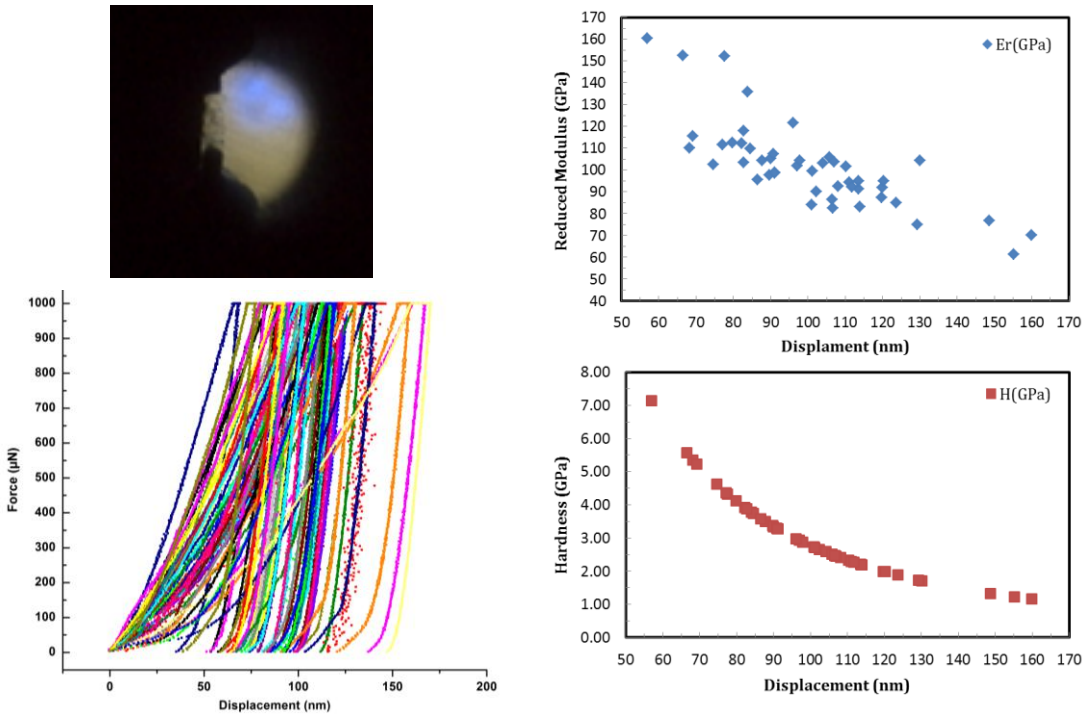

Figure 59. Location, P vs. displacement curves, and H and E_r vs. h_c for 8W15-3.0AL2.

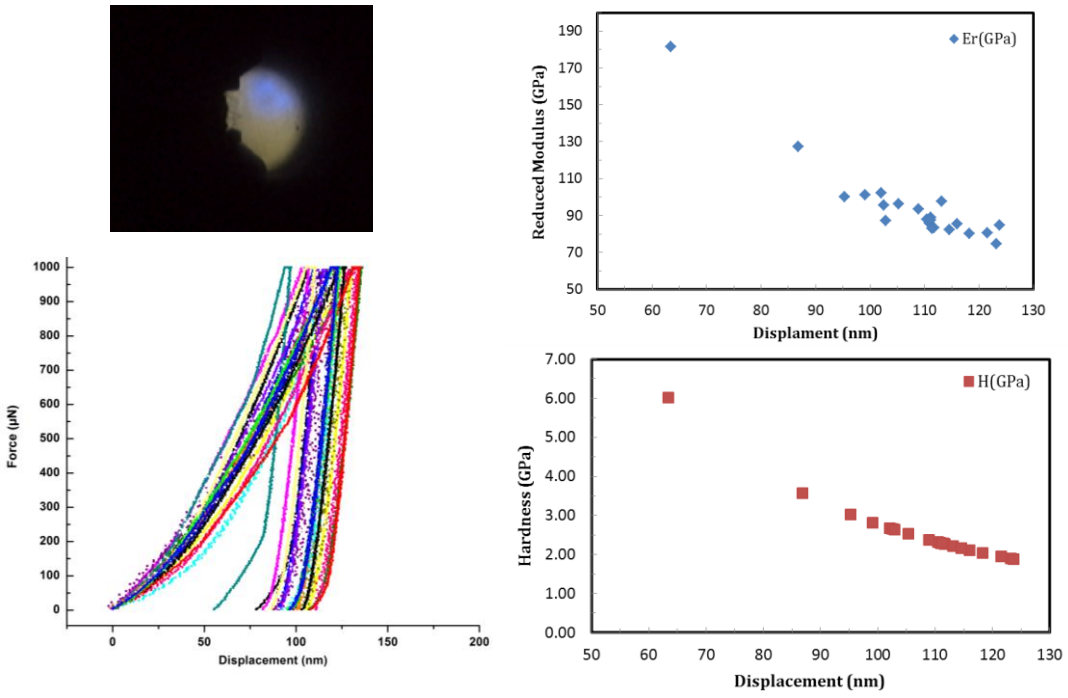

Figure 60. Location, P vs. displacement curves, and H and E_r vs. h_c for 8W15-2.0AL2.

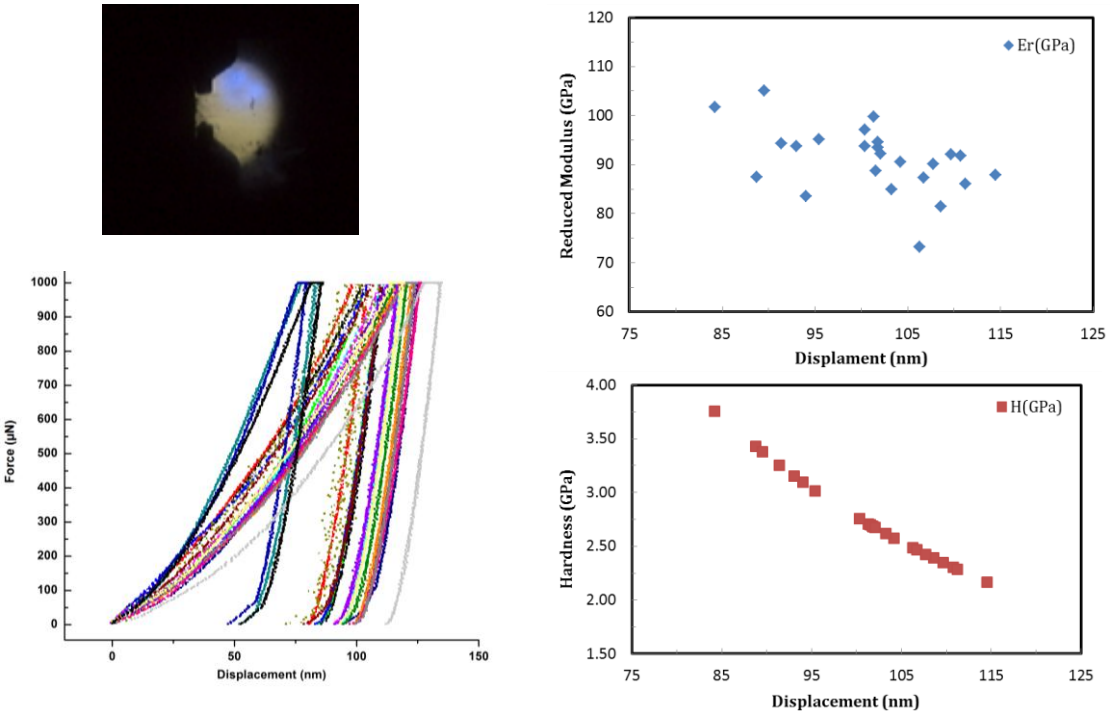

Figure 61. Location, P vs. displacement curves, and H and E_r vs. h_c for 7.5W15-3.0AL2.

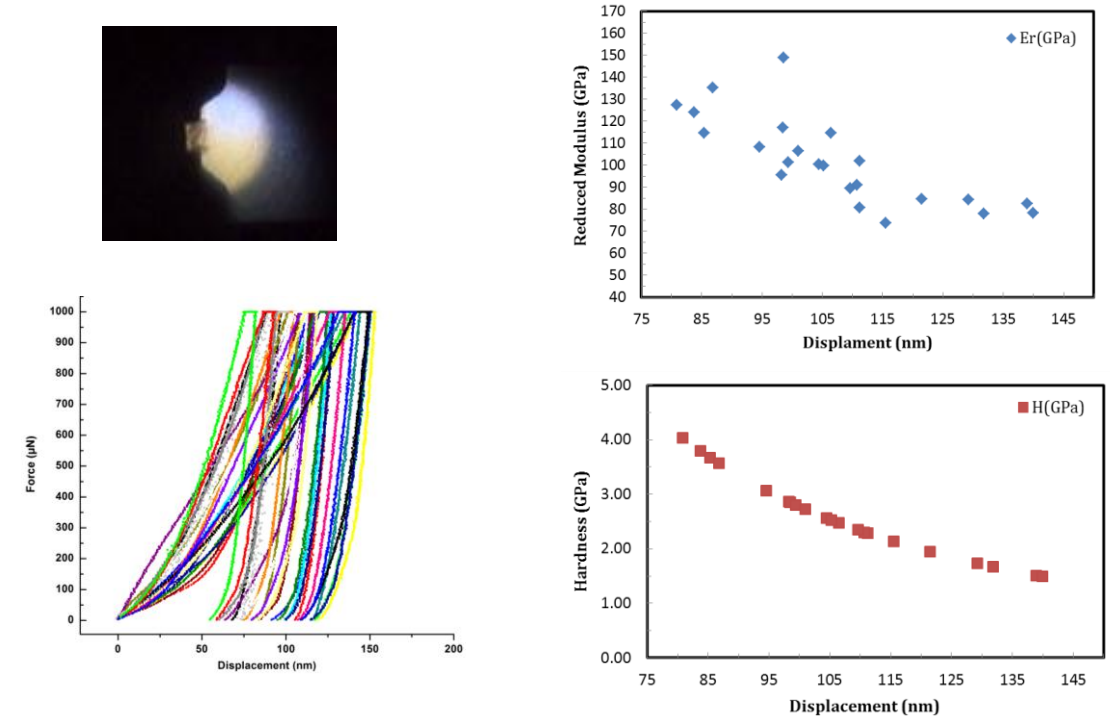

Figure 62. Location, P vs. displacement curves, and H and E_r vs. h_c for 7.5W15-2.0AL2.

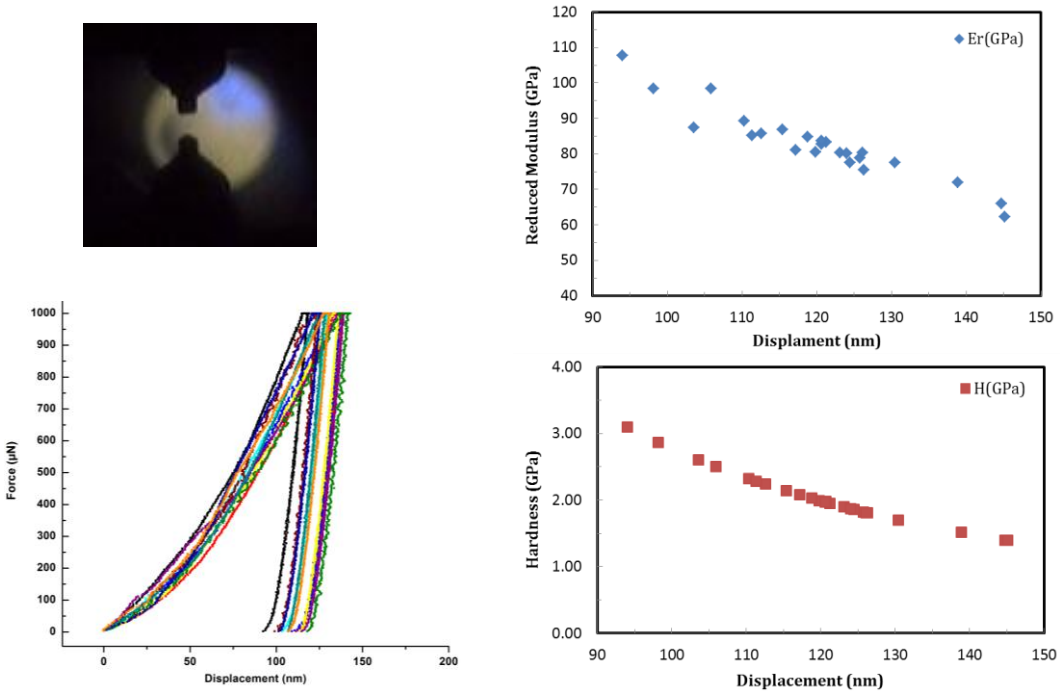

Figure 63. Location, P vs. displacement curves, and H and E_r vs. h_c for AA 5083.

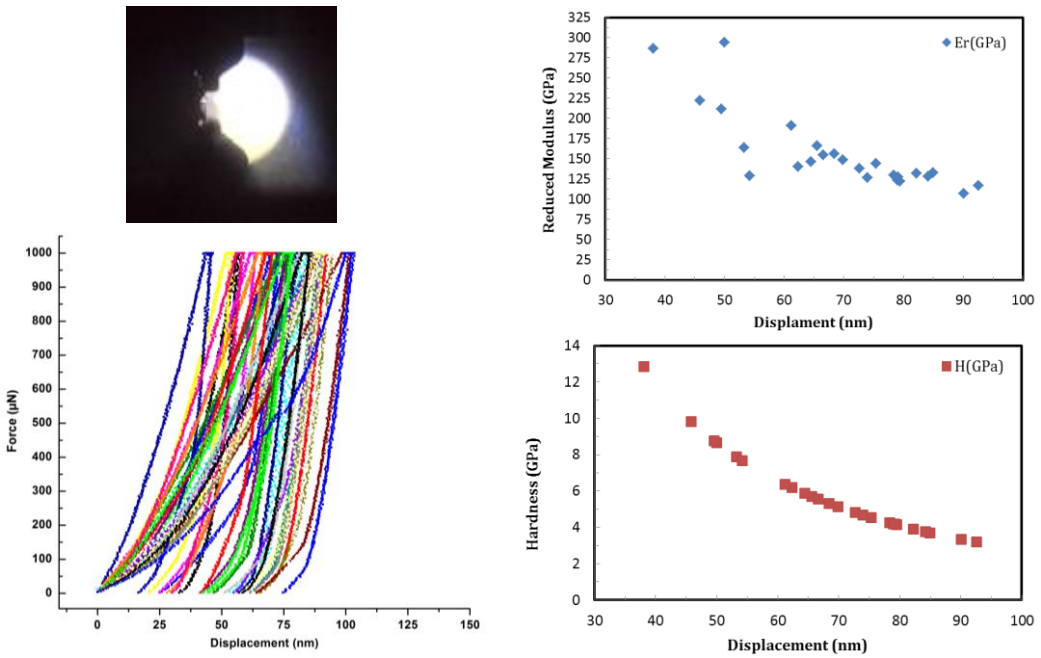

Figure 64. Location, P vs. displacement curves, and H and E_r vs. h_c for Ti1-01.

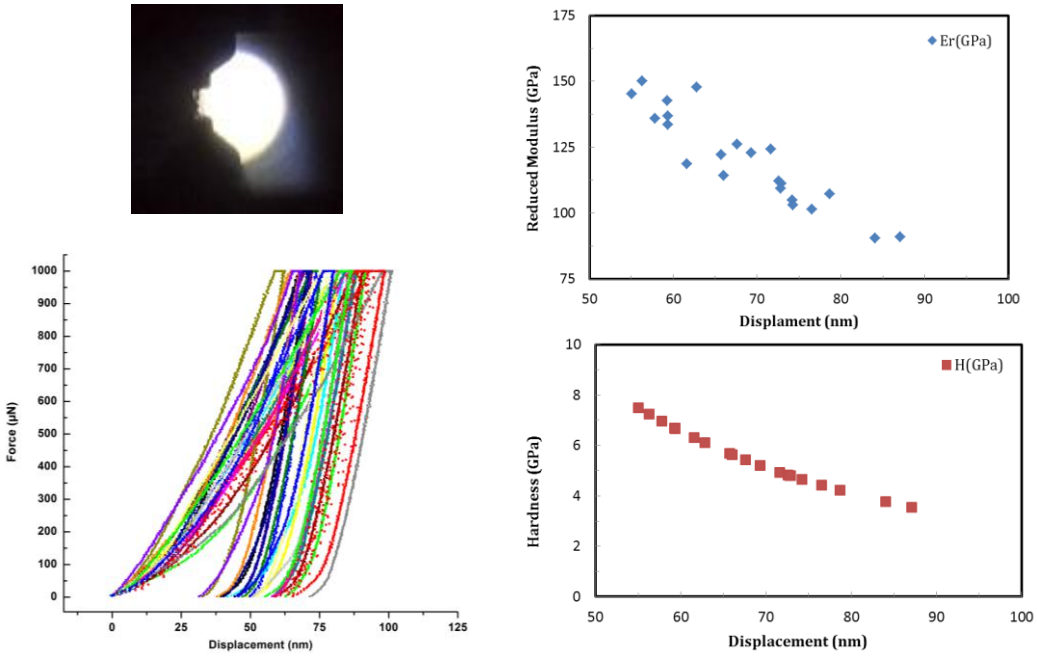

Figure 65. Location, P vs. displacement curves, and H and E_r vs. h_c for Ti1-02.

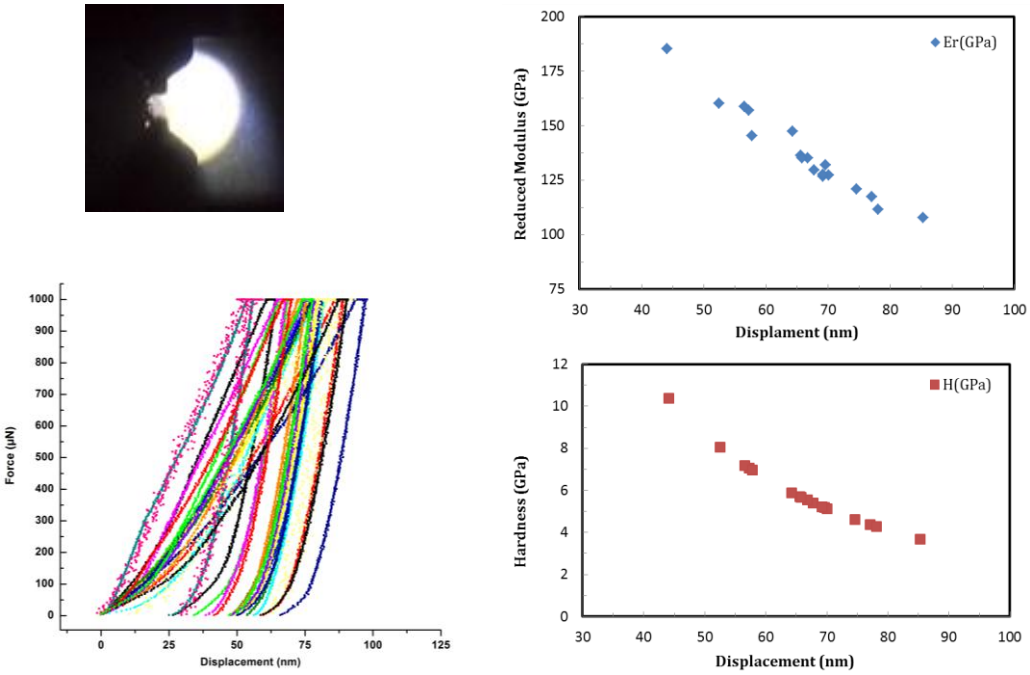

Figure 66. Location, P vs. displacement curves, and H and E_r vs. h_c for Ti1-03.

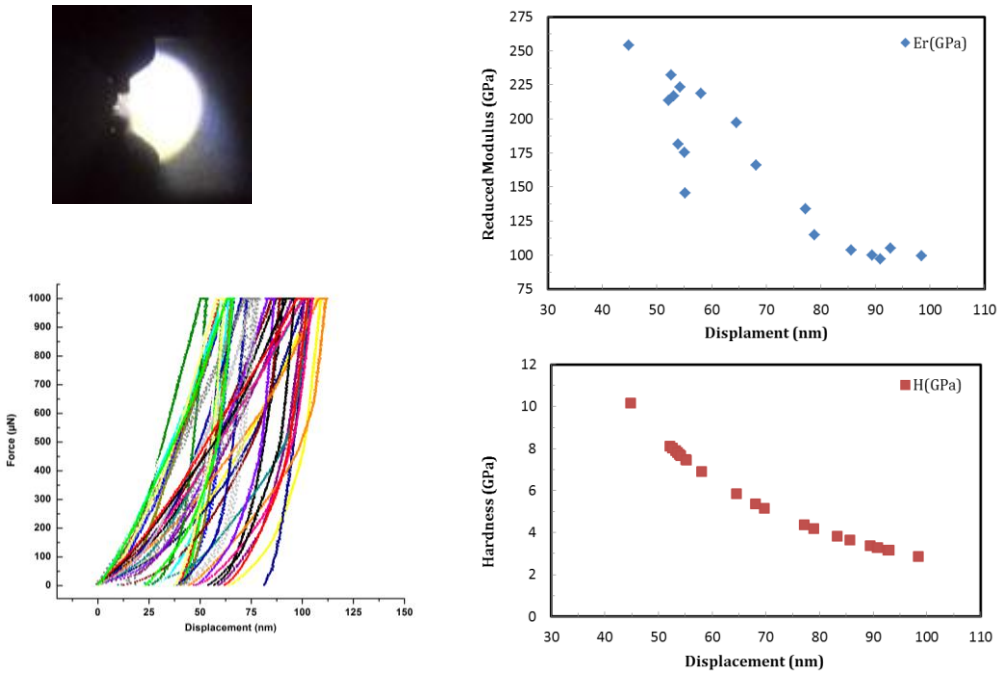

Figure 67. Location, P vs. displacement curves, and H and E_r vs. h_c for Ti1-04.

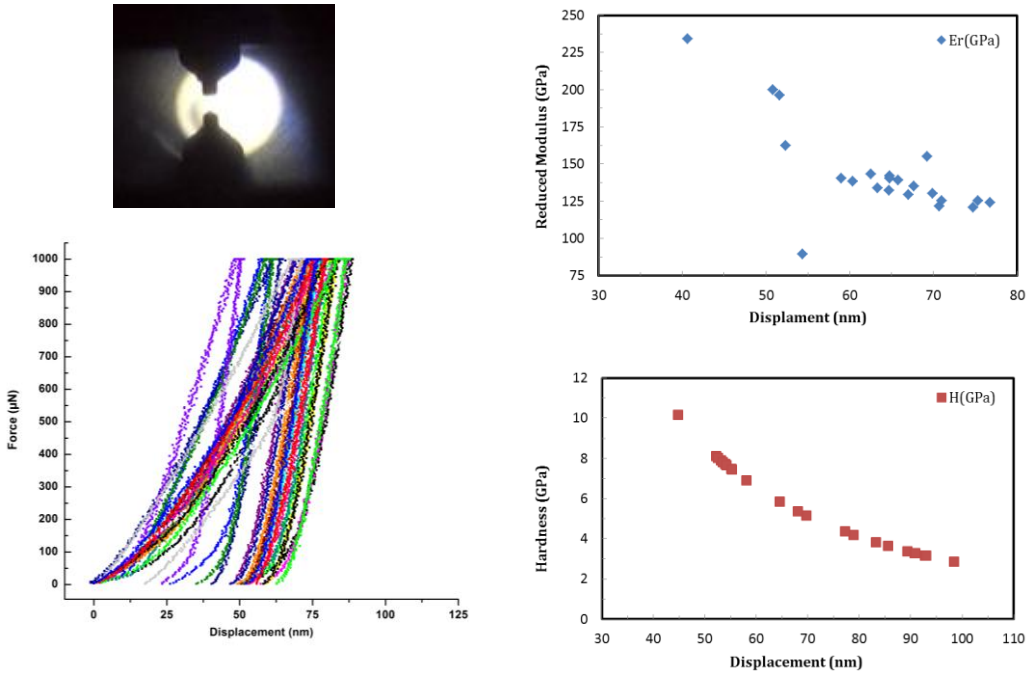

Figure 68. Location, P vs. displacement curves, and H and E_r vs. h_c for Ti2-01.

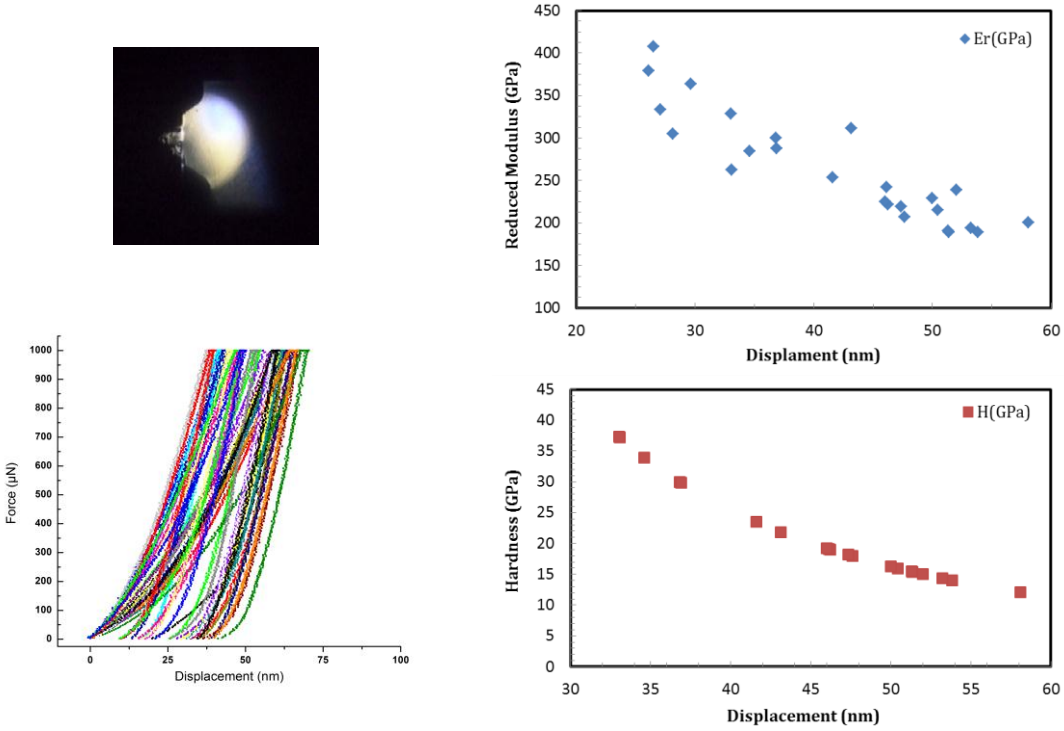

Figure 69. Location, P vs. displacement curves, and H and E_r vs. h_c for Ti2-02.

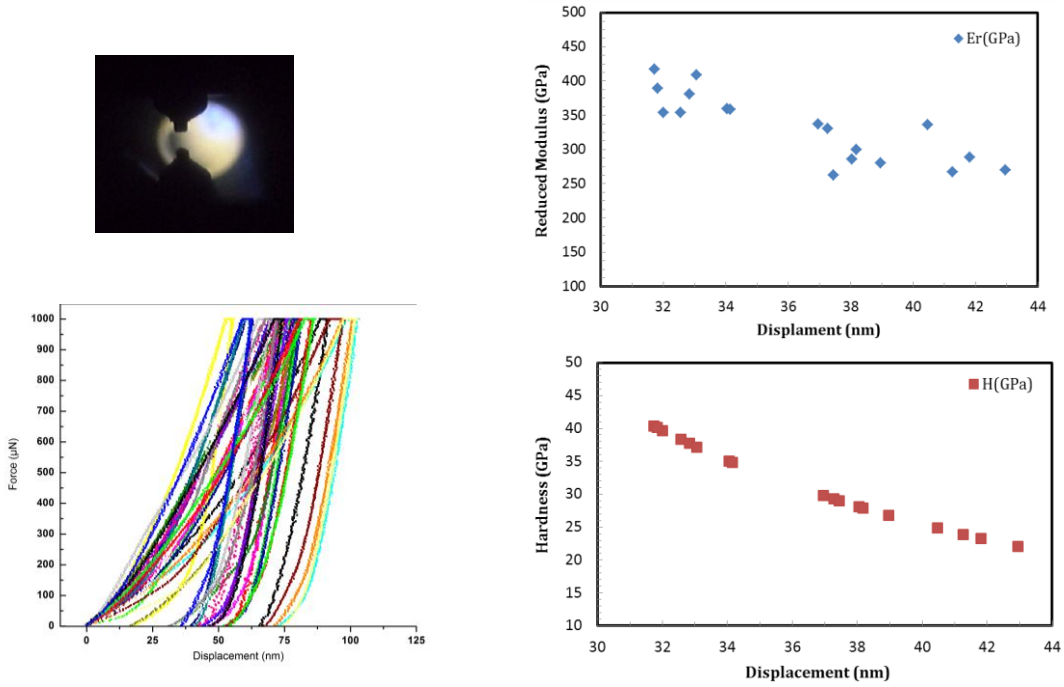

Figure 70. Location, P vs. displacement curves, and H and E_r vs. h_c for Ti2-03.

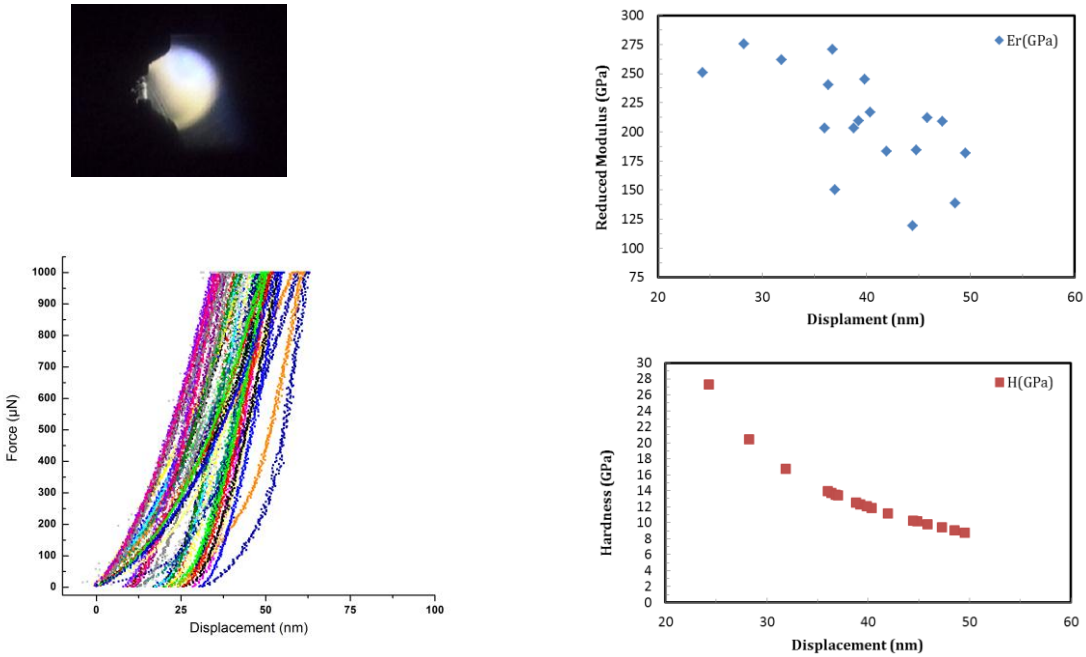

Figure 71. Location, P vs. displacement curves, and H and E_r vs. h_c for Ti6Al4V.

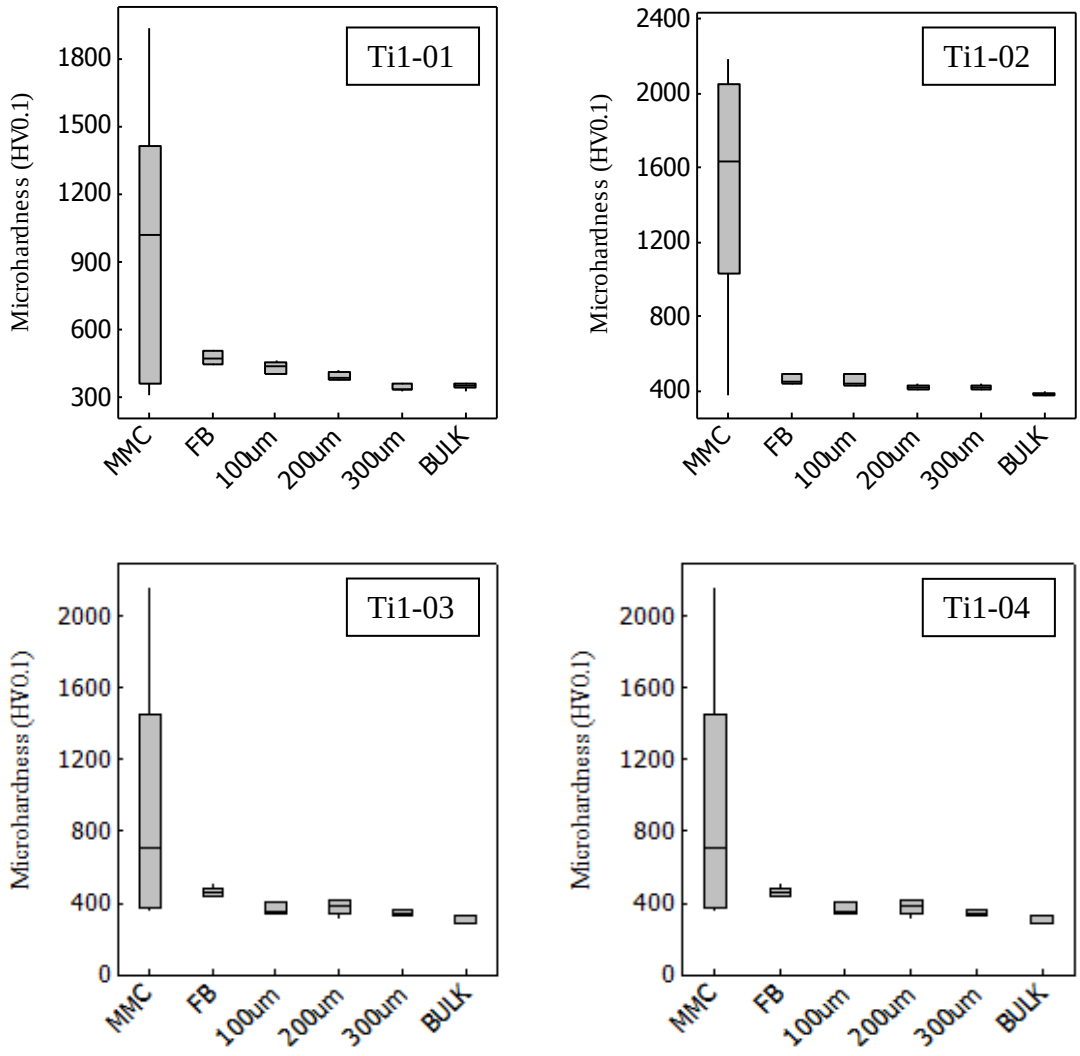

Figure 72. Microhardness (Vickers) cross-sectional profiles of Ti1-MMCs. Indentations were taken in the MMC, Fusion Boundary (FB), at incremental distances from the FB zone and in the bulk material (Ti6Al4V)

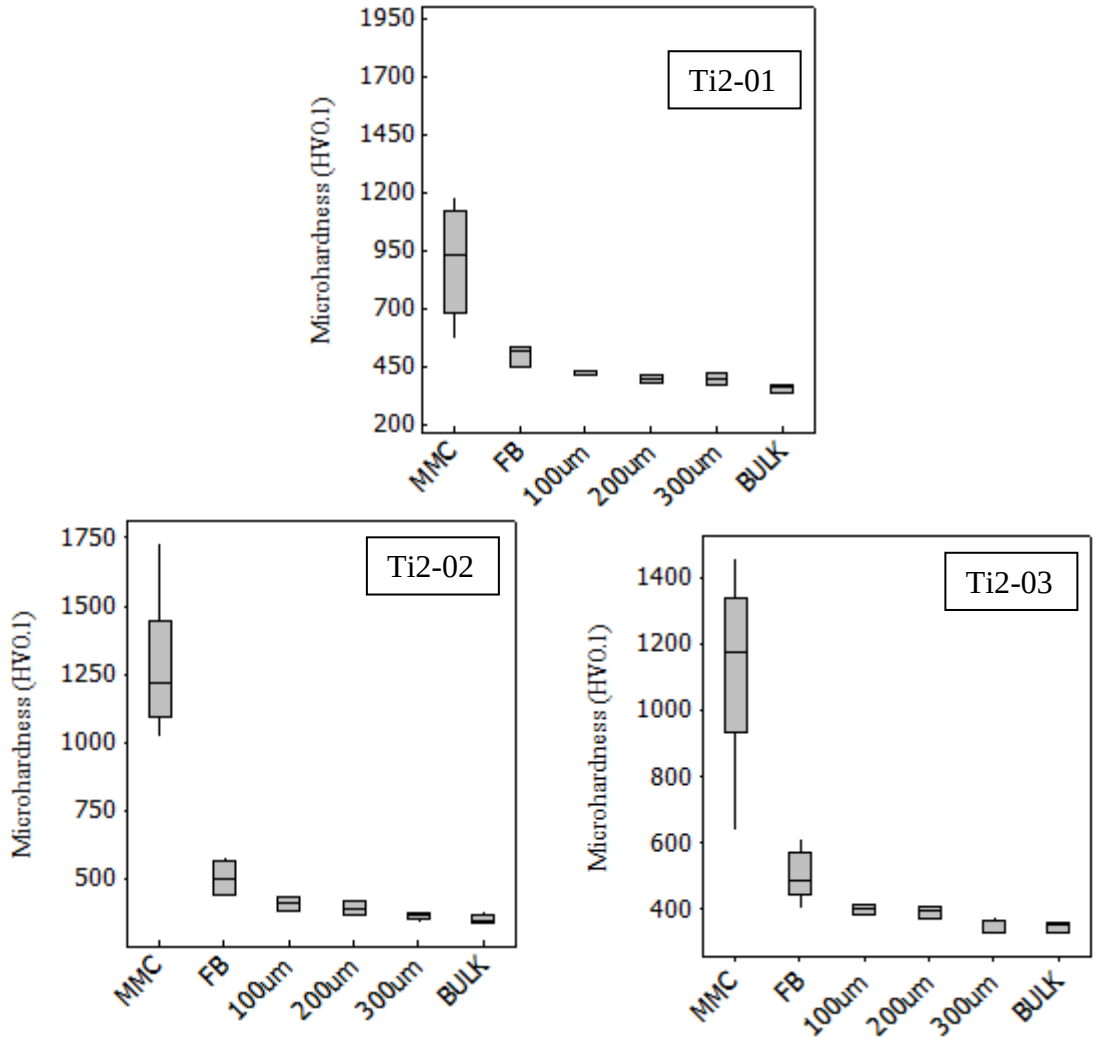

Figure 73. Microhardness (Vickers) cross-sectional profiles of Ti2-MMCs. Indentations were taken in the MMC, Fusion Boundary (FB), at incremental distances from the FB zone and in the bulk material (Ti6Al4V)

Table 9. Average Microhardness (Vickers) and standard deviation in the MMC, Fusion Boundary (FB), at incremental distances from the FB zone and in the bulk material (Ti6Al4V)

	Ti1-01		Ti1-02		Ti1-03		Ti1-04		Ti2-01		Ti2-02		Ti2-03	
	$\bar{Y}$	σ	$\bar{Y}$	σ	$\bar{Y}$	σ	$\bar{Y}$	σ	$\bar{Y}$	σ	$\bar{Y}$	σ	$\bar{Y}$	σ
MMC	965	561	1487	607	958	647	1234	400	905	226	1281	224	1117	269
FB	472	28	458	25	457	30	438	34	493	48	501	63	501	77
100 um	428	26	452	31	363	31	389	22	413	11	407	26	395	16
200um	388	18	414	13	374	43	366	18	394	18	390	24	390	19
300um	338	14	411	11	339	17	369	21	390	24	359	15	342	21
BULK	348	13	373	12	306	23	333	29	349	17	348	16	344	16

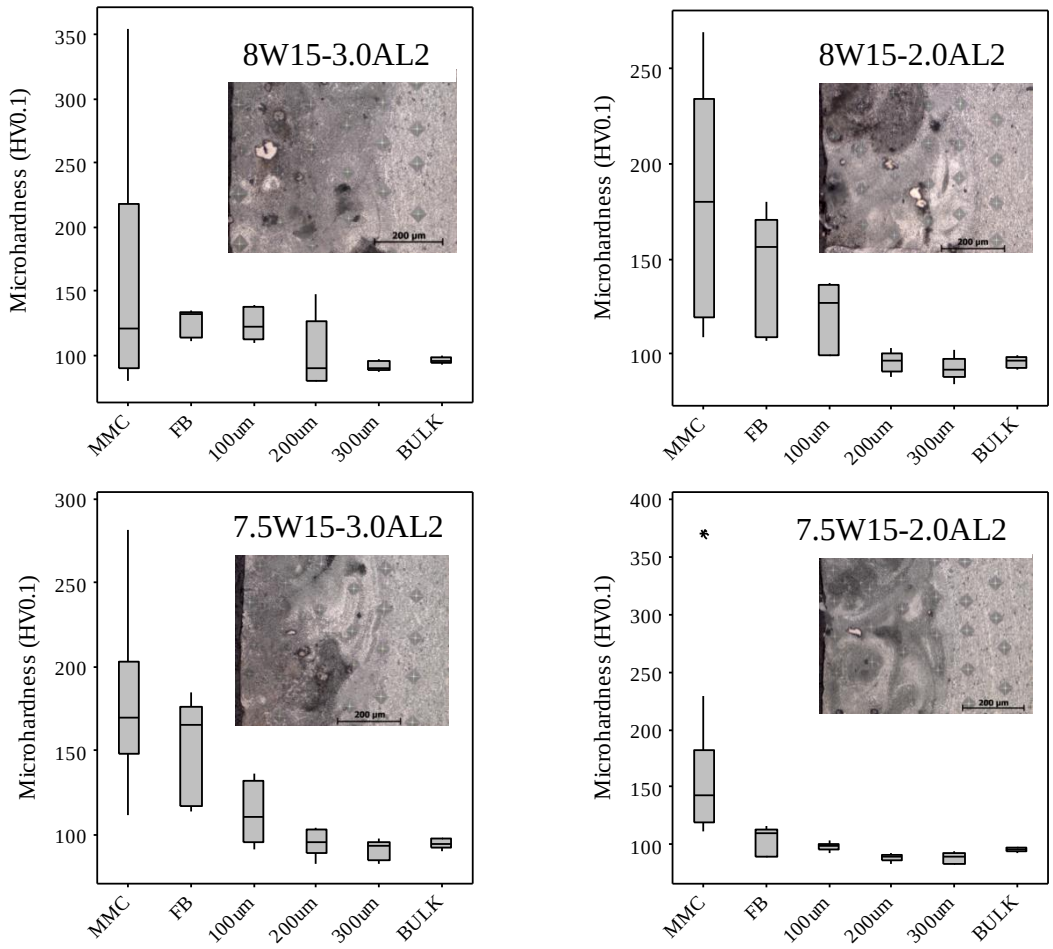

Figure 74. Microhardness (Vickers) cross-sectional profiles of Al2-MMCs. Indentations were taken in the MMC, Fusion Boundary (FB), at incremental distances from the FB zone and in the bulk material (AA 5083)

Table 10. Average microhardness (Vickers) and standard deviation in the MMC, Fusion Boundary (FB), at incremental distances from the FB zone and in the bulk material (Ti6Al4V)

	8W15-3.0AL2		8W15-2.0AL2		7.5W15-3.0AL2		7.5W15-2.0AL2	
	$\bar{Y}$	σ	$\bar{Y}$	σ	$\bar{Y}$	σ	$\bar{Y}$	σ
MMC	157	91	181	59	176	47	168	79
FB	125	11	143	32	150	32	104	13
100um	125	13	119	19	114	19	98	4
200um	101	28	95	5	96	8	89	3
300um	91	4	92	6	91	6	89	5
BULK	96	3	96	3	95	3	96	2

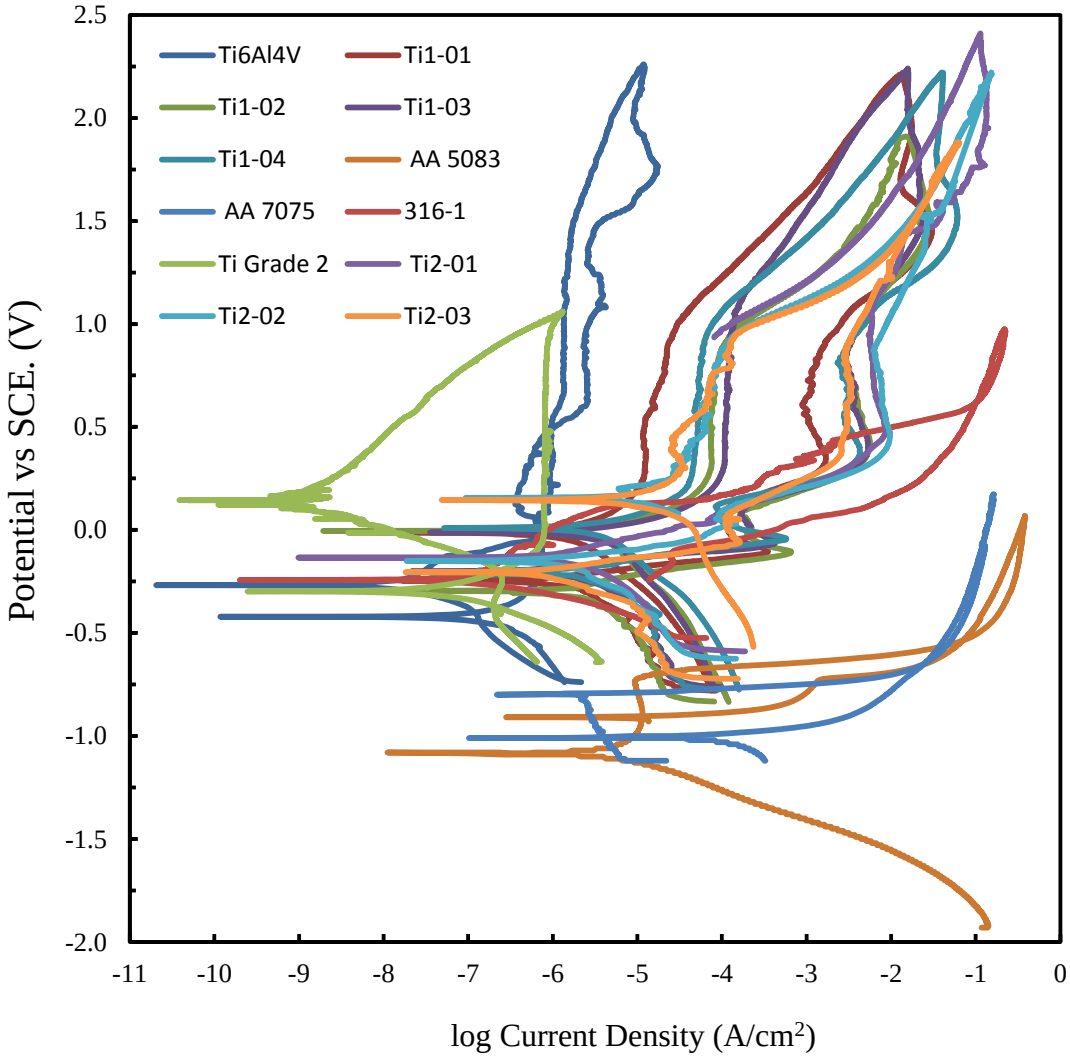

Figure 75. Cyclic potentiodynamic polarization curves for Ti6Al4V, AA 7075, AA 5083, Ti- and Al-MMCs, Ti (grade 2), and 316 SS.

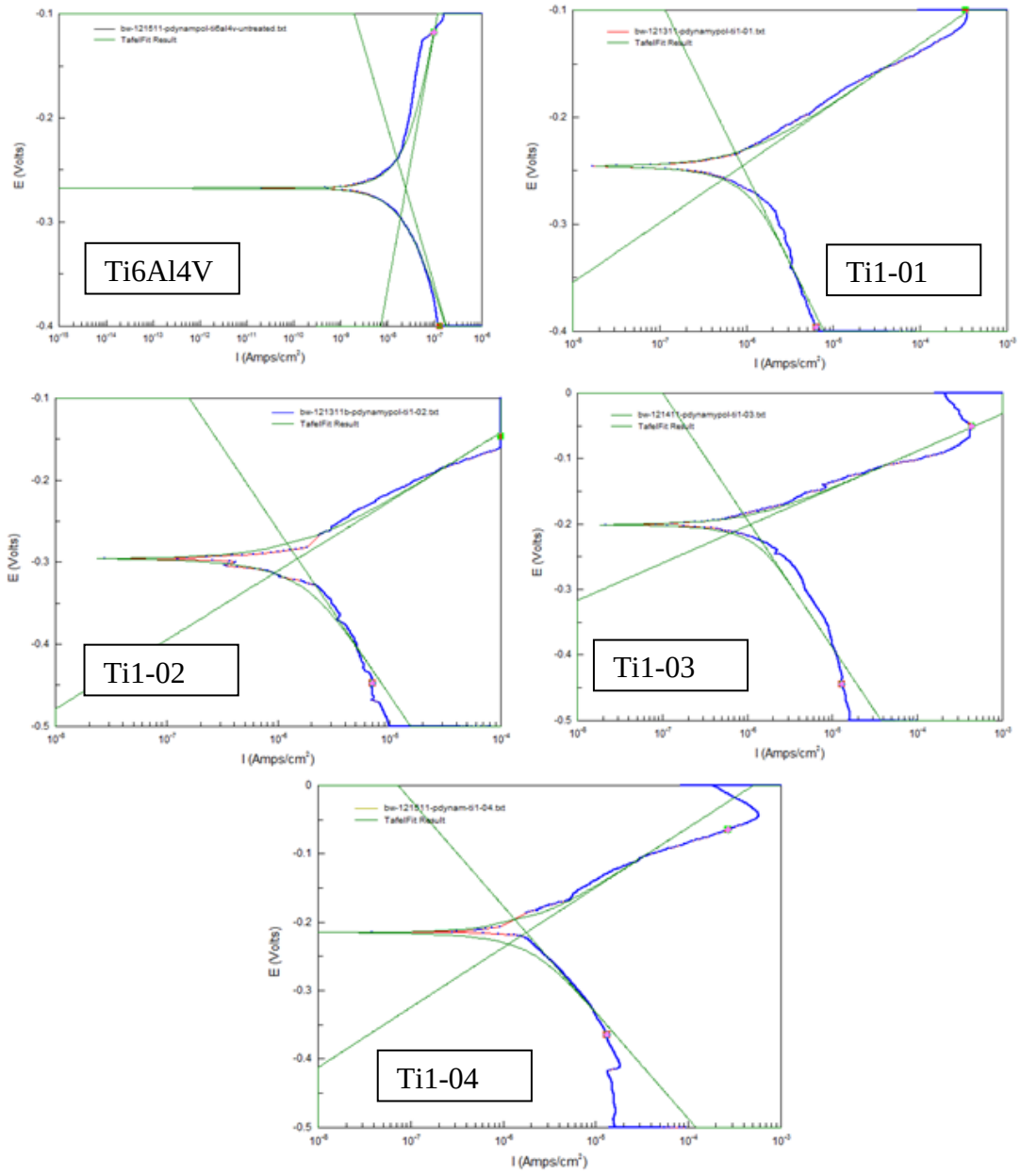

Figure 76. Ti1-MMC tafel curves plotted in CorrView® to determine the corrosion rate. The corrosion rate is directly proportional to the corrosion current: the current at which the anodic and cathodic current densities intersect.

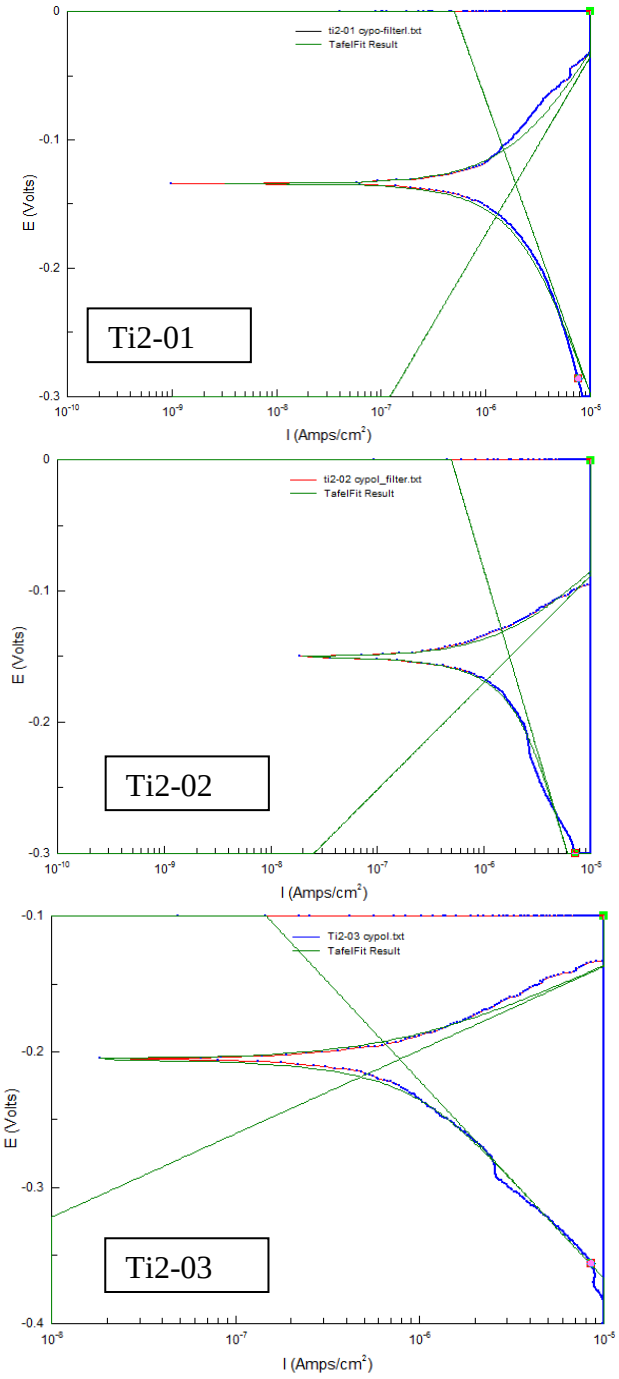

Figure 77. Ti2-MMC tafel curves plotted in CorrView® to determine the corrosion rate. The corrosion rate is directly proportional to the corrosion current: the current at which the anodic and cathodic current densities intersect.

REFERENCES

[1] E. Toyserkani, A. Khajepour, and S. Corbin, Laser Cladding CRC Press, Boca Raton, Florida, (2005).

[2] K. Zhang, J. Zou, J. Li, Z.-S. Yu, and H. Wang, Transactions of Nonferrous Metals Society of China (2009) 2192-2197.

[3] R.L. Sun, D.Z. Yang, L.X. Guo, and S.L. Dong, Surface and Coatings Technology 135 (2001) 307-312.

[4] L. Sexton, S. Lavin, G. Byrne, and A. Kennedy, Journal of Materials Processing Technology 122 (2002) 63-68.

[5] J.P. Kruth, M.C. Leu, and T. Nakagawa, CIRP Annals - Manufacturing Technology 47 (1998) 525-540.

[6] S. Suresh, A. Mortensen, and A. Needleman, Fundamentals of Metal-Matrix Composites Butterworth-Heinemann, Stoneham, MA, (1993).

[7] K.U. Kainer, Metal Matrix Composites Wiley-VCH, (2003).

[8] A. Rabiei, L. Vendra, and T. Kishi, Composites Part A: Applied Science and Manufacturing 39 (2008) 294-300.

[9] J.A. Lee and D.L. Mykkanen, Metal and Polymer Matrix Composites Noyes Data Corporation, Park Ridge, New Jersey, (1987).

[10] J.E. Schoutens and D.A. Zarate, Composites 17 (1986) 188-204.

[11] T.J. Downes and J.E. King, Composites 24 (1993) 276-281.

[12] J. Sampedro, I. Perez, B. Carcel, J.A. Ramos, and V. Amigo, Lasers in Manufacturing - Proceedings of the Sixth International WLT Conference on Lasers in Manufacturing. (2011) 313-322.

[13] J.E. Hatch, Aluminum: Properties and Physical Metallurgy ASM International, (1984).

[14] V.E. Carter, Metallic Coatings For Corrosion Control Nesnes-Butterworths, London, (1977).

[15] K. Samar Jyoti, Microstructure and corrosion properties of diode laser melted friction stir weld of aluminum alloy 2024 T351. Applied Surface Science (2011) 3985-3997.

[16] D.S. Stewart, Principles of Corrosion Protection Macmillian, London, (1968).

[17] M.J. Donachie, Titanium: A Technical Guide. ASM International. (2000).

[18] F.L. LaQue and H.R. Copson, Corrosion Resistance of Metals and Alloys Reinhold Publishing Corporation, New York, (1966).

[19] Y. Shimizu, T. Nishimura, and I. Matsushima, Materials Science and Engineering: A 198 (1995) 113-118.

[20] L.H. Hihara, Shreir's Corrosion: Corrosion of Metal Matrix Composites. Elsevier. (2010) 2250-2269.

[21] J. Zhu and L.H. Hihara, Corrosion Science (2010) 406-415.

[22] S.D. Cramer and B.S. Covino, ASM Handbook ASM International, (2005).

[23] A. Mortensen and J.A. Cornie, JOM . 40 (1988) 237.

[24] R.A. Arsenault, Metal Matrix Composites: Mechanisms and Properties Academic Press, (1991).

[25] D.W. Shoesmith, J.J. Noel, Shreir's Corrosion: Corrosion of Titanium and its Alloys, Elsevier (2010) 2042-2052.

[26] L.H. Hihara and C. Tamirisa, Materials Science and Engineering: A 198 (1995) 119-125.

[27] H. Brown, Aluminum and its Applications. Pitman Publishing Corporation. (1948).

[28] L. Dudley, Light Metals In Structural Engineering Temple Press, Great Britain, (1947).

[29] H. Sun, E.Y. Koo, and H.G. Wheat, Corrosion Science 47 (1991) 741.

[30] A.J. Griffiths and A. Turnbull, Corrosion Science 36 (1994) 23-35.

[31] H. Fukunaga, X. Wang, and Y. Aramaki, Journal of Material Science (1990).

[32] E. Tank. Cast composite materials having an Al-Mg matrix alloy. U.S. Patent No. 4943313 . (1992).

[33] E.M. Klier, A. Mortensen, J.A. Cornie, and M.C. Flemings, Fabrication of cast particle-reinforced metals via pressure infiltration. Jourrnal of Materials Science. (1991) 2519-2526.

[34] R.B. Bhagat, R.K. Everett, and R.J. Arsenault, Metal Matrix Composites: Processing and Interfaces. Boston: Academic Press. (1991). 43.

[35] J.T. Blucher, U. Narusawa, M. Katsumata, and A. Nemeth, Composites Part A: Applied Science and Manufacturing 32 (2001) 1759-1766.

[36] M.D. Skibo and D.M. Schuster, Process for preparation of composite materials containing nonmetallic particles in a metallic matrix, and composite materials made thereby. U.S. Patent No. 4786467. (1988).

[37] P. Mathur, D. Apelian, and A. Lawley, Acta Metallurgica 37 (1989) 429-443.

[38] S. A.R.E, European Materials Research Society 1990 Spring Meeting on Metal Matrix Composites 135 (1991) 13-17.

[39] T.Z. Kattamis and T. Suganuma, Materials Science and Engineering: A 128 (1990) 241-252.

[40] J.S. Reed, Introduction to the Principles of Ceramic Processing Wiley and Sons, (1988).

[41] L.E. Murr, Metallurgical Applications of Shock-Wave and High-Strain-Rate Phenomena Marcel Dekker, Inc., New York, (1986).

[42] N. Popovska, H. Gerhard, D. Wurm, S. Poscher, G. Emig, and R.F. Singer, Materials & Design 18 (1997) 239-242.

[43] E. Cappelli, S. Orlando, F. Pinzari, A. Napoli, and S. Kaciulis, Applied Surface Science 138â€“139 (1999) 376-382.

[44] Q. Bao, C. Chen, D. Wang, Q. Ji, and T. Lei, Applied Surface Science 252 (2005) 1538-1544.

[45] E.C. Santos, M. Shiomi, K. Osakada, and T. Laoui, International Journal of Machine Tools and Manufacture 46 (2006) 1459-1468.

[46] J.C. Ion, Chapter 12 - Cladding, in Laser Processing of Engineering Materials. Butterworth-Heinemann: Oxford. (2005) 296-326.

[47] D. Novichenko, A. Marants, L. Thivillon, P.H. Bertrand, and I. Smurov, Lasers in Manufacturing - Proceedings of the Sixth International WLT Conference on Lasers in Manufacturing. (2011) 296-302.

[48] L. Dubourg and J. Archambeault, Surface and Coatings Technology 202 (2008) 5863-5869.

[49] L. Dubourg, D. Ursescu, F. Hlawka, and A. Cornet, Wear 258 (2005) 1745-1754.

[50] X. Wu, R. Sharman, J. Mei, and W. Voice, Materials & Design 25 (2004) 103-109.

[51] I. Yadroitsev and I. Smurov, Lasers in Manufacturing 2011 - Proceedings of the Sixth International WLT Conference on Lasers in Manufacturing. (2011) 264-270.

[52] I. Yadroitsev and I. Smurov, Laser Assisted Net Shape Engineering , Proceedings of the LANE (2010) 551-560.

[53] I. Yadroitsev, L. Thivillon, P. Bertrand, and I. Smurov, Laser synthesis and processing of advanced materials E-MRS-P Symposium 254 (2007) 980-983.

[54] L. Thijs, F. Verhaeghe, T. Craeghs, J.V. Humbeeck, and J.-P. Kruth, Acta Materialia (2011) 3303-3312.

[55] P.H. Chong, H.C. Man, and T.M. Yue, Surface and Coatings Technology 154 (2002) 268-275.

[56] L.E. Murr, S.A. Quinones, S.M. Gaytan, M.I. Lopez, A. Rodela, E.Y. Martinez, D.H. Hernandez, E. Martinez, F. Medina, and R.B. Wicker, Journal of the Mechanical Behavior of Biomedical Materials 2 (2009) 20-32.

[57] D.T. Pham and R.S. Gault, International Journal of Machine Tools and Manufacture 38 (1998) 1257-1287.

[58] J.D. Majumdar, B.R. Chandra, A.K. Nath, and I. Manna, Surface and Coatings Technology 201 (2006) 1236-1242.

[59] J.J. Candel, V. Amiga, J.A. Ramos, and D. Busquets, Surface and Coatings Technology (2004) 3161-3166.

[60] P.H. Chong, H.C. Man, and T.M. Yue, Surface and Coatings Technology 145 (2001) 51-59.

[61] J. Fernandez, A. Isalgue, N. Cinca, S. Dosta, and J. Ventayol, 3rd International Symposium on Shape Memory Materials for Smart Systems/E-MRS 2010 Spring Meeting. (2010) 77-80.

[62] I. Hussainova, Microstructure and erosive wear in ceramic-based composites. Wear (2005) 357.

[63] I. Hussainova, Effect of microstructure on the erosive wear of titanium carbide-based cements. Wear (2003) 121.

[64] X. Pei, J. Wang, Q. Wan, L. Kang, M. Xiao, and H. Bao, Surface and Coatings Technology (2005) 4380-4387.

[65] J. Dutta Majumdar, I. Manna, A. Kumar, P. Bhargava, and A.K. Nath, Journal of Materials Processing Technology 209 (2009) 2237-2243.

[66] J.D. Ayers, Wear 97 (1984) 249-266.

[67] J. Nurminen, J. Nakki, and P. Vuoristo, International Conference on the Science of Hard Materials (2009) 472-478.

[68] M.M. Savalani, C.C. Ng, Q.H. Li, and H.C. Man, Applied Surface Science. (2012) 3173-3177.

[69] M.M. Savalani, C.C. Ng, Q.H. Li, and H.C. Man, Applied Surface Science 258. (2005) 3173-3177.

[70] J. DuttaMajumdar and L. Li, Development of titanium boride (TiB) dispersed titanium matrix composite by direct laser cladding, Materials Letters. (2010) 1010-1012.

[71] N.V. Pimenova and T.L. Starr, Electrochimica Acta 51 (2006) 2042-2049.

[72] I. Aziz, Z. Qi, and X. Min, Chinese Journal of Aeronautics 22 (2009) 670-676.

[73] T.T. Wong and G.Y. Liang, Journal of Materials Processing Technology 63 (1997) 930-934.

[74] T.N. Baker, H. Xin, C. Hu, and S. Mridha, Materials Science Technology 10 (1994) 536-544.

[75] W. Cerri, R. Martinella, G.P. Mor, P. Bianchi, and D.D. Angelo, Surface and Coatings Technology 49 (1991) 40-45.

[76] P. Sallamand and J.M. Pelletier, Materials Science and Engineering: A 171 (1993) 263-270.

[77] K.G. Watkins, M.A. McMahon, and W.M. Steen, Materials Science and Engineering: A 231 (1997) 55-61.

[78] M. Bethencourt, F.J. Botana, J.J. Calvino, M. Marcos, and M.A. Rodriguez-Chacan, Corrosion Science 40 (1998) 1803-1819.

[79] W.C. Oliver and G.M. Pharr, J.Mater.Res. 7 (1992) 1564.